



Technische Universität München

Max-Planck-Institut für Plasmaphysik

Experimental characterization of the core plasma flow at the ASDEX Upgrade tokamak

Alexander Lebschy

Vollständiger Abdruck der von der Fakultät für Physik der Technischen Universität München zur Erlangung des akademischen Grades eines

Doktors der Naturwissenschaften

genehmigten Dissertation.

Vorsitzender: Prof. Dr. Frank Pollmann

Prüfer der Dissertation:

1. Prof. Dr. Ulrich Stroth

2. Prof. Dr. Stefan Schönert

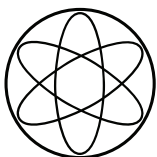
Die Dissertation wurde am 05.02.2018 bei der Technischen Universität München eingereicht und durch die Fakultät für Physik am 17.04.2018 angenommen.



DEPARTMENT OF PHYSICS
TECHNISCHE UNIVERSITÄT MÜNCHEN

Experimental characterization of the core plasma flow at the ASDEX Upgrade tokamak

Alexander Lebschy



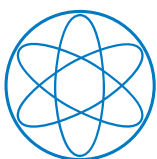


DEPARTMENT OF PHYSICS
TECHNISCHE UNIVERSITÄT MÜNCHEN

Experimental characterization of the core plasma flow at the ASDEX Upgrade tokamak

Author: Alexander Lebschy
Supervisor: Prof. Dr. Ulrich Stroth
Advisor: Dr. Rachael M. McDermott

Submission Date: 5th February 2018



Abstract

One of the most promising concepts to achieve fusion on earth are toroidal devices like tokamaks that confine plasmas with helically twisted magnetic field lines. In these devices, the rotation of the plasma has a strong influence on the plasma transport by the stabilization of modes and the suppression of plasma turbulence, which affects the transport of heat, particles, and momentum. In tokamaks, the toroidal rotation (u_{tor}) is essentially a free parameter that is usually dominated by the external momentum input from the neutral beam sources used to heat the plasma. The poloidal rotation (u_{pol}), on the other hand, is strongly damped due to the motion of the particles from the regions with higher magnetic field to lower magnetic field (and vice versa) and the associated transfer from poloidal to toroidal rotation (magnetic pumping effect). Despite many previous investigations, the nature of the core u_{pol} remains an open question: studies at the tokamak DIII-D show that at low collisionalities, u_{pol} is significantly more in the ion diamagnetic direction than predicted from neoclassical (NC) theory. At higher collisionalities, however, a good agreement between experiment and theory was found at the tokamaks TCV and DIII-D, which is qualitatively consistent with the edge results from both Alcator C-Mod and ASDEX Upgrade (AUG).

In order to study the core impurity u_{pol} at AUG the core charge exchange recombination spectroscopy (CXRS) systems have been upgraded with new toroidal optical heads providing 70 additional lines-of-sight (LOSs) from the low-field side (LFS) to the high-field side (HFS) pedestal top. From theory it is known that any plasma flow can be expressed through a component parallel to the magnetic field and a rigid body rotation such that the measurement of the core toroidal flow at two points of the same flux surface (LFS/HFS) enables an indirect determination of the core u_{pol} with an accuracy better than 1 km/s for certain plasma parameters and regimes.

At AUG, the core u_{pol} at mid-radius is found to be more ion diamagnetic directed than the neoclassical prediction for both L- and H-mode discharges. At the plasma edge, u_{pol} is found to be electron diamagnetic directed and in good agreement with NC codes, consistent with previous investigations at AUG. In order to characterize the core u_{pol} further at AUG, different parameter dependencies were investigated in the framework of the poloidal rotation database. In the H-mode data there is an increase in the difference between the experimentally measured and theoretically predicted u_{pol} values at lower collisionalities concomitant with larger normalized Larmor radii. A possible explanation for this result is a balance between the neoclassical damping and the turbulent drive of u_{pol} . Within this picture, the dominant driving mechanism for u_{pol} at the lowest collisionalities of the database is turbulence. At higher collisionalities, the turbulent drive is reduced and the experimental profiles agree with the neoclassical predictions within their uncertainties.

The indirect measurement of the core u_{pol} provides as well the missing ingredient to evaluate the core $\vec{u}_{\vec{E} \times \vec{B}}$ velocity from measurements only, which can then be compared to measurements of perpendicular plasma flow velocity (u_{\perp}) of the turbulent fluctuations to gain information on the turbulent phase velocity (v_{ph}). This approach has been utilized to gain further information on the physics behind the transition from the linear Ohmic confinement (LOC) to the saturated Ohmic confinement (SOC) regime in

Ohmically heated L-mode discharges. The non neoclassical u_{pol} values from CXRS lead to good agreement between $\vec{u}_{\vec{E} \times \vec{B}}$ and u_{\perp} indicating that v_{ph} is small and at similar values as found with gyrokinetic simulations. Moreover, the data shows a shift in the ion diamagnetic direction at the plasma edge after the transition from LOC to SOC, which is qualitatively consistent with a change in the dominant turbulence regime from trapped electron mode (TEM) to ion temperature gradient (ITG). The upgrade of the core CXRS system provides as well a deeper insight into the intrinsic rotation of Ohmic L-mode discharges. This thesis shows that the reversal of the core u_{tor} occurs clearly after the LOC-SOC transition and concomitant with the peaking of the electron density.

Zusammenfassung

Tokamaks sind eines der vielversprechendsten Konzepte, um Fusion auf der Erde zu erreichen und die immer steigende Energienachfrage zu decken. In diesen Gefäßen werden Plasmen aus Wasserstoff-Isotopen durch einen helikal verdrillten magnetischen Käfig eingeschlossen und auf Temperaturen von mehr als 150 Millionen Grad aufgeheizt. Die Rotation des Plasmas hat einen sehr starken Einfluss auf die Stabilität verschiedener Moden des Plasmas und die Ausprägung der Turbulenz, die den Transport von Wärme, Teilchen und Impuls maßgeblich bestimmt. Die toroidale Rotation ist in Tokamaks ein freier Parameter, der typischerweise durch den externen Impulsübertrag von neutralen Atomen, die zur Heizung des Plasmas verwendet werden, bestimmt wird. Im Gegensatz dazu, wird die poloidale Rotation durch die Bewegung der Teilchen von Regionen mit großer magnetischer Feldstärke in Bereiche mit geringem magnetischen Feld (und umgekehrt) stark gedämpft und die neoklassische Theorie sagt Werte kleiner als 2 km/s voraus. Obwohl die poloidale Rotation das Thema einer Vielzahl von wissenschaftlichen Arbeit ist, bleibt ihr Ursprung unbekannt: Untersuchungen an dem Tokamak DIII-D zeigen zum Beispiel, dass es einen signifikanten Unterschied zwischen der gemessenen und theoretischen vorhergesagten poloidalen Rotation bei kleinen Kollisionsalitäten gibt. Bei höheren Kollisionsalitäten wurde eine gute Übereinstimmung mit der neoklassischen Theorie an den Tokamaks DIII-D und TCV gefunden, die qualitativ mit Messungen an den Experimenten Alcator C-Mod und AUG am Plasmarand übereinstimmt.

Um die poloidale Rotation im Zentrum von AUG experimentell zu messen, wurden die Systeme der Ladungsaustauschspektroskopie (CXRS), um ein weiteres toroidales System mit insgesamt 70 Sichtlinien vom Plasmarand an der Niederfeld- zur Hochfeldseite, erweitert. Durch den bekannten Zusammenhang, dass jede Plasmaströmung durch eine Komponente parallel zum magnetischen Feld und einer Starrkörperrotation ausgedrückt werden kann, ermöglicht die simultane Messung der toroidalen Plasmaströmung an zwei Punkten der gleichen magnetischen Flussfläche die Bestimmung der beiden Komponenten und damit eine indirekte Messung der poloidalen Rotation. Eine Sensitivitätsstudie zeigt, dass die poloidale Rotation im Plasmazentrum mit dieser Methode mit Fehlern kleiner als 1 km/s gemessen werden kann.

Die poloidale Rotation bei AUG zeigt in der Mitte des Plasmaradius mehr in die diamagnetische Bewegungsrichtung der Ionen als von der neoklassischen Theorie vorhergesagt für L- und H-Mode Plasmen. Am Plasmarand zeigt die poloidale Rotation in die diamagnetische Driftrichtung der Elektronen und stimmt mit der neoklassischen Vorhersage gut überein. Die Beobachtungen am Plasmarand bestätigen vorherige Messungen bei AUG. Um Parameterabhängigkeiten der poloidalen Rotation zu analysieren wurde eine Datenbank für die poloidale Rotation. In den Daten der H-Mode Plasmen wurde ein Anstieg des Unterschiedes zwischen der Messung und der Theorie hinzu kleinen Kollisionsalitäten beobachtet. Diese kleinen Kollisionsalitäten stimmen mit den größten Werten des normierten Larmorradius überein, so dass die Beobachtungen ein Gleichgewicht zwischen der neoklassischen Dämpfung der poloidalen Rotation und dem turbulenten Antrieb nahelegen. Mit dieser Interpretation würde der Antrieb für die poloidale Rotation bei kleinen Kollisionsalitäten die Turbulenz sein. Bei größeren Kollisionsalitäten bestimmt die neoklassische Dämpfung die Rotation und eine gute Übereinstimmung wird beobachtet.

Die indirekte Messung der poloidalen Rotation ist außerdem die fehlende Komponenten, um die $\vec{E} \times \vec{B}$ Geschwindigkeit ($\vec{u}_{\vec{E} \times \vec{B}}$) im Plasmazentrum zu messen. Ein Vergleich mit der senkrechten Geschwindigkeit (u_{\perp}) von turbulenten Fluktuationen ermöglicht Informationen über die Phasengeschwindigkeit (v_{ph}) der Turbulenz zu erhalten. Dieser Ansatz wurde verwendet, um weitere Informationen über die Physik hinter dem Übergang von dem linearen Ohmschen Energieeinschluss (LOC) Bereich zum gesättigten Ohmschen Energieeinschluss (SOC) Bereich zu erhalten. Die nicht neoklassischen Rotationen in der Mitte des Plasmaradiuses führen zu einer guten Übereinstimmung von $\vec{u}_{\vec{E} \times \vec{B}}$ und u_{\perp} , die zeigt, dass v_{ph} klein ist und mit Vorhersagen von gyrokinetischen Codes übereinstimmt. Die Messungen zeigen außerdem, dass die Veränderung von v_{ph} in die diamagnetische Bewegungsrichtung der Ionen erst nach dem Übergang von LOC nach SOC passiert. Diese Veränderung stimmt qualitativ mit einem Übergang in der dominanten Turbulenz von der gefangenen Elektronenmode zu der Ionen Temperaturgradienten Mode überein. Die Erweiterung der CXRS Systeme im Plasmazentrum ermöglicht zudem einen tieferen Einblick in die intrinsische Rotation von Ohmschen L-Mode Plasmen. Diese Arbeit zeigt, dass die Umkehrung der toroidalen Rotation im Zentrum deutlich nach dem LOC-SOC Übergang passiert und von der Erreichung des Höhepunkts des Gradienten in der Elektronendichte begleitet wird.

Contents

Abstract	iii
Zusammenfassung	v
1 Introduction	1
1.1 Thermonuclear Fusion	1
1.2 Magnetic confinement: the tokamak concept	3
1.3 Scope of this thesis	6
2 The ASDEX Upgrade tokamak	9
2.1 Overview of ASDEX Upgrade	9
2.2 Heating sources	10
2.3 Plasma diagnostics at AUG	12
2.4 Deducing the magnetic equilibrium	17
3 Theoretical background on the plasma flow	21
3.1 Fluid motion	21
3.2 Radial plasma transport	25
3.3 Plasma rotation in toroidal geometry	31
3.4 Neoclassical poloidal rotation	34
3.5 Plasma confinement	36
4 Charge Exchange Recombination Spectroscopy at AUG	41
4.1 Measurement principle	41
4.2 Toroidal CXRS systems at AUG	44
4.3 Characterization and calibration of CXRS diagnostics	47
4.4 Corrections to CXRS measurements	52
4.5 Validation of CXRS measurements	56
4.6 Measurement of the core poloidal rotation	58
5 Validation of the indirect measurement technique	63
5.1 Artificial data	63
5.2 Effects of uncertainties in the magnetic equilibrium	66
5.3 Uncertainties in the q-profile	69
5.4 Phenomenology on impurity density asymmetries	71

5.5	Changing the drift directions	75
6	Characterisation of the core poloidal flow structure at ASDEX Up-grade	79
6.1	Flow predictions from neoclassical theory	79
6.2	Comparison to different neoclassical codes	83
6.3	Poloidal rotation database	84
6.4	Parameter dependencies	88
6.5	Implications for the main ion poloidal rotation	92
6.6	Conclusions	93
7	Measurement of the $E \times B$ velocity across the LOC-SOC transition	95
7.1	Overview of performed LOC-SOC experiments	95
7.2	Discharge design and measurement technique	98
7.3	Measurement of the poloidal rotation across the LOC-SOC transition . .	102
7.4	Measurement of the phase velocity across the LOC-SOC transition . . .	105
7.5	Reversal of the core toroidal rotation	107
7.6	Summary	109
8	Summary and outlook	111
	Acknowledgements	I
	Acknowledgments	I
	Acronyms	III
	Symbolslist	VII
	Glossary	IX
	Bibliography	XI
A	Taylor expansion of grating equation	XXIII
B	Derivations of q-dependence of indirect u_{pol} measurement	XXV

Chapter 1

Introduction

1.1 Thermonuclear Fusion

Our quality of life is based on the continuous availability and consumption of energy. The primary energy consumption increased by 120 % between 1973 and 2013 [1] and is expected to increase even further by 2030 [2] due to the increasing energy demand in the so-called developing countries. So far, the energy production is and was based mainly on the burning of fossil fuels such that the growth in energy demand is coupled to a massive rise in CO₂ emissions [2, 3]. The eventual shortage of these resources and the steadily increasing amount of greenhouse gases in the atmosphere [4] confront our society with new challenges in order to meet our energy demand. Therefore, new energy sources are necessary that are efficient, environmentally friendly, and economically viable.

A possible solution for the energy production problem is nuclear energy, since these processes do not generate CO₂ emissions and the typical energy release is six to seven orders of magnitude larger than in chemical reactions such as the burning of oil and coal. The basic principle of nuclear energy production is hidden in the dependency of the binding energy per nucleon ($\Delta E/A$) on the atomic mass number (A) shown in figure 1.1a. $\Delta E/A$ is the energy that would be required to disassemble the nucleus of an atom into neutrons and protons divided by A and in case that the resulting atom has a larger $\Delta E/A$ than the initial atom energy is released. Therefore, there are two energy production regions in figure 1.1a: fusion energy is produced by combining two light nuclei into a heavier one and fission energy production is feasible by splitting heavier nuclei into lighter ones. The border between these two regions is marked by ⁶²Ni.

Fission technology has been under development since 1954 [7] and produces currently 4.8 % of the primary energy world-wide [1]. Recent accidents (1986: Chernobyl, 2011: Fukushima) and the problem of storing the long-lived radioactive waste are, however, leading to a controversial discussion about the usage of fission and an eventual reduction in the usage of fission as an energy source. The advantage of fusion over fission is that no radioactive isotopes are produced in fusion reactions and that the fusion process can be stopped almost immediately since it is no chain reaction; making fusion an interesting candidate to help solving the energy production problem.

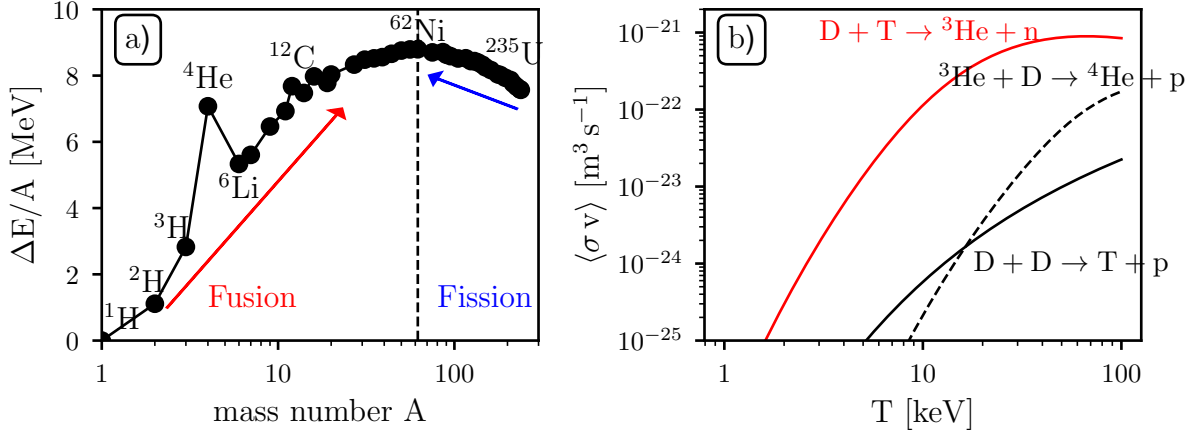
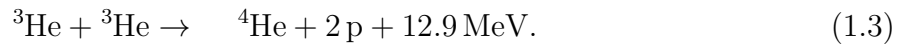
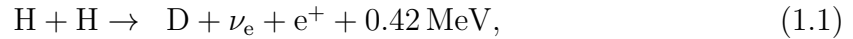


Figure 1.1: (a): The binding energy per nucleon $\Delta E/A$ as a function of the atomic mass number A has been calculated from the measured mass defect given in [5]. The element with the highest $\Delta E/A$ is ^{62}Ni . (b): Dependency of fusion rate coefficients on temperature (parameters taken from [6]).

The knowledge about fusion is actually older than the discovery of fission: The first evidence of a fusion reaction was found by Ernest Rutherford in 1919 [8] and Arthur Eddington proposed in 1920 fusion as the energy source of the stars [9]. The dominant energy production process in stars for temperatures¹ less than 1 keV is the proton-proton chain (see equations (1.1)–(1.3)): four protons fuse to make ^4He and release in total 26.7 MeV² of energy. This energy is released as gamma rays and kinetic energy of the fusion products.



The first step in the proton-proton chain, equation (1.1), involves the weak nuclear force and has, therefore, a very small rate coefficient ($\langle \sigma v \rangle \approx 10^{-45} \text{ m}^3 \text{s}^{-1}$) [10]. For a hydrogen (H) ion, it takes on average roughly 10^9 years for one of these reactions to occur. Therefore, different fusion reactions are considered for a future fusion power plant on earth involving deuterium (D), tritium (T) and helium (He):



¹Throughout this thesis energies and temperatures are expressed in eV: 1 eV is equal to 11.605 K.

²The energy difference between 26.7 MeV and the summed energy yield of the equations (1.1), (1.2), and (1.3) results from the annihilation of electrons and positrons: $e^- + e^+ \rightarrow 2\gamma + 1.02 \text{ MeV}$.

Figure 1.1b shows the rate coefficients for the different fusion reactions relevant for fusion on earth. The D-T reaction is the most promising one since it has the highest reaction rate and a broad maximum at around 50 keV. Deuterium accounts for roughly 0.0156 % of all naturally occurring hydrogen, and tritium can be bred with the neutrons from the fusion process by using lithium (Li): ${}^6\text{Li} + n \rightarrow {}^4\text{He} + \text{T} + 4.8 \text{ MeV}$. The naturally occurring deposits of these fuels are sufficient to meet the world energy demand for more than 1,000,000 years [11].

At the temperatures relevant for fusion, i.e. larger than 10 keV (more than 100 million degree Kelvin), the matter is in a state called plasma; the electrons are separated from the nuclei and both species can move independently from each other. The charge densities from ions and electrons are, however, equal such that the plasma is quasi neutral.

In present day experiments the total fusion power produced is less than the total energy losses of the plasma. The point at which the losses from the plasma can be covered by the heating from the α -particles resulting from the fusion process, is called ignition. By solving a global energy balance of the plasma, it can be expressed in terms of plasma parameters (Lawson criterion), i.e. by the fusion triple product of plasma density (n), plasma temperature (T) and energy confinement time (τ_E) [12]:

$$n T \tau_E \Big|_{\text{DT,ignition}} \geq \frac{12}{E_{\text{fus}}} \frac{T^2}{\langle \sigma_{\text{fus}} v \rangle} \approx 3 \cdot 10^{21} \text{ keV s/m}^3, \quad (1.7)$$

where $\langle \sigma_{\text{fus}} v \rangle$ is the fusion rate coefficient shown in figure 1.1b, τ_E is defined as the ratio between the energy stored inside the plasma and the net input power, and $E_{\text{fus,DT}} = 3.5 \text{ MeV}$ is the kinetic energy of the fusion produced helium nuclei (α -particles).

The Lawson criterion states that fusion triple product has to be larger than a certain value in order to achieve ignition. The fusion process has an optimum temperature for a maximum in the fusion power such that there are two separate approaches to meet this condition and realize fusion: magnetic confinement (trying to achieve a high energy confinement time) and inertial confinement (trying to achieve high plasma densities). The following discussion and this thesis in general will focus on magnetic confinement and further information on inertial confinement can be found, for example, in [13].

1.2 Magnetic confinement: the tokamak concept

There are no materials which can withstand the high temperatures needed for fusion without melting. Magnetic confinement overcomes this by keeping the charged particles away from the walls by the Lorentz force. In the early days, one tried to confine plasmas in a linear magnetic mirror configuration. It turned out that the losses at the end points are too high and the triple product is roughly a factor of 300 too small [14]. An alternative idea was to bend the magnetic field lines together into a torus. This is done by arranging toroidal field coils in a circle (see figure 1.2b) resulting in a purely toroidal magnetic field. The coils on the inner side of the circle are closer together than on the outer side resulting in a radial gradient of the magnetic field. The resulting movement of the particles around the magnetic field lines is, therefore, not helical but

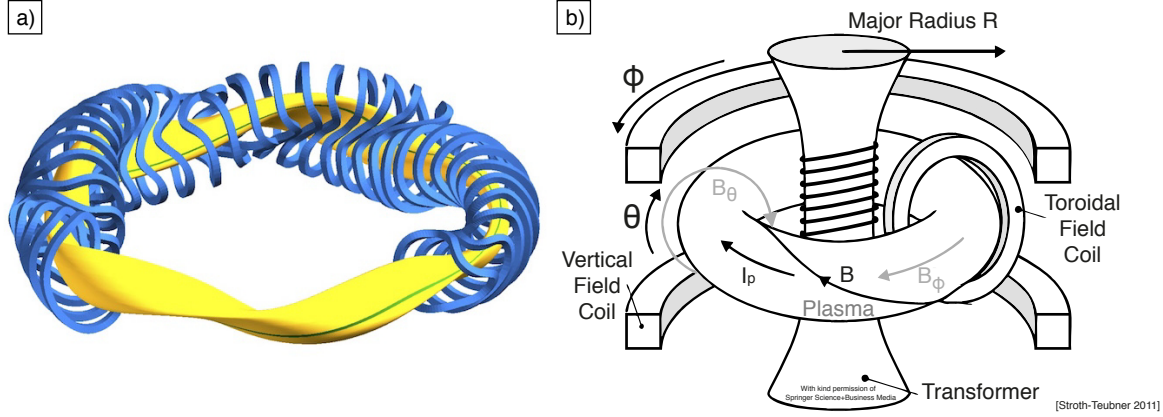


Figure 1.2: Comparison of two fusion concepts: (a) a schematic drawing of the stellarator Wendelstein 7-X (taken from [15]) and (b) the tokamak concept (taken from [16]).

has an additional up/down drift motion directed in opposite directions for electrons and ions. This charge separation leads to an electrical field and finally to a force that pushes the plasma radially outward to the wall. Therefore, the plasma is unstable in a purely toroidal magnetic field and an additional magnetic field perpendicular to the toroidal direction, called *poloidal* direction, is needed to average out the charge separation. The combination of the toroidal magnetic field (B_ϕ or B_{tor}) and poloidal magnetic field (B_θ or B_{pol}) leads to helical magnetic field lines as illustrated in figures 1.2b.

There are two concepts in order to realize the helical magnetic field: the tokamak (see figure 1.2b) and the stellarator (see figure 1.2a). The stellarator concept was proposed in 1951 by Lyman Spitzer Jr. [17] and generates the helical magnetic field directly through the design of the coils (see figure 1.2a showing a sketch of the magnetic coils from Wendelstein 7-X). The other concept, the tokamak (see figure 1.2b), was invented in the 1950s by the two Soviet physicists Igor Tamm and Andrei Sakharov [18] who were inspired by the original idea of Oleg Lavrent'ev [19]. The tokamak creates the poloidal magnetic field through the induction of a current in the plasma.

Comparing the two designs, it can be seen that the stellarator is more difficult to realize since the shape and position of the coils has to be computed numerically and the complexity and required accuracy pose extreme engineering challenges. The stellarator is, therefore, still one order of magnitude behind the tokamak in terms of performance (see figure 1.3). It features, however, the advantage that it can be operated continuously since there is no transformer necessary. As this work was done at a tokamak the following discussion will focus on this magnetic configuration.

The efficiency of a fusion device can be expressed as the ratio of the power produced by fusion reactions and the externally applied heating power defined as the fusion power gain Q . Breakeven is achieved when the fusion power is equal to the auxiliary power, i.e. $Q = 1$. The highest fusion gain obtained so far was achieved in a D-T plasma in the JET tokamak, located in Culham, England, with $Q = 0.62$ [21]. Figure 1.3 shows the fusion triple product of different experiments as a function of the achieved temperature. It can be seen that there is no experiment so far that exceeds the necessary value from

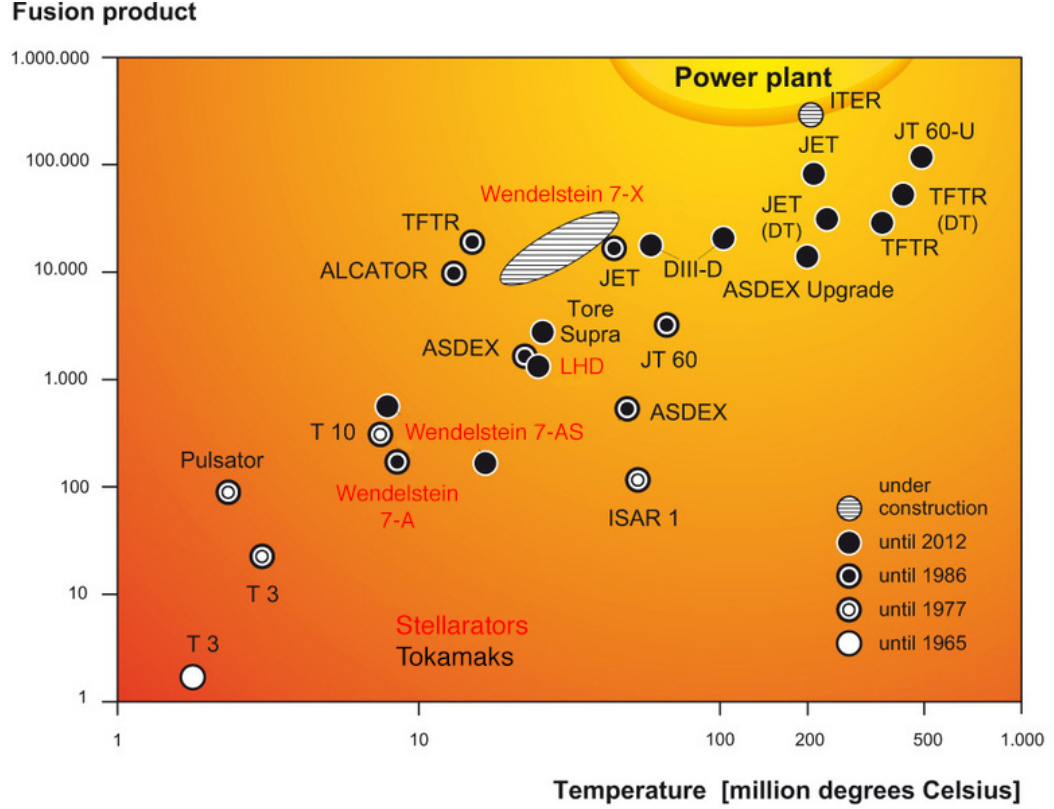


Figure 1.3: The fusion triple product achieved by various fusion experiments is shown against the plasma temperature. Above a certain threshold (Lawson criterion, see equation 1.7) the generated fusion energy overcomes the losses and the fusion experiment could be operated as a power plant (adapted from [20]).

equation (1.7). The next generation fusion device ITER is foreseen to operate above the critical value with $Q \geq 10$ [22].

The profiles of plasma parameters can be described in different coordinate systems. Due to the shape of a tokamak, the most simple one is a toroidal coordinate system (R, ϕ, z) , with the major radius R , the toroidal angle ϕ (as defined in figure 1.4), and the vertical position z . This can be converted into a Cartesian-cylindrical system (ρ, θ, ϕ) with the normalized radius ρ and the poloidal angle θ (see figure 1.4). One example for a definition of ρ is $\rho = r/a$ with r being the distance from the plasma center and a the minor radius of the plasma. The most commonly used definition of ρ is given by the equations from magneto-hydrodynamics (MHD). In the ideal MHD equilibrium, the single fluid force balance reduces to

$$\vec{j} \times \vec{B} = \vec{\nabla} p, \quad (1.8)$$

where \vec{j} is the plasma current density, \vec{B} the total magnetic field and $\vec{\nabla} p$ the pressure gradient. This equation defines flux surfaces on which the pressure is constant (see figure 1.4) and, thus, ρ can be defined using the poloidal magnetic flux Ψ at a cer-

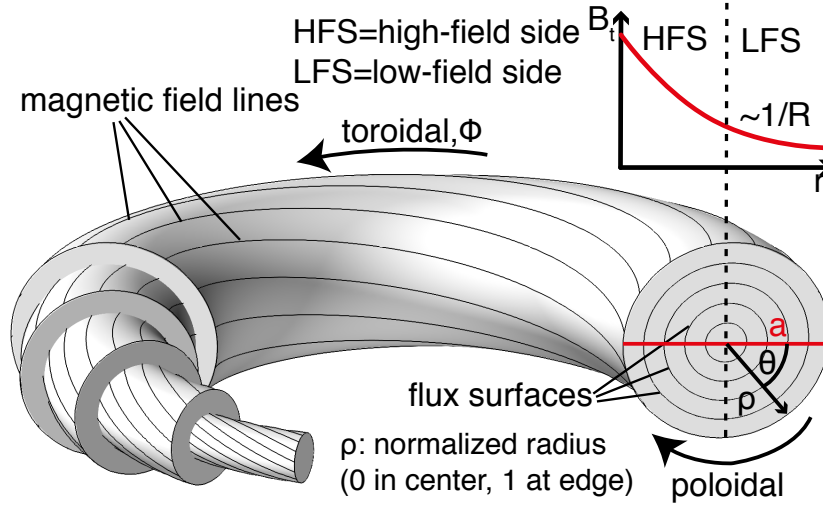


Figure 1.4: Magnetic geometry and coordinate system definitions in a tokamak configuration.

tain position and the magnetic flux at the separatrix³ ($\Psi_{\text{separatrix}}$) and at the magnetic axis (Ψ_{axis}):

$$\rho_{\text{pol}} = \sqrt{\frac{\Psi - \Psi_{\text{axis}}}{\Psi_{\text{separatrix}} - \Psi_{\text{axis}}}}; \quad \Psi = \int_{S_{\text{pol}}} B \cdot dS \quad (1.9)$$

A similar coordinate ρ_{tor} can be calculated by using the toroidal instead of the poloidal flux. This definition is more common for the plasma core, while ρ_{pol} is more typical for the edge. Throughout this thesis, ρ_{pol} and ρ_{tor} are used when showing plasma profiles. Additionally, movements of the plasma can be described relatively to the magnetic field, i.e. parallel and perpendicular to it.

From figure 1.4 it can be seen that B_{tor} has a $1/R$ dependence which results from the magnetic coil geometry. This dependency leads to two different areas on each flux surface: the high-field side (HFS) on the inboard side with larger magnetic fields and the low-field side (LFS) on the outboard-side with smaller magnetic fields.

1.3 Scope of this thesis

The plasma particles in a magnetic field are confined perpendicular to the field and free to flow parallel to the magnetic field. As a result, finite velocities develop and the plasma spins. In tokamaks, the toroidal rotation (u_{tor}) is essentially a free parameter that is usually dominated by the external momentum input from the neutral beam injection (NBI) heating. Figure 1.5 shows exemplarily that an increase in the NBI heating leads to an increase of u_{tor} in the plasma core. The poloidal rotation (u_{pol}), on the other hand, is strongly damped due to the motion of the particles from the LFS to the HFS and the associated magnetic pumping effect [23, 24] (see as well section 3.4.2). Therefore, the

³The last closed flux surface in a divertor configuration is called separatrix.

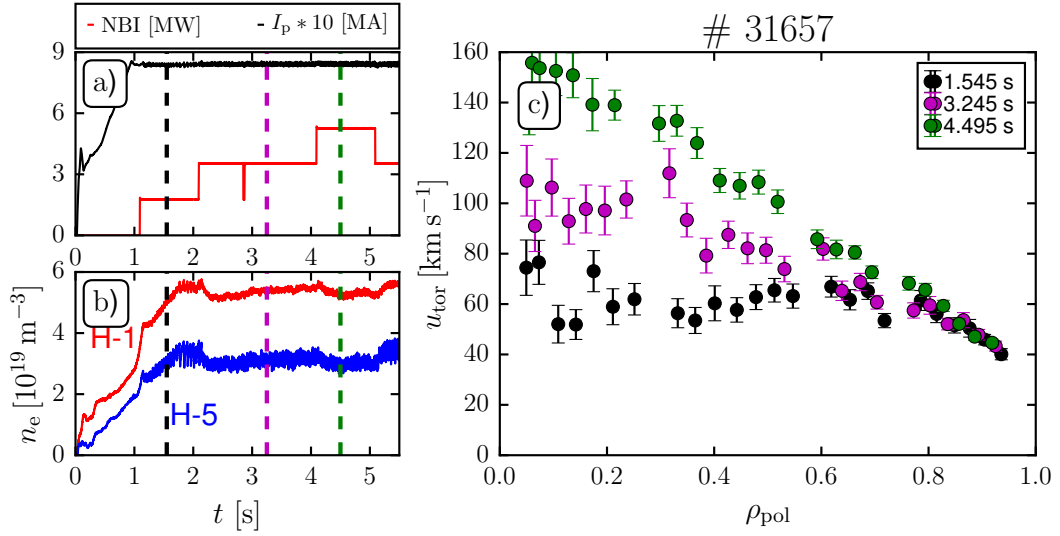


Figure 1.5: Time traces of a plasma discharge showing the impact of NBI heating on u_{tor} : (a) NBI heating power (red) and plasma current (I_p) (black), (b) central (H-1, red) and edge (H-5, blue) electron density (c) toroidal plasma rotation for three time points with different amounts of NBI heating.

predictions for u_{pol} in the plasma core (see sections 3.2 and 3.4) are on the order of a few km/s.

Nevertheless, u_{pol} is important for many aspects of magnetically confined plasmas as it affects the stability of different kinds of MHD modes [25] and induces transitions in the MHD equilibrium [26]. More generally, u_{pol} is connected to the radial electric field (E_r) which is a critical parameter for understanding the physics of micro-instabilities and turbulent transport in plasmas [27]. The determination of E_r through measurements of u_{tor} on the LFS and HFS of the plasma is a key point of this thesis. Since the divergence of the plasma flow has to vanish on each flux surface, the poloidal and toroidal flows are closely connected. Therefore, it is possible to extract E_r from measurements on the inboard and outboard sides.

In present day fusion devices, the rotation of the plasma is determined through spectroscopic diagnostics measuring the Doppler shift of known atomic emission lines. Charge exchange recombination spectroscopy (CXRS) exploits the line radiation from a charge exchange reaction between fully or partially stripped impurity ions and injected neutrals (more information will be given in chapter 4). With this technique, velocities as low as 5 km/s can be measured quite accurately. This is generally sufficient for core toroidal rotation measurements where velocities of 50 to 200 km/s are regularly observed. For measuring core poloidal velocities, however, which are expected to be only a few km/s, this accuracy is insufficient. Additionally, the atomic physics gets more complicated when measuring in the gyro-orbit plane (poloidal direction) such that corrections to u_{pol} are necessary that can be of the same order as the measurement [28], making the direct measurement of u_{pol} in the plasma core challenging.

These facts could be the reason that the reported direct measurements of u_{pol} show a rather complicated picture for the plasma core. In general a good agreement to theoretical predictions is found at smaller devices with lower magnetic fields and temperature and under “normal” plasma operations as, for example, at MAST [29], NSTX [30] and TEXT [31, 32]. In special plasma scenarios, a significant difference between the measured u_{pol} values and theory was found as reported in an internal transport barrier (ITB) at JET [33, 34], in QH-modes and H-mode plasmas at DIII-D [35]. At TFTR, a plasma with a reversal of the poloidal flow was found [36]. Recent studies at DIII-D show that u_{pol} is significantly higher at low collisionalities in the plasma core than expected from theory [37], which could have a significant impact on the plasma confinement if present in ITER, since will operate at even lower collisionalities.

In the 1980s, a novel technique was proposed at the PDX tokamak for the measurement of u_{pol} in the plasma core [38] and has recently been established as well at DIII-D [39], TCV [40], and as subject of this thesis on ASDEX Upgrade (AUG). The evaluation of the inboard-outboard asymmetry of u_{tor} is a possibility to measure the full plasma flow and, thus, to deduce u_{pol} indirectly in the plasma core accurately with errors in the order of ± 1 km/s [40, 41]. The advantage of this technique is that the indirect measurement is not affected by aforementioned atomic physics effects such that the uncertainty in the measurement is smaller and enables the accurate reconstruction of small poloidal rotation velocities. The results from TCV show a very good agreement between the theoretical predictions and the experimental values [40].

For this thesis, a new core CXRS system has been installed at AUG [42] (see chapter 4). This system has in total 70 dedicated lines-of-sight (LOSs) for the measurement of the plasma rotation from the separatrix on the LFS to the separatrix on the HFS and, thus, enabling the measurement of u_{pol} in the plasma core (see section 4.6.2). One particular topic of interest of this thesis is the change of u_{tor} in Ohmically heated plasma discharge featuring a transition in the confinement regime from linear Ohmic confinement (LOC) to saturated Ohmic confinement (SOC). By increasing the plasma density, τ_E increases first linearly (LOC) with the plasma density and saturates (SOC) eventually above a certain critical density. Additionally, this thesis aims at characterizing the nature of the core poloidal flow at AUG for the operating space available.

This thesis is structured as follows: Chapter 2 introduces the ASDEX Upgrade tokamak and important diagnostics which are used throughout this thesis. Chapter 3 gives an introduction into the theory behind the plasma flow, the general particle motion, and the equation for the indirect measurement of the poloidal rotation. Subsequently, the measurement technique of the plasma rotation, i.e. CXRS is introduced in chapter 4. Chapter 5 presents some initial tests on the indirect measurement technique and validates the measurement technique. In order to characterize the nature of the core poloidal flow, a database approach is presented in chapter 6 and the measured u_{pol} values are compared to theoretical predictions in a variety of discharges. Chapter 7 presents a novel technique to address the physics behind a change in the energy confinement time of the two Ohmic regimes observed in tokamaks and the last chapter concludes with a summary of the most important findings and an outlook for future work in chapter 8.

Chapter 2

The ASDEX Upgrade tokamak

This chapter gives an overview of the fusion experiment ASDEX Upgrade at which the experiments of this thesis have been carried out. It starts with a short general description of the machine and details of the heating systems, which is followed by an introduction to the relevant diagnostics for this thesis.

2.1 Overview of ASDEX Upgrade

The largest tokamak in Germany, ASDEX Upgrade, is situated in Garching bei München and is operated by the Max-Planck-Institut für Plasmaphysik. It is designed to study the physics needed for the next generation of fusion experiments. Due to similarities in magnetic configuration, divertor geometry, and plasma facing components, it is particularly well suited for studying the physics needed to successfully operate ITER, which is a joint effort of 35 countries world-wide and currently built in Cadarache (France). Its major radius is roughly 4 times the size of AUG. With a maximum electron density of $4.5 \cdot 10^{20} \text{ m}^{-3}$, a maximum core temperature of 10 keV, and a typical confinement time of 100 ms, AUG is one order of magnitude below the Lawson criterion for ignition: $nT\tau_E|_{\text{AUG}} \sim 4.5 \cdot 10^{20} \text{ m}^{-3} \text{ s keV} = 0.15 nT\tau_E|_{\text{ignition}}$. Thus, a burning plasma cannot be achieved in AUG discharges and it is typically operated with pure deuterium plasmas in order to minimize the neutron flux to the walls. Further parameters of the device are summarized in table 2.1.

Figure 2.1 shows a schematic illustration of the AUG tokamak. The toroidal magnetic field is created by 16 toroidal field (TF) coils and the poloidal magnetic field is generated by the plasma current which is mainly driven by a central transformer coil. The shaping coils and fast control coils are used for the vertical stabilization of the plasma and to add some more flexibility in the shaping of the magnetic flux surfaces.

AUG went into operation in 1992 and is the successor of the Axially Symmetric Divertor Experiment (ASDEX). The name of the device refers to the divertor concept which is a special magnetic field topology (see figure 2.2a) that allows efficient power and particle exhaust. The key of this concept is that the outermost magnetic field lines end on special tiles that tolerate large heat loads and have a high sputtering threshold. Particles expelled from the plasma do not impact the neighboring walls, but are guided

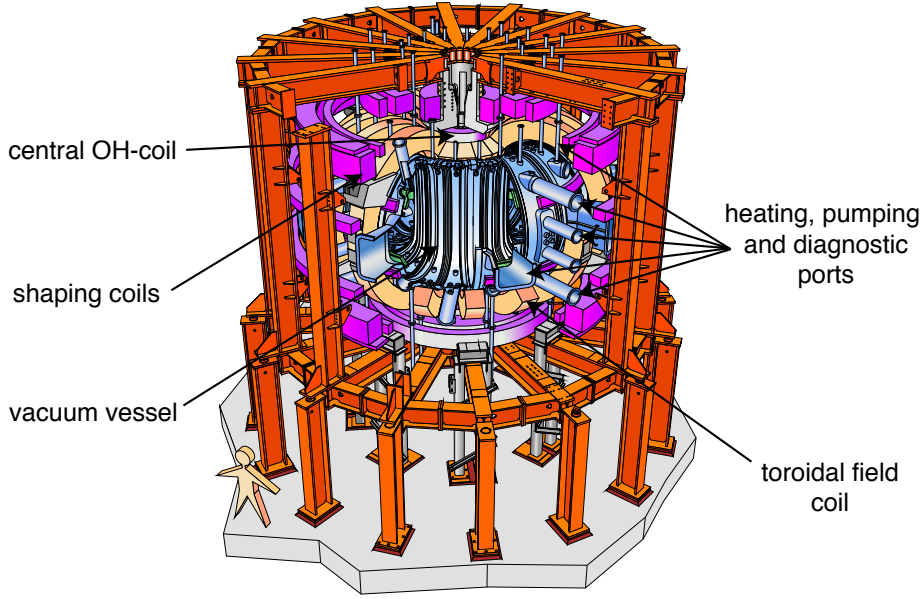


Figure 2.1: An overview of the ASDEX Upgrade tokamak. The vacuum vessel is shown in blue, the 16 toroidal field coils are shown in light orange and the coils determining the plasma shape and generating the plasma current are shown in purple. This figure is taken from [43].

to the divertor tiles where their energy is reduced by collisions with a cushion with a high neutral gas density. This concept leads, therefore, to a lower influx of sputtered wall materials into the plasma and, hence, to plasmas with higher main ion concentrations. The divertor concept was successfully tested at ASDEX and is as well foreseen for ITER.

2.2 Heating sources

In order to reach the temperatures relevant for fusion, i.e. 15 keV, it is necessary to externally heat the plasma until the α -heating can set in. An inherent heating mechanism in tokamaks is Ohmic heating. The toroidal current, which is necessary for the poloidal magnetic field (B_{pol}), heats the plasma through the resistance of the plasma. At low

major plasma radius R_0	1.65 m
minor plasma radius a	0.5 m
toroidal magnetic field $ B_\phi $	1 to 3 T
plasma current $ I_p $	0.4 to 1.2 MA
heating power	up to 33 MW
plasma volume	14 m ³
plasma mass	3 mg
plasma fuel	D, H, He

Table 2.1: Main machine parameters of ASDEX Upgrade

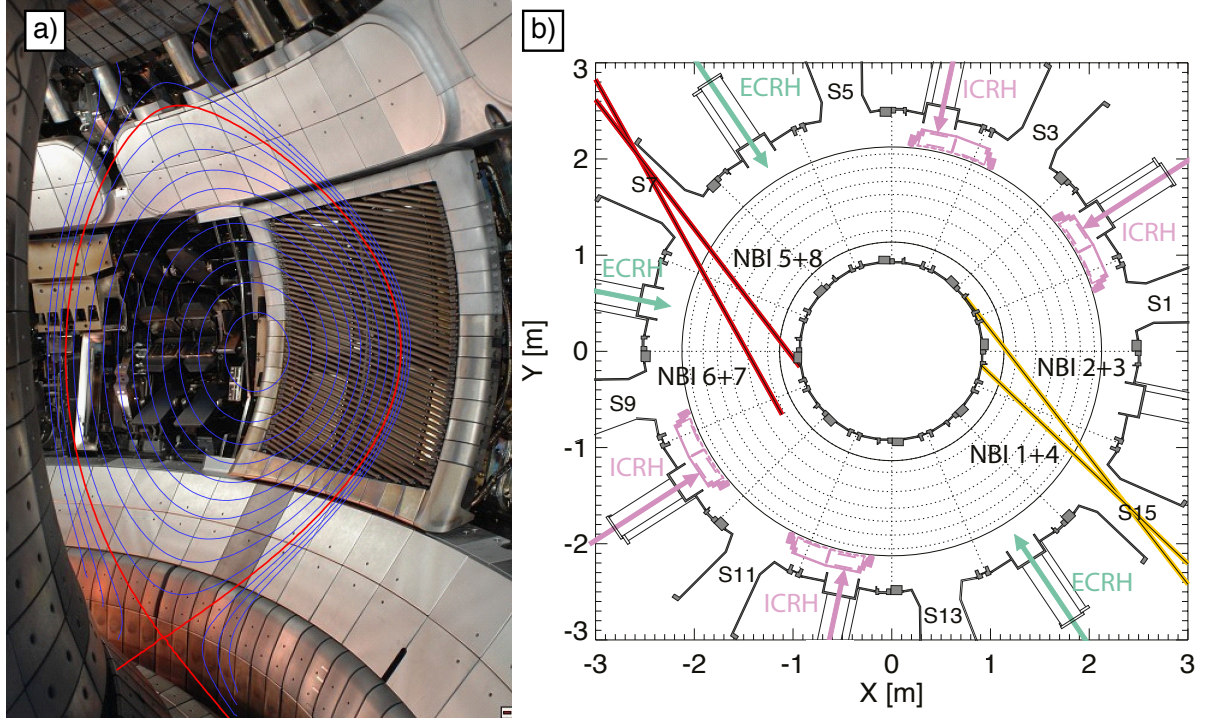


Figure 2.2: (a) View into the AUG vacuum vessel showing the magnetic flux surfaces. (b) Overview of the different heating sources installed at ASDEX Upgrade. These figures are taken from [43].

temperatures, this heating is very efficient, but the resistance of the plasma varies with the temperature as $T^{-3/2}$ [44] such that additional heating sources are necessary. The most common ones in present day fusion experiments are neutral beam injection and wave heating which will be described briefly in the next sections.

2.2.1 Neutral beam injection heating

The neutral beam injection (NBI) heating method injects fast neutral particles into the plasma which get trapped in the magnetic field after their ionization and transfer their energy to the plasma by collisions. These particles are generated in the following way: ions are extracted from an ion source and accelerated through an electric field to the desired energy. These ions are, subsequently, neutralized by passing through a cell with higher gas pressure and the remaining ions are filtered out by a perpendicular magnetic field before entering the plasma. At AUG, a deuterium ion source is typically used which produces in addition to D^+ , the molecules D_2^+ and D_3^+ . These molecules are accelerated by the electric field such that fast deuterium atoms are injected into the plasma that have full, half, and one third of the acceleration energy. The fraction of the different injection energies is called *species mix* and can be defined in terms of particle numbers (current) or with respect to the power.

As depicted in figure 2.2b, the AUG NBI system consists of two injectors/boxes located in sectors 15 (box 1) and 7 (box 2) with 4 sources each. Each source typically

injects deuterium atoms with a total power of 2.5 MW. Figure 2.2b shows that the sources located in sector 7 are named 5–8 and have a full injection energy of 93 keV. The sources in sector 15 are numbered 1–4 and have a maximum injection energy of 60 keV. The power species mix of the NBI sources 1–4 is typically 0.65 : 0.25 : 0.10 and for the sources 5–8, 0.62 : 0.29 : 0.09 [45]. Knowing this ratio is important for the accurate determination of the impurity density profile from CXRS measurements (see section 5.4). The NBI source 8 is of particular interest to this thesis since new CXRS spectrometers have been built utilizing this beam source to the complete core plasma flow at AUG.

2.2.2 Electron and ion cyclotron resonance heating

If electrons or ions have a velocity perpendicular to \vec{B} then they move in helical trajectories along \vec{B} . The frequency of the circular motion is given by $\omega_c = |q| B/m$ (cyclotron frequency). Effective wave heating, i.e. absorption of an injected frequency, is possible if the electromagnetic wave is injected with the frequency ω_c or some harmonics of it. This process is called electron cyclotron resonance heating (ECRH) if it heats the electrons and ion cyclotron resonance heating (ICRH) for the ions. Due to the $1/R$ dependence of the toroidal magnetic field, ω_c depends as well on R and, hence, this method provides a localized heating of the electrons or ions.

The locations of the ECRH and ICRH antennas in AUG are illustrated in figure 2.2b. The ECRH system at AUG can be operated at either 105 or 140 GHz, which corresponds to the second harmonic cyclotron frequency of electrons at magnetic fields of 1.8 and 2.5 T, respectively. This heating mechanism provides at AUG a power of up to 4 MW [45] and is beneficial to prevent the accumulation of heavy impurities (such as tungsten) in the plasma core, which leads to a loss of confinement due to the strong radiation losses and could eventually cause to a disruption of the plasma.

At AUG, the ICRH waves are typically injected with a frequency of 30 or 36 MHz and heat the hydrogen minority present in deuterium plasmas [44]. At AUG, this system consists of four generators with a frequency range of 30 to 120 MHz and an output power of 2 MW each. The radio frequency waves are coupled to the plasma via four antennas which are located behind shielding strips (see figure 2.1a) in the wall of the tokamak.

2.3 Plasma diagnostics at AUG

In order to get accurate predictions from theory, it is necessary to measure the ion temperature and electron density and their gradients accurately. At AUG, there are various diagnostics measuring these kinetic profiles. The most relevant ones for this thesis are introduced in this section.

2.3.1 Electron cyclotron emission

The reconstruction of the T_e profile is based on a radiometer measuring the electron cyclotron emission (ECE) at the cyclotron frequency ω_c during the gyro-motion of

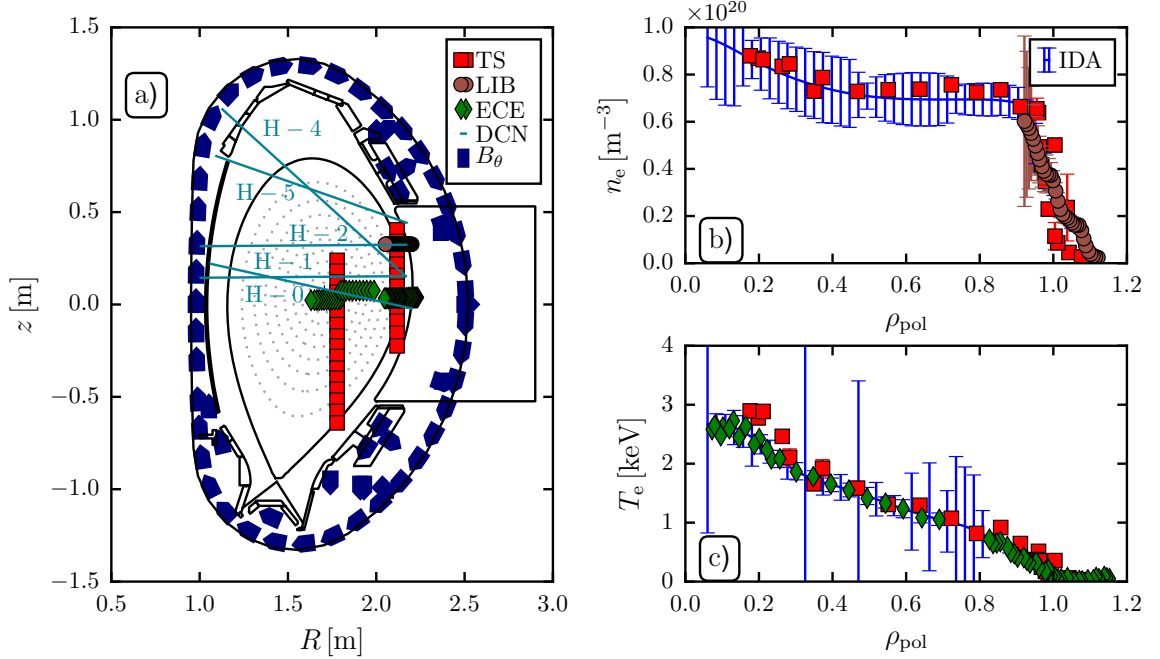


Figure 2.3: Overview of the measurement positions of the individual diagnostics in the poloidal plane (a) and a comparison of the electron density (n_e) (b) and electron temperature (T_e) (c) profiles from the integrated data analysis (IDA) and the measurements from individual diagnostics. The DCN interferometry measurements are not shown in (b) since they are line-integrated.

electrons around the magnetic field lines. In the ideal case, the plasma emits radiation as a black body so that the intensity of the emitted electromagnetic radiation is proportional to the plasma temperature. At low temperatures (Rayleigh Jeans approximation: $\hbar\omega \ll k_B T$), the intensity I of the radiation is given by Planck's radiation formula:

$$I(\omega) = \frac{\omega_c^2 k_B T}{8 \pi^3 c^2}, \quad (2.1)$$

where k_B is the Boltzmann constant and c the speed of light. The information on the plasma position is given by the $1/R$ dependence of \vec{B} . The T_e profile can, therefore, be derived from:

$$T(R) = \frac{8 \pi^3 c^2 I(\omega_c(R))}{k_B \omega_c^2(R)}. \quad (2.2)$$

At AUG, the intensity is measured with a multichannel heterodyne radiometer in the frequency range from 89 to 187 GHz. It measures the second harmonic cyclotron radiation at 60 different frequencies (positions) as shown in figure 2.3a [46]. More information on the ECE diagnostic is given in [47, 48].

2.3.2 Lithium beam emission spectroscopy

The Li-beam (LIB) emission spectroscopy observes the spectral radiance of the Li I(2s – 2p) transition resulting from injected Li atoms with an energy of 30 to 80 keV. The neutral Li atoms collide with the plasma particles leading to excitation and de-excitation of the atoms as well as ionization through collisions and charge exchange processes. These processes depend on n_e and, therefore, n_e can be reconstructed using a system of coupled linear equations [49]:

$$\frac{d N_i}{dl} = \sum_j [n_e(l) a_{ij}(T_e(z)) + b_{ij}] N_j(z), \quad (2.3)$$

$$N_i(l = 0) = \delta_{1i}, \quad (2.4)$$

where l is the coordinate along the lithium beam ($l = 0$ is the entrance of the beam to the plasma), N_i is the occupation density of the i -th energy level, a_{ij} is the rate coefficient for the transition $i \rightarrow j$ and b_{ij} is the Einstein coefficient for the spontaneous de-excitation. At AUG, the temporal resolution of the diagnostic is 200 kHz [50]; a more detailed description can be found in [51, 52].

2.3.3 Laser interferometry

If an electromagnetic wave with the wavelength λ_0 passes through the plasma, it experiences a phase shift by an angle ϕ depending on the local electron density profile $n_e(l)$:

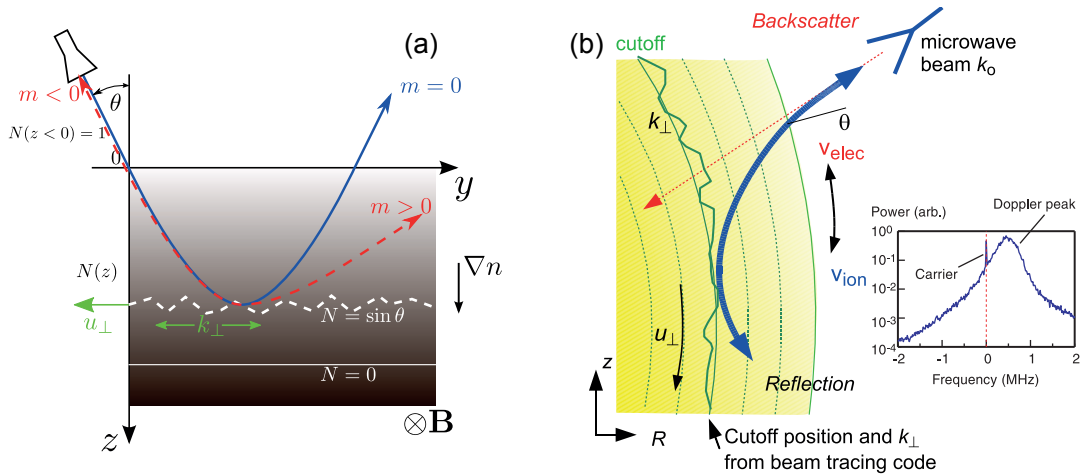
$$\phi = \frac{\lambda_0 e^2}{4 \pi \epsilon_0 m_e c^2} \int n_e dl, \quad (2.5)$$

where l is the coordinate along the wave path, ϵ_0 the vacuum permittivity and e the elementary charge. Laser interferometry provides, therefore, a line-integrated measurement of n_e and, given a sufficient large number of lines-of-sight, it is possible to deduce the full n_e profile. However, access restrictions often give a limit of 5–10 LOSs.

The deuterium cyanide laser (DCN) system used at AUG is equipped consists of a laser at a wavelength of 195 μm ; figure 2.3a shows the LOS geometry in a poloidal view. At the inner wall, the injected electromagnetic waves are reflected with a mirror and the phase shift is measured with a Mach-Zehnder interferometer. A phase shift of 2π corresponds to a line-integrated density of 5.3×10^{18} electrons/ m^2 [53].

2.3.4 Thomson scattering

Thomson scattering (TS) is a common diagnostic technique that provides localized, simultaneous measurements of n_e and T_e . This diagnostic is based on the measurement of incoherent scattering of laser light on the plasma electrons [54–56]. The electromagnetic wave accelerates charged particles, which then emit radiation in all directions and, thereby, scatter the incoming wave. In the case of a plasma, it is sufficient to consider the scattering off electrons only ($m_e \ll m_i$). The Doppler width of the scattered wave provides information on T_e and the intensity on n_e .



AUG is equipped with two vertical TS systems, one for the plasma core and one for the edge; see figure 2.3a [57]. The systems consist of six (core) and four (edge) lasers and the scattered waves are collected with, in total, 26 polychromators. The scattering volumes are around 25 mm³ in the core and 3 mm³ at the plasma edge. The TS system provides n_e and T_e profiles with a temporal resolution of 8 and 3 ms, respectively.

2.3.5 Integrated data analysis of electron density and temperature profiles

At AUG, the measurements of several diagnostics measuring n_e and T_e are combined in the integrated data analysis (IDA) framework, which treats the error bars of the individual diagnostics using Bayesian probability theory. Thereby, systematic errors of the different diagnostics can be detected faster and the combined fit to all experimental measurements results in self-consistent profiles. In its standard setup, IDA uses ECE for the evaluation of the T_e profile and a combined analysis of LIB emission spectroscopy, DCN interferometry, and TS for the determination of n_e . Figure 2.3a shows the measurement positions of the different diagnostics in the poloidal plane and figures 2.3b and c compare the measurements from the individual diagnostics to the result from the IDA analysis.

2.3.6 Reflectometry

For this thesis, two reflectometry systems are of special interest: the Doppler reflectometry (DR) system and the poloidal correlation reflectometry (PCR). They both provide measurements of the perpendicular plasma flow velocity.

Doppler reflectometry

Figure 2.4a illustrates the principle of Doppler reflectometry: A microwave beam is launched into the plasma under a finite tilt angle θ with respect to the normal of the flux surface and is eventually reflected at a cutoff surface (order $m = 0$, see figure 2.4a) depending on the magnetic field and the density of the plasma. In the presence of density fluctuations, the cutoff surface is corrugated, and the injected wave gets scattered at the cutoff layer (orders $m \neq 0$). The scattering surface can be described as a reflection grating with a small sinusoidal corrugation characterized by a wavenumber k_\perp [60]. If the order -1 is observed then the emitting antenna can be operated as receiving antenna and the backscattered wave satisfies the Bragg condition

$$k_\perp = 2k_0 \sin \theta, \quad (2.6)$$

where k_0 is the wave vector of the microwave. With curved cutoff-layers (i.e. in real geometry, figure 2.4b), a ray or beam tracing code has to be used to calculate the radial position of the back-scattering volume and the probed turbulence wavenumber. At AUG, the ray tracing code TORBEAM is typically used [61].

In case the fluctuations move relative to the diagnostics antenna, the backscattered signal is Doppler shifted with a frequency:

$$\omega_D = \vec{u} \cdot \vec{k} = u_\perp k_\perp + u_\parallel k_\parallel + u_r k_r, \quad (2.7)$$

where \vec{u} is the mean velocity of the density fluctuations. The Doppler shift can be seen in the typical DR spectrum shown in figure 2.4b. The intensity is proportional to the amplitude of the turbulence fluctuations at the probed wavenumber.

The DR systems are optimized such that they are only sensitive to k_\perp and not to k_\parallel by aligning them perpendicular to the magnetic field. Additionally, it has been shown that k_\perp/k_\parallel is close to 200 in the stellarator experiment TJ-K [62], about 100 to 200 in TEXT [63, 64] and roughly 30 in TFTR [65] for magnetically confined plasmas. The radial component of equation (2.7) can be neglected, since u_r is very small and the DR system is optimized to select the $k_r \approx 0$ component. This means, that both the radial and the parallel component of the Doppler shift can be neglected in general: $\omega_D \approx u_\perp k_\perp$ [59, 66]. The measured perpendicular velocity corresponds to the sum of the $\vec{E} \times \vec{B}$ drift velocity $\vec{u}_{\vec{E} \times \vec{B}}$ and the turbulent phase velocity v_{ph} :

$$u_\perp = \vec{u}_{\vec{E} \times \vec{B}} + v_{ph}. \quad (2.8)$$

A commonly used approximation is $\vec{u}_{\vec{E} \times \vec{B}} \gg v_{ph}$, so that the previous equation reduces to $u_\perp = \vec{u}_{\vec{E} \times \vec{B}}$ and the radial electric field can be calculated from u_\perp : $E_r = u_\perp B$. It is, however, very difficult to confirm this approximation experimentally. At TJ-II, this approximation was validated in ECRH and NBI heated L-mode plasmas through comparative studies between DR and a heavy ion beam probe [67]. Comparisons with Langmuir probes at AUG [68] and with spectroscopic measurements at Wendelstein 7-AS [60] support this approximation as well. Recent comparisons of u_\perp measured at different k_\perp values done with DR at AUG suggest a turbulent phase velocity in the order of

1.6 km/s [58] while simulations yielded phase velocities smaller than 0.5 km/s. Together with very accurate measurements of $\vec{u}_{\vec{E} \times \vec{B}}$ from CXRS this approximation can be tested and the magnitude of v_{ph} can be estimated. Chapter 7 presents some results obtained for this thesis showing that v_{ph} is smaller than 1 km/s and at a similar magnitude as predicted from theory [69].

Poloidal Correlation Reflectometry

The poloidal correlation reflectometry diagnostic uses a multi-point time-delay estimation approach to get information on the perpendicular velocity and the pitch angle of the magnetic field lines [70]. The PCR diagnostic launches microwaves into the plasma where they propagate until they reach a cutoff layer. The reflected wave is received by a cluster of antennas (instead of one antenna), which is distributed toroidally and poloidally with respect to the launching antenna. By cross-correlating the reflectometer signals from different antennas, properties of the density fluctuations can be obtained such as the correlation length, decorrelation time, and the fluctuation propagation velocity [71] as well as the pitch angle of the magnetic field lines [72].

2.4 Deducing the magnetic equilibrium

In order to relate the locally measured profiles to the magnetic coordinate system (introduced in section 1.2) an accurate reconstruction of the magnetic equilibrium at all positions in the plasma vessel is necessary. This section introduces briefly the techniques applied for the magnetic equilibrium reconstruction.

2.4.1 Grad-Shafranov equation

Figure 2.2a shows the magnetic topology of an AUG plasma in the poloidal plane. It can be described by a set of nested flux surfaces of constant magnetic flux. The toroidal component of the magnetic field is well known due to accurate measurements of the currents in the TF coils. The poloidal component, however, is created by the plasma current and has to be reconstructed from the current distribution in the plasma. Starting from the equilibrium equation (1.8), the equilibrium for an axisymmetric system, such as a tokamak, can be calculated from a differential equation for the poloidal flux ψ (Grad-Shafranov equation) [73, 74]:

$$-\Delta^* \psi = \mu_0 R^2 \frac{dp}{d\psi} + f \frac{df}{d\psi} = \mu_0 R j_\phi, \quad (2.9)$$

where $-\Delta^*$ is the Grad-Shafranov operator, p the flux function describing the plasma pressure, f the flux function describing the poloidal current and j_ϕ the toroidal current density. This equation has two arbitrary functions (f , p) and the task of equilibrium codes is to solve equation (2.9) for these variables.

At AUG, there are several approaches to solve equation (2.9). CLISTE [75, 76] is an iterative solver that uses information from 63 different magnetic pick-up coils (see

blue arrows in figure 2.3a) measuring the local poloidal magnetic field at their relative positions. Additionally, the information on the currents in different coils (toroidal field coils, Ohmic transformer, shaping coils, passive stabilizing loop) are used routinely to get the magnetic equilibrium. The results from CLISTE can be constrained further by taking into account the thermal pressure profile and that of fast ions [77].

A novel technique couples the solver of the Grad-Shafranov equation to the results of the current diffusion equation. The resulting equilibrium can be constrained further by including information from diagnostics like the motional Stark effect (MSE) diagnostic and polarimetry, which are sensitive to the current distribution in the plasma (a short description is given in section 2.4.2). This method allows the evaluation of different measurements in the framework of Bayesian probability theory and is called integrated data analysis equilibrium (IDE) [78]. Equilibrium results from CLISTE with a 100 ms time resolution (EQI) and 1 ms time resolution (EQH) and the IDE reconstruction are used in this work. General mapping is done with EQH, as IDE is only provided upon request for special analysis.

2.4.2 Additional constraints on the plasma current profile

There are some diagnostics installed at AUG that are sensitive to the current distribution in the plasma. These will be outlined briefly since they are used inside the equilibrium reconstruction with IDE code.

Motional Stark Effect diagnostic

An important effect on the spectrum of the injected neutrals from the NBI sources is the motional Stark effect. It is similar to the normal Stark effect splitting and shifting the spectral lines of molecules and atoms in the presence of a magnetic field. The slight difference is, however, that the electric field is not stationary present in the tokamak, but caused by the movement of the beam neutrals in the magnetic field. In the rest frame of the beam neutrals the electric field is given by: $\vec{E} = \vec{u}_n \times \vec{B} + \vec{E}_0$, where \vec{u}_n corresponds to the velocity of the beam neutrals and \vec{E}_0 to the background electric field.

This effect splits, therefore, the emission lines into parallel (π) and perpendicularly (σ) polarized light with respect to the electric field. The basic idea behind the MSE diagnostic is to measure the polarization of the σ - and/or π -polarized light and, thereby, to get information on the local magnetic field. The local magnetic field provides then an additional constraint on the local current distribution since the toroidal field component is well known. Further information on this measurement technique can be found, for example, in [79–81].

At AUG, there are two implementations of the MSE diagnostic: the conventional MSE [82, 83] provides up to 60 LOSs from the plasme edge to the core and the imaging motional Stark effect (iMSE) [84] measures the MSE effect in a continuous volume on a charge coupled device (CCD)-chip.

Polarimetry diagnostic

The DCN system introduced in section 2.3.3 can be used as well to get more insight on the plasma current distribution since light traveling through the plasma along a magnetic field is affected by the so-called Faraday rotation [81]. The linearly polarized electromagnetic wave from the laser can be considered as a superposition of two circularly polarized lights. The left- and right- circularly polarized lights experience different refractive indices such that the linear polarization changes its direction depending on the parallel magnetic field along the observation direction and electron density. By knowing the local electron density, information on the local magnetic field can be obtained [82, 85]. This diagnostic technique is known as polarimetry (POL).

Chapter 3

Theoretical background on the plasma flow

The previous chapter explained that a magnetic field is necessary to keep the hot plasma away from the wall of the fusion device. This chapter will give a brief overview of the theory of flows in a plasma. It starts with a general introduction to the fluid motion of the plasma, which is followed by an overview of the radial plasma transport. Subsequently, the theory behind the new approach to measure u_{pol} in the plasma core is presented in section 3.3 and, in general, the expectations for u_{pol} from theory are as well presented in this chapter. It concludes with an overview over different confinement regimes observed in tokamaks.

3.1 Fluid motion

Charged particles experience good confinement perpendicular to the magnetic field, i.e. they gyrate around the magnetic field line with the cyclotron frequency $\omega_{c,\alpha}$ and the Larmor radius $r_{L,\alpha}$:

$$\omega_{c,\alpha} = \frac{|q_\alpha|B}{m_\alpha}; \quad r_{L,\alpha} = \frac{v_{\perp,\alpha}}{\omega_{c,\alpha}} = \frac{m_\alpha v_{\perp,\alpha}}{|q_\alpha|B}, \quad (3.1)$$

where q_α is the charge, m_α the mass of a particle α , and B the absolute value of the magnetic field. Parallel to the magnetic field line, there is no confinement and the movement is unchanged. The gyro-motion of the particle is typically not of interest, but rather the movement of the guiding center in the magnetic field. The guiding center approximation is valid for magnetic fields that feature large spatial gradient lengths $\nabla B/B$ and slow temporal changes in magnitude $\frac{\partial B}{\partial t}/B$ with respect to the Larmor radius and the cyclotron frequency, respectively [44].

In order to describe the movement of the plasma two pictures can be applied: the particle picture and the fluid picture, which give similar solutions for the plasma movement. For the fluid picture, the equations derived from hydrodynamics are extended with the Maxwell equations which is then called magneto-hydrodynamics. The following

introduction to the plasma dynamics focuses mostly on the fluid picture, where the single trajectories of the particles are not of interest. Additional information on the treatment of the plasma in terms of the particles can be found, for example, in [16, 44, 86].

3.1.1 Boltzmann equation

The kinetic theory of gases and plasmas describes their behavior in terms of statistical parameters of the particles involved. In this description, the particles are characterized by their positions \vec{r} and velocities \vec{v} in the six-dimensional phase space. The distribution function $f_\alpha(\vec{x}, \vec{v}, t)$ measures the probability density for a species α in a phase space volume. The kinetic and collisional evolution of a plasma is described by the Boltzmann equation:

$$\frac{\partial f_\alpha}{\partial t} + \vec{v}_\alpha \cdot \nabla f_\alpha + \frac{q_\alpha}{m_\alpha} \left(\vec{E} + \vec{v}_\alpha \times \vec{B} \right) \cdot \nabla_v f_\alpha = \left(\frac{\partial f_\alpha}{\partial t} \right)_{\text{collisions}}. \quad (3.2)$$

Multiplying this equation with the mass of the particle m_α and taking the first and second order velocity moments yield the mass and momentum conservation equations for the species α [87]:

$$\frac{d\rho_{m\alpha}}{dt} + \rho_{m\alpha} \nabla \cdot \vec{u}_\alpha = 0 \quad (3.3)$$

$$\underbrace{\rho_{m\alpha} \frac{d\vec{u}_\alpha}{dt}}_{\text{inertia}} = \underbrace{\rho_\alpha \left(\vec{E} + \vec{u}_\alpha \times \vec{B} \right)}_{\text{Lorentz force}} - \underbrace{\nabla p_\alpha}_{\text{pressure force}} - \underbrace{\nabla_\beta \Pi_{\alpha\beta}}_{\text{viscosity}} + \underbrace{\vec{R}}_{\text{friction}}. \quad (3.4)$$

The total time derivative of these equations is defined as $\frac{d}{dt} = \frac{\partial}{\partial t} + \vec{u}_\alpha \cdot \nabla$. The mean velocity of the particles, also known as the fluid velocity, is defined as $\vec{u}_\alpha = \langle \vec{v}_\alpha \rangle = \frac{1}{n_\alpha} \int v f_\alpha d^3v$. The density is given by $n_\alpha = \int f_\alpha d^3v$, $\rho_{m\alpha} = mn$ is the mass density and $\rho_\alpha = q_\alpha n_\alpha$ is the charge density. The quantity p_α is the scalar pressure and $\Pi_{\alpha\beta} = \rho_{m\alpha} \langle \vec{v}_\alpha^* \vec{v}_\beta^* - \vec{v}_\alpha^{*2} / 3 \delta_{\alpha\beta} \rangle$ is known as the viscous stress tensor [87]. The friction term \vec{R} occurs in case that electrons and ions flow with different velocities and can be written as $\vec{R} = nm_e \nu_{ei} (\vec{u}_e - \vec{u}_i)$, where ν_{ei} is the electron-ion collision frequency [16]. Equation (3.3) is as well known as the continuity equation and equation (3.4) as the equation of motion of the plasma.

3.1.2 Force balance equation

Considering a stationary plasma (i.e. $\frac{d}{dt} = 0$), neglecting friction forces between different species, and assuming an isotropic pressure, i.e. $\Pi_{\alpha\beta} = 0$, the equation of motion of the plasma reduces to:

$$\nabla p_\alpha = \rho_\alpha \left(\vec{E} + \vec{u}_\alpha \times \vec{B} \right). \quad (3.5)$$

This equation is known as the force balance equation and states that to lowest order the Lorentz force is balanced by the pressure force. The electric field parallel to the magnetic field lines is, however, very small since accumulations of charges can be balanced out easily. The radial component of the electric field is of special interest since it is

governed by the perpendicular transport of electrons and ions. The radial component of equation (3.5) can be written as:

$$E_r = \frac{\nabla_r p_\alpha}{\rho_\alpha} + u_{\perp, \alpha} B, \quad (3.6)$$

$$= \frac{\nabla_r p_\alpha}{\rho_\alpha} - u_{\text{pol}, \alpha} B_{\text{tor}} + u_{\text{tor}, \alpha} B_{\text{pol}}. \quad (3.7)$$

Equation (3.7) is written in the coordinate system of the torus and can be used to determine the radial electric field experimentally. Therefore, the flow and the kinetic profiles of an impurity species α has to be measured experimentally (see chapter 4).

3.1.3 Drifts perpendicular to the magnetic field

In order to derive flows perpendicular to the magnetic field, the cross-product of the equation (3.5) and the magnetic field is taken. Additionally, an external force \vec{f}_{ext} is assumed acting on the plasma¹:

$$0 = \rho_\alpha \left(\vec{E} + \vec{u}_\alpha \times \vec{B} \right) - \nabla p + \vec{f}_{\text{ext}} \mid \times \vec{B}, \quad (3.8)$$

$$\Rightarrow \quad \vec{u}_\perp = \underbrace{\frac{\vec{E} \times \vec{B}}{B^2}}_{\vec{u}_{\vec{E} \times \vec{B}}} - \underbrace{\frac{\nabla p \times \vec{B}}{\rho_\alpha B^2}}_{\vec{u}_{\text{dia}, \alpha}} + \underbrace{\frac{\vec{f}_{\text{ext}} \times \vec{B}}{\rho_\alpha B^2}}_{\vec{u}_{\text{ext}}}. \quad (3.9)$$

Equation (3.9) shows that an electrical field, a pressure gradient and in general a force perpendicular to the magnetic field lead to a flow of the plasma perpendicular to the magnetic field. These components will be discussed briefly in the following.

$\vec{E} \times \vec{B}$ drift

The $\vec{E} \times \vec{B}$ drift results from the presence of an electric field and the corresponding force $\vec{F} = q_\alpha \vec{E}$. According to equation (3.9), the drift can be expressed as:

$$u_{\vec{E} \times \vec{B}} = \frac{\vec{E} \times \vec{B}}{B^2}. \quad (3.10)$$

It is important to note that this drift is independent of the charge or mass of the particles such that the electrons and ions drift in the same direction and with the same velocity leading to macroscopic fluid flow without the generation of any electric current.

¹In the derivation the following vector identity is used:

$$\left(\vec{u} \times \vec{B} \right) \times \vec{B} = -B^2 \underbrace{\vec{u}}_{=\vec{u}_\parallel + \vec{u}_\perp} + \underbrace{\left(\vec{B} \cdot \vec{u} \right) \cdot \vec{B}}_{=\vec{u}_\parallel B^2} = -\vec{u}_\perp B^2$$

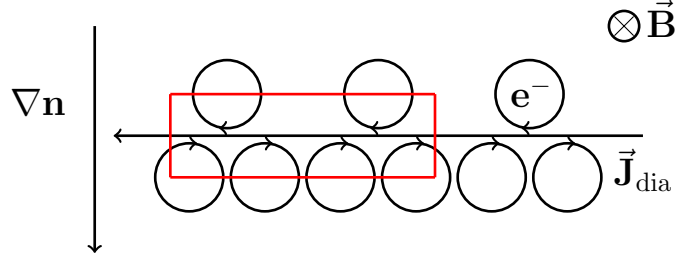


Figure 3.1: Physical origin of the magnetization current. At the horizontal line, there are more orbits from the high density side pointing to the right than orbits from the low density side pointing to the left. The differential causes a magnetization current \vec{J}_{dia} horizontally to the left side. This figure has been adapted from [86].

Diamagnetic drift

The diamagnetic drift is not directly connected to the guiding center drifts. It arises from a gradient in the pressure that is perpendicular to the magnetic field and causes a fluid drift. Figure 3.1 illustrates the origin of the drift: Due to the gradient in the density in a given volume (red box) there are more particles gyrating to the right at the horizontal line resulting in a net drift. The electrons and ions drift in opposite directions such that a current is generated, the so-called diamagnetic current \vec{J}_{dia} . The general form of this drift is given by:

$$\vec{u}_{\text{dia},\alpha} = -\frac{\nabla p_\alpha \times \vec{B}}{\rho_\alpha B^2}. \quad (3.11)$$

The diamagnetic drift depends on the charge of the particles and is, therefore, oppositely directed for electrons and ions.

General drift caused by an external force

In equation (3.9) it was shown that any perpendicular external force will lead to a perpendicular drift of the form:

$$\vec{u}_{\text{ext}} = \frac{\vec{f}_{\text{ext}} \times \vec{B}}{\rho_\alpha B^2} \quad (3.12)$$

The origin of this drift can be explained best when looking at the trajectory of a single particle (see figure 3.2). In case there is no external force (case a), the particle gyrates around the magnetic field line with a certain radial distance, i.e. the Larmor radius. With an external force, the particle gets accelerated through \vec{f}_{ext} as it moves from position 4 to 2 and slowed down between 2 and 4. This implies, effectively, that the average velocity is higher in the upper part of the plot, i.e. between 1 and 3, than in the lower part. A higher perpendicular velocity is associated with a larger Larmor radius (see equation 3.1) such that the gyro-motion has a larger radius in the upper part of the plot as well. This results in an effective drift of the guiding center perpendicular to \vec{f}_{ext} and \vec{B} as it is shown in figure 3.2b.

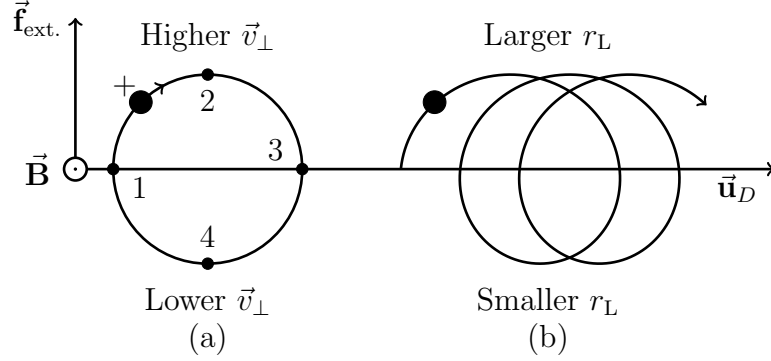


Figure 3.2: Schematic illustration of the effect of a force $\vec{f}_{\text{ext.}}$ perpendicular to \vec{B} on the particle drift: \vec{v}_{\perp} is higher in the upper part of the plot leading to a larger r_L . The varying radius of the gyro-motion leads, subsequently, to an effective drift in the $\vec{f}_{\text{ext.}} \times \vec{B}$ -direction (y -axis of the plot).

∇B drift

Another drift which applies to single particles and will be important for the following section is the drift due to the magnetic field gradient (see section 1.2), i.e. it has a $1/R$ -dependence such that there is a gradient in \vec{B} along R . The gradient in the magnetic field causes a force $f_{\nabla B} = -0.5 m u_{\perp, \alpha}^2 \frac{\nabla B}{B}$ [16] and thus a drift of the form:

$$\vec{u}_{\nabla B, \alpha} = -\frac{m_{\alpha} u_{\perp, \alpha}^2}{2q_{\alpha}} \frac{\nabla B \times \vec{B}}{B^3}. \quad (3.13)$$

The ∇B drift is in opposite directions for electrons and ions.

There are additional drifts, like the polarization drift, the curvature drift, or the gravitational drift. These drifts are, however, not relevant for this thesis and will not be considered here. A treatment can be found for example in [44, 86].

3.2 Radial plasma transport

3.2.1 Classical transport by collisions

Charged particles gyrating around magnetic field lines can collide with particles from other field lines leading to radial transport caused by Coulomb collisions (classical transport). In the particle picture, the classical transport can be described by a random-walk diffusion model with the diffusion coefficient given by

$$D_{\text{classical}} = \frac{(\Delta x)^2}{2 \Delta t}, \quad (3.14)$$

where Δx is the typical step size and Δt the characteristic time scale of the random-walk model. Particles are transported from the magnetic field lines by drifts (see section 3.1.3)

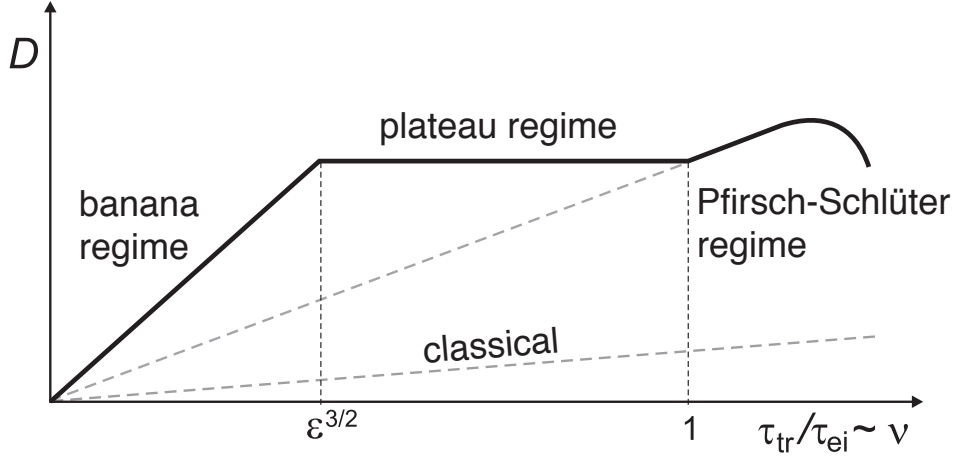


Figure 3.3: Comparison of the classical and neoclassical diffusion coefficients for the different plasma regimes. This figure is taken from [16].

and through collisions. Classical transport does, however, only treat collisions. The collisions happen mostly under small angles and it takes typically one momentum relaxation time τ until the direction of the movement is shifted by 90° [16]. The collision between the same particle species will not lead to an effective particle transport. The typical time scale and step size of the system are, therefore, given by the inverse of the electron-ion collision frequency and the electron Larmor radius:

$$D_{\text{classical}} = \frac{r_{Le}^2}{2\tau_{ei}} \approx \left(\frac{mu}{qB} \right)^2 \frac{1}{2\tau_{ei}} \quad (3.15)$$

Comparisons with experimentally measured diffusion coefficients show, however, that the transport measured in experiments is substantially larger.

3.2.2 Neoclassical transport

The drifts introduced in section 3.1.3 and the inhomogeneous magnetic field of a tokamak leads to additional transport that is covered by the neoclassical (NC) transport theory [88]. Neoclassical transport is divided by the ratio of the transit time τ_{tr} and the electron-ion collision time τ_{ei} into the banana regime, the plateau regime, and the Pfirsch-Schlüter regime (see figure 3.3). The transit time τ_{tr} is given by the time a particle needs to cover a complete poloidal turn:

$$\tau_{tr} = \frac{2\pi R}{u_{||}} q_s, \quad (3.16)$$

where $q_s = (rB_\phi)/(RB_\theta)$ is the safety factor.

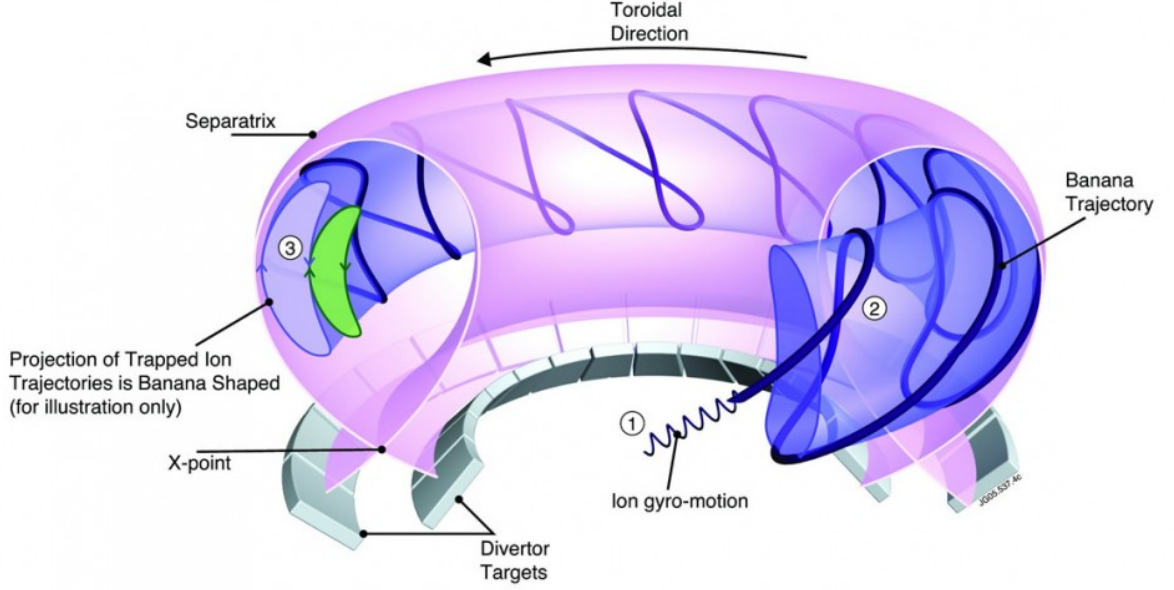


Figure 3.4: Illustration of the banana orbit. This figure is taken from [89].

Pfirsch-Schlüter transport

In the Pfirsch-Schlüter regime the collision time is smaller than the transit time, i.e. $\tau_{tr}/\tau_{ei} > 1$. The drifts in the magnetic field (outlined in section 3.1.3) lead to a displacement of the guiding center of the particle from the magnetic field line by the value $\delta_{PS} = (m u q_s)/(q B)$ such that the diffusion coefficient in the Pfirsch-Schlüter regime is given by [16]:

$$D_{PS} = \frac{\delta_{PS}^2}{2\tau_{ei}} = \frac{1}{2\tau_{ei}} \left(\frac{m u q_s}{q B} \right)^2 = D_{classical} q_s^2. \quad (3.17)$$

This simple derivation shows that the transport in the Pfirsch-Schlüter regime is enhanced by q_s^2 . A more thorough derivation shows that the diffusion coefficient is actually enhanced by $2q_s^2$ so that the total diffusion coefficient is given by: $D_{neo} = D_{classical}(1+2q_s^2)$ [16]. For typical values of $q_s = 3$, the classical transport is enhanced by a factor of 20.

Banana transport

The banana regime treats transport for collision times larger than the transit time. The main difference to classical transport is that particles can get trapped in the magnetic field. The magnetic moment of the charged particle $\mu = \frac{1}{2} m u_{\perp}^2 / B$ is conserved in a slowly varying magnetic field. Since the magnetic field changes from the HFS to the LFS, u_{\perp} has to change as well. Additionally, the kinetic energy of the particle is conserved meaning that the parallel velocity has to increase as u_{\perp} decreases and vice versa. Therefore, there is an interchange between the parallel and perpendicular energy

and the particle can be trapped between LFS and HFS if the mirror condition is fulfilled:

$$\left| \frac{u_{\parallel}}{u_{\perp}} \right| < \sqrt{2\epsilon}, \quad (3.18)$$

where $\epsilon = r/R$ is the aspect ratio (in the limit $\epsilon \ll 1$). Assuming a Maxwellian distribution of the particle velocities, the fraction of trapped particles is given by $n_t/n = \sqrt{2\epsilon}$. Due to the $\nabla B \times B$ drift and its different directions on LFS and HFS, the poloidal projection of the trapped particle's trajectory has a banana shape (see figure 3.4) with a width:

$$w_B = \frac{r_L}{\sqrt{\epsilon}} q_s, \quad (3.19)$$

which is wider than the step size of the classical transport by $q_s/\sqrt{\epsilon}$. Additionally, the collision frequency of the neoclassical transport is enhanced by $1/\epsilon$ implying that the diffusion coefficient for the banana regime is given by:

$$D_{\text{Ba}} = \underbrace{\sqrt{\epsilon}}_{\text{frac. trapped}} \left(\frac{r_L q_s}{\sqrt{\epsilon}} \right)^2 \frac{1}{2 \tau_{ei} \epsilon} = \frac{q_s^2}{\epsilon^{3/2}} D_{\text{classical}} = \frac{1}{\epsilon^{3/2}} D_{\text{PS}}. \quad (3.20)$$

The neoclassical transport is, therefore, roughly a factor 50 higher than the classical transport. The boundary at which the banana transport sets in is given by the condition that the effective collision time is larger than the reflection time of the banana τ_{Ba} :

$$\tau_{ei} \epsilon = \tau_{\text{eff}} \leq \tau_{\text{Ba}} = \frac{\tau_{\text{tr}}}{\sqrt{\epsilon}} \Rightarrow \frac{\tau_{\text{tr}}}{\tau_{ei}} \leq \epsilon^{3/2}. \quad (3.21)$$

In the plateau regime, the diffusion coefficient is constant and, therefore, equal to the values at the boundary to the banana and Pfirsch-Schlüter regimes. In order to predict transport properties from theory it is necessary to assume some orderings. Typical assumptions are shown in [88].

3.2.3 Turbulent transport

Even though neoclassical transport predictions are significantly larger than classical estimates, the observed transport is in general larger than the neoclassical predictions [90, 91]. Observed transport beyond neoclassical theory is attributed to turbulent transport. From a theoretical point of view, turbulent transport is due to a release of free energy driving fluctuations in the plasma parameters. These fluctuations, which can be thought of as small irregular structures, enhance the radial transport due to microscopic potential structures. There is evidence [66, 92] that microinstabilities are one generation mechanism of turbulent transport which are excited once critical temperature and/or density gradients are exceeded. Microinstabilities drive macroscopic turbulent eddies transporting particles, heat and momentum. The sizes and lifetimes of these eddies serve as the step size and characteristic time scale in the aforementioned ansatz to characterize the diffusion coefficients of turbulent transport. The microinstabilities can be grouped based

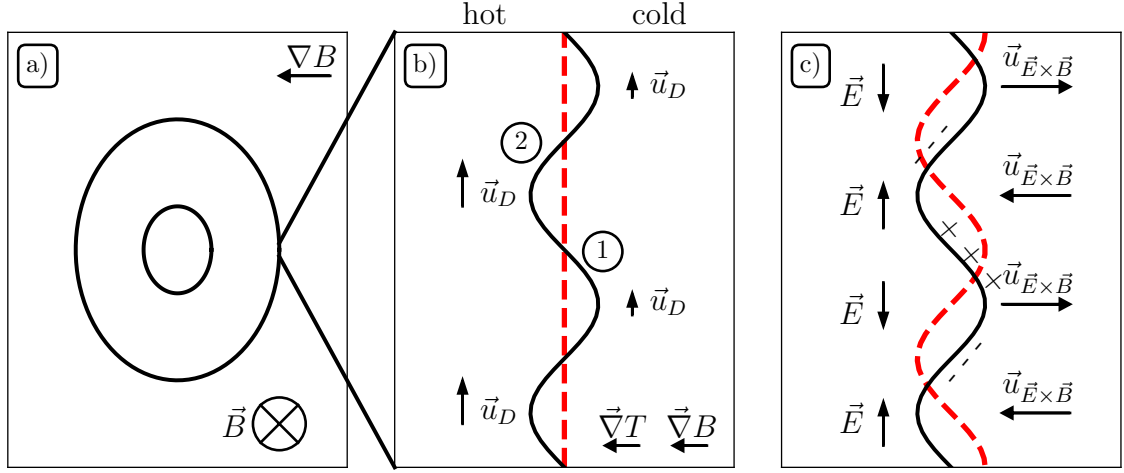


Figure 3.5: Simple model of ITG emergence: (a) sketch of plasma equilibrium with a magnetic field pointing into the plane, (b) initial periodic temperature variation (black) on the LFS leads to different drift velocities in the hot and cold region which (c) cause a variation in the periodic potential (red). The resulting electric field amplifies the initial drift wave. This figure is adapted from [82]

on their underlying physics' generation mechanism and two groups are of particular interest for this thesis which are the interchange and driftwave instability. Examples for the interchange instability are the ion temperature gradient (ITG) and electron temperature gradient (ETG) driven modes. One example where the driftwave instability is important is the trapped electron mode (TEM) that is caused by trapped electrons in the magnetic field topology. The aforementioned instabilities are briefly sketched in the following.

Interchange instability

The analogy to the Rayleigh-Taylor instability in hydrodynamics is the interchange instability in plasma physics [93]. It can be described as a 2D phenomenon and will be sketched for the ion temperature gradient mode in the following. Figure 3.5a shows a poloidal plasma cross section and an area treated on the LFS. For simplicity, the plasma is divided into two regions (hot and cold) and an initial perturbation is set up on the boundary between the two regions (see figure 3.5b). Due to the ∇B -drift introduced in equation (3.13), the ions will drift upwards. Ions in the hotter region drift faster than those from the cold region ($u \sim \sqrt{T}$) generating an area with higher ion density in point ① and with lower ion density in ②, i.e. a periodic perturbation of the ion density with a phase shift of $\pi/2$. The resulting electric field and $\vec{E} \times \vec{B}$ drift amplifies the initial perturbation: the hotter plasma is pulled further into the cold region and vice versa. This mode exists only on the LFS of the plasma. On the HFS, ∇B stays unchanged, but ∇T changes the direction such that resulting $\vec{E} \times \vec{B}$ flow reduces the initial perturbation.

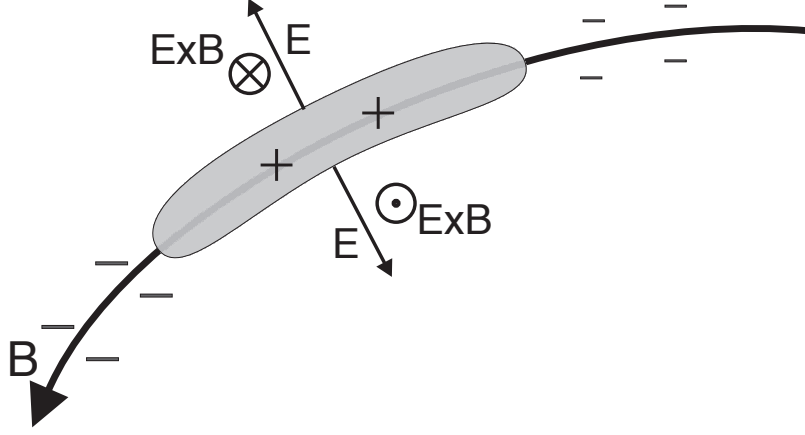


Figure 3.6: Illustration of the physics underlying the driftwave instability. The figure was taken from [16].

The ITG mode [94] is of particular importance for fusion plasmas since it is thought to be the primary source of ion heat transport in the core.

The equivalent ETG mode for electrons follows the same principle with the roles of ions and electrons switched. A major difference between the modes is the characteristic step size, which is the ion Larmor radius for ITG and electron Larmor radius for the ETG.

Driftwave instability

Compared to the interchange instability, the driftwave instability is a 3D phenomenon which can occur in an arbitrary magnetic field geometry and does not need a gradient in the magnetic field. For the driftwave instability, it is important that there is a perturbation parallel and perpendicular to the magnetic field where the wavenumber of the perpendicular perturbation is larger than the parallel one. Figure 3.6 illustrates the process underlying the driftwave instability with an initial density perturbation that is stretched in the direction of the magnetic field line. The mobile electrons react to the perturbation faster than the ions and move to regions with lower density. Thereby the positively charged ions are left behind in regions of higher pressure and regions of lower density are negatively charged by the electrons. Adiabatic electrons would not lead to transport since the perturbation in density and potential are in phase [16]. The response of the electrons is slowed down due collisions causing a phase difference between the density and potential perturbation leading to radial transport [44, 95].

3.3 Plasma rotation in toroidal geometry

The magnetic equilibrium in a tokamak configuration can be described by a right-handed coordinate system (r, θ, ϕ) (see section 1.2 and figure 1.4) and the magnetic field can be written as

$$\vec{B} = s_b F \nabla \phi + s_j \nabla \phi \times \nabla \psi, \quad (3.22)$$

where ψ is the poloidal magnetic flux (minimum on axis), $s_b = \text{sign}(R B_{\text{tor}})$ and $s_j = \text{sign}(\vec{B} \cdot \nabla \theta) = \text{sign}(\partial \psi / \partial \rho)$ indicate the direction of the magnetic field and plasma current with respect to the toroidal direction $\nabla \phi$ and poloidal direction $\nabla \theta$. s_b is defined in such a way that $F = R B_{\text{tor}} \geq 0$.

In section 3.1.2, it was shown that the Boltzmann equation can be re-written to lowest order as the force balance equation by applying the transport orderings introduced in section 3.2. Furthermore, it is accepted that flows are to lowest order incompressible such that the continuity equation leads to requirement of a divergence free flow: $\nabla \cdot \vec{u} = 0$ [88, 96, 97]. Section 3.1.3 showed, however, that the perpendicular plasma flow velocity (u_{\perp}) is given by the sum of $\vec{u}_{\vec{E} \times \vec{B}}$ and the diamagnetic velocity. The parallel flow has, therefore, to balance the divergence of the perpendicular flow:

$$\Rightarrow \quad u_{\parallel} = \frac{R B_{\text{tor}}}{B} \left[\frac{1}{q_{\alpha} n_{\alpha}} \frac{\partial p}{\partial \psi} + \frac{\partial \Phi}{\partial \psi} \right] + C B, \quad (3.23)$$

where an integration constant $C B$ has been added to account for general flows and Φ is the electrostatic potential. Together with the perpendicular flow:

$$\vec{u}_{\perp} = -\frac{R B_{\text{pol}}}{B} \left[\frac{1}{q_{\alpha} n_{\alpha}} \frac{\partial p}{\partial \psi} + \frac{\partial \Phi}{\partial \psi} \right] \vec{e}_{\perp} \quad (3.24)$$

$$\vec{e}_{\perp} = \frac{B_{\text{tor}}}{B_{\text{pol}}} \vec{b} - \frac{B R}{B_{\text{pol}}} \nabla \phi; \quad \vec{b} = \frac{\vec{B}}{B} \quad (3.25)$$

the total plasma flow is given by:

$$\vec{u} = \vec{b} u_{\parallel} + \vec{u}_{\perp} = C \cdot \vec{B} + \left[\frac{1}{q_{\alpha} n_{\alpha}} \frac{\partial p}{\partial \psi} + \frac{\partial \Phi}{\partial \psi} \right] R^2 \nabla \phi = C \vec{B} + \omega(\psi) R^2 \nabla \phi. \quad (3.26)$$

This equation shows that the total plasma flow can be expressed by a component parallel to the magnetic field and a rigid body rotation purely in the toroidal direction. This result is essential for this thesis since it enables the indirect reconstruction of u_{pol} through the measurement of the total plasma flow (see chapter 4) given by measurements of the toroidal plasma flow at two distinct points on the same flux surface. Some algebraic manipulations² allow the expression of the total plasma flow in the form:

$$\vec{u} = \hat{\omega}(\psi, \theta) \vec{e}_{\text{tor}} + \hat{u}(\psi, \theta) \vec{B} \quad (3.27)$$

²using the identity: $R^2 \nabla \phi = s_b F \frac{\vec{B}}{B^2} + s_j \frac{\nabla \psi \times \vec{B}}{B^2}$

where $\vec{e}_{\text{tor}} = R\nabla\phi$ and

$$\hat{\omega}(\psi, \theta) = \frac{\vec{u} \cdot \nabla\theta}{\vec{B} \cdot \nabla\theta}; \quad \hat{u}(\psi, \theta) = -s_j \left[\frac{\partial\phi}{\partial\psi} + \frac{1}{q_\alpha n_\alpha} \frac{\partial p}{\partial\psi} \right] \quad (3.28)$$

Here, the functions $\hat{\omega}$ and \hat{u} retain a dependence on the flux ψ and the poloidal angle. Assuming a stationary plasma density, i.e. there is no particle source and a negligible radial derivative of the radial particle flux at all poloidal angles, the poloidal dependency of $\hat{\omega}$ vanishes and \hat{u} can be approximated by the equation [40]:

$$\hat{u}(\psi, \theta) = \frac{K(\psi)}{n_\alpha(\psi, \theta)}, \quad (3.29)$$

where $K(\psi)$ is a constant on each flux surface. There is a remaining dependency of \hat{u} on the poloidal angle which results from the possible dependence of n_α on θ . There are two possible assumptions on n_α : first, that n_α is constant on a flux surface and second, that there is an asymmetry, which will be treated in the following.

3.3.1 Without impurity density asymmetries

Assuming a constant n_α on the flux surface, equation (3.29) reduces to $\hat{u}(\psi, \theta) = \hat{u}(\psi) = K(\psi)/n_\alpha(\psi)$ and the poloidal dependence of equation (3.27) vanishes entirely. Projecting equation (3.27) onto the toroidal direction, i.e. along $\nabla\phi$, and the poloidal direction, i.e. along $\nabla\phi \times \nabla\psi$, the plasma flow can be written as:

$$u_{\text{tor}} = \hat{\omega}(\psi) R + s_b \hat{u}(\psi) F(\psi)/R \quad (3.30)$$

$$u_{\text{pol}} = s_j \hat{u}(\psi) B_{\text{pol}} \quad (3.31)$$

Equation (3.30) implies that the two flux functions $\hat{\omega}$ and \hat{u} can be determined from two measurements of u_{tor} at the same flux surface. Preferably, these two locations are on the LFS and HFS, since the rigid body component $\hat{\omega} R$ depends on the difference between u_{tor} of the two points. The largest radial distance between the two points is given by the mid-plane values on LFS and HFS. Utilizing these values, the uncertainty of the measurement is minimized. According to equation (3.31), u_{pol} can then be reconstructed if the poloidal magnetic field is known, i.e. the magnetic equilibrium (see section 2.4).

Figure 3.7 illustrates the measurement principle for artificial data and the AUG coordinate system with positive toroidal magnetic field and plasma current ($s_b = -1$ and $s_j = -1$). From equation (3.31) it can be seen that a poloidal flow can only exist if $\hat{u} \neq 0$. Three different profiles for \hat{u} have been assumed: one with $\hat{u} = 0$ (black) and two with $\hat{u} \neq 0$ (red and blue). A linearly decreasing $\hat{\omega}$ profile is assumed (dashed green line) for all cases. Figure 3.7b shows the resulting u_{tor} profile and it can be seen from the figures 3.7c and d that an existing poloidal rotation creates an asymmetry in ω_{tor} . The direction of u_{pol} depends on the sign of $\Delta\omega_{\text{tor}} = \omega_{\text{tor,HFS}} - \omega_{\text{tor,LFS}}$: a positive value ($\Delta\omega_{\text{tor}} > 0$), i.e. ω_{tor} is larger on the HFS than on the LFS, indicates a poloidal flow in

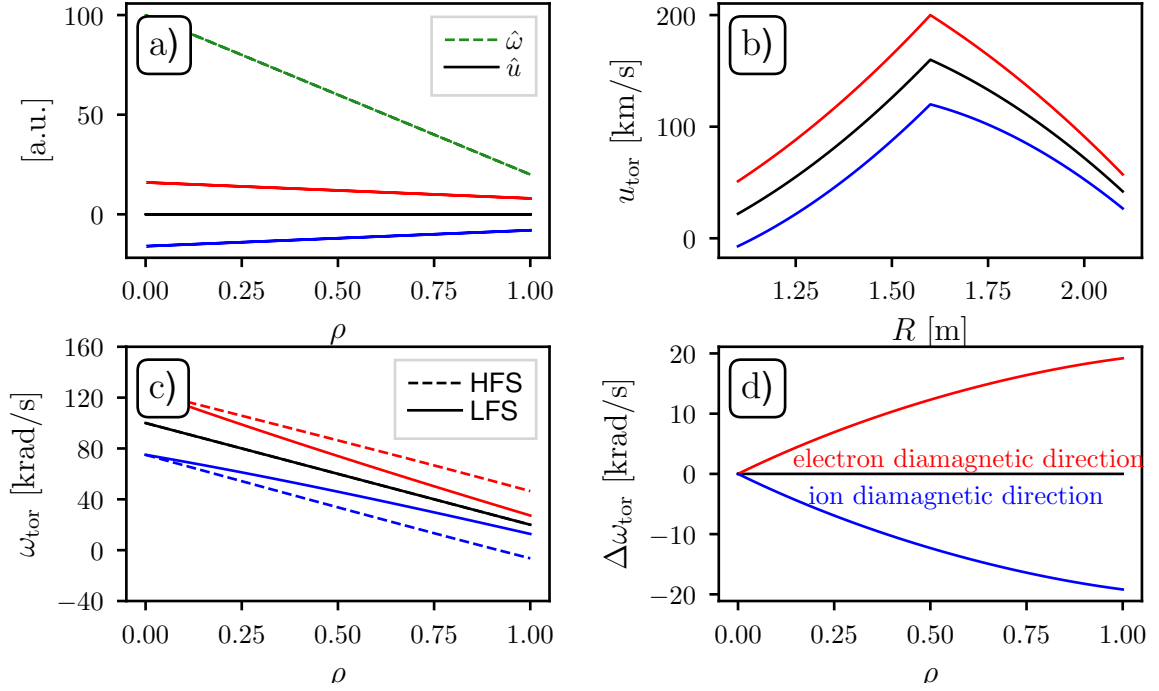


Figure 3.7: Illustration of the indirect measurement principle for three different \hat{u} profiles, without poloidal rotation (black) and with poloidal rotation (blue and red). (a) shows the assumed flux functions \hat{u} and \hat{w} . (b) illustrates the resulting u_{tor} profiles as a function of major radius and (c) shows the corresponding $\omega_{\text{tor}} = u_{\text{tor}}/R$ profiles. The difference between ω_{tor} on the HFS and the LFS is shown in (d) illustrating that there is a poloidal flow for the case that there is an asymmetry in ω_{tor} , where $\Delta\omega_{\text{tor}}$ is defined as $\Delta\omega_{\text{tor}} = \omega_{\text{tor,HFS}} - \omega_{\text{tor,LFS}}$. This example is done for the AUG coordinate system with positive plasma current and positive toroidal magnetic field.

the electron diamagnetic direction and a negative one to a flow in the ion diamagnetic direction.

3.3.2 With impurity density asymmetries

As it will be shown in section 5.4, impurity density (n_{imp}) asymmetries between LFS and HFS are a regularly observed feature for the outer half of the plasma. They start typically at $\rho_{\text{tor}} \gtrsim 0.6 - 0.7$ and the impurity density at the pedestal top on the HFS can reach values of up to 4 times the values on the LFS. For the case with an n_{imp} asymmetry, the poloidal rotation reconstruction shown above has to be adapted slightly. Assuming that the electrostatic potential is a flux function, a simple form for $K(\psi)$, defined in equation (3.29), can be derived by combining equations (3.27) and (3.28) using similar

steps as for the case without an impurity density asymmetry [40]:

$$K(\psi) = \frac{s_b}{F} \left(\frac{u_{\text{tor,HFS}}}{R_{\text{HFS}}} - \frac{u_{\text{tor,LFS}}}{R_{\text{LFS}}} - s_j \frac{T}{q_\alpha} \frac{\partial \ln n_{\alpha,\text{HFS}}/n_{\alpha,\text{LFS}}}{\partial \psi} \right) \left(\frac{1}{n_{\alpha,\text{HFS}} R_{\text{HFS}}^2} - \frac{1}{n_{\alpha,\text{LFS}} R_{\text{LFS}}^2} \right)^{-1}. \quad (3.32)$$

3.3.3 At high Mach numbers

The main result of this section, i.e equation (3.27), is not a formalism specific to neo-classical poloidal rotations. It is valid as long as the transport orderings shown in the previous section are valid, which is nearly always the case. A limitation for the application of the equation are, however, large toroidal flows with Mach numbers close to or larger than one. In that case the inertia term from equation (3.4) cannot be neglected in the approximation of the force balance. In this case, a more general form of the tokamak flow is [98]:

$$\vec{u} = \frac{U(\psi)}{n_\alpha} \vec{B} + R \left[\Omega(\psi) - \frac{1}{q_\alpha} \ln \left(\frac{n_\alpha}{n_{\alpha,p}} \right) \frac{\partial T}{\partial \psi} + \frac{m_\alpha}{2q_\alpha} (R^2 - R_p^2) \frac{\partial \Omega^2(\psi)}{\partial \psi} \right] \hat{e}_{\text{tor}}, \quad (3.33)$$

where $U(\psi)$ and $\Omega(\psi)$ are two unknown flux functions (similar to \hat{u} and ω in the previous equation), n_p and R_p are defined as impurity ion density at and major radius of the outboard mid-plane.

3.4 Neoclassical poloidal rotation

The previous section showed an approach to evaluate u_{pol} by measuring u_{tor} at two distinct points on the same flux surface. This section will show the expectations from neoclassical theory for u_{pol} .

3.4.1 Deriving the poloidal rotation for the plasma

Using the Hirshman and Sigmar moment approach [99], equations for the main ion and impurity ion poloidal rotation can be deduced from the flux-surface averaged momentum force balance equation (3.4). Neglecting external forces, the parallel electric field, and the electron contributions to the viscous and friction forces, the following equations can be calculated for a plasma with one impurity species α [100]:

$$u_{\text{pol,i}}^{\text{neo}} = \frac{1}{2} u_{\text{therm,i}} r_{\text{L,i}} \left(K_1 \frac{1}{L_{T_i}} \right) \frac{\vec{B} \cdot \vec{B}_{\text{tor}}}{\langle B^2 \rangle}, \quad (3.34)$$

$$u_{\text{pol,\alpha}}^{\text{neo}} = \frac{1}{2} u_{\text{therm,i}} r_{\text{L,i}} \left[(K_1 + 1.5K_2) \frac{1}{L_{T_i}} - \frac{1}{L_{p_i}} + \frac{Z_i}{Z_\alpha} \frac{T_\alpha}{T_i} \frac{1}{L_{p_\alpha}} \right] \frac{\vec{B} \cdot \vec{B}_{\text{tor}}}{\langle B^2 \rangle}, \quad (3.35)$$

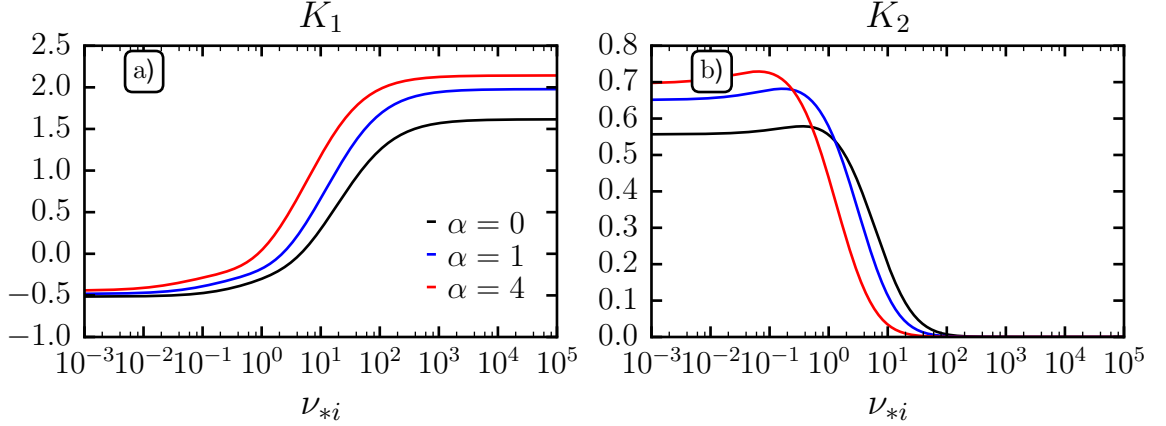


Figure 3.8: Dependence of the NC viscosity coefficients on the main ion collisionality and the impurity strength parameter $\alpha = n_Z Z_Z^2 / n_i Z_i^2$.

where $u_{\text{therm},i}$ is the thermal velocity of the main ions, $r_{L,i}$ the ion Larmor radius, K_1 and K_2 are the collisionality-dependent viscosity coefficients as defined in [100] and sketched in figure 3.8, and L_{p_i} the main ion pressure gradient length. It can be seen that the ion temperature gradient is crucial for the main and impurity ion poloidal rotation. While the ion pressure gradient is of importance as well for the impurity u_{pol} , the impurity pressure gradient plays only a minor role since it is multiplied with the charge ratio Z_i/Z_α .

In this thesis, equation (3.35) is used to compare experimental u_{pol} measurements with calculations from neoclassical codes such as NEOART[101], NEO[102] and NCLASS [103]. The last code is integrated into the TRANSP [104] package, which is used for transport analysis.

3.4.2 Poloidal flow damping

One important outcome of neoclassical theory is the strong damping of poloidal flows resulting from two different physical mechanisms. The first one, the more general one that is valid for all regimes of neoclassical theory, results from the fact that B_ϕ is larger on the inboard side (HFS) than on the outboard side (LFS). Due to the motion of the plasma parallel to the magnetic field, the plasma sees in its rest-frame a time-varying magnetic field by which it is periodically pinched (HFS) and stretched (LFS). The collisions lead to a transfer of the energy in the poloidal flow in the direction of the magnetic field (magnetic pumping effect) [23, 24].

The second mechanism is rather specific to the scattering of trapped and passing particles in the banana regime. For this regime, the parallel momentum change can be written as [97]:

$$n_i \frac{\partial u_{i,\parallel,p}}{\partial t} = \underbrace{\frac{\nu_{ii}}{\epsilon} \frac{c \epsilon^{1.5} T_i}{e B_{\text{pol}}} \frac{dn}{dr}}_{\text{trapped} \rightarrow \text{passing}} - \underbrace{\sqrt{\epsilon} \nu_{ii} n_i u_{i,\parallel,p}}_{\text{passing} \rightarrow \text{trapped}} = \sqrt{\epsilon} \nu_{ii} n_i \underbrace{\left[\frac{c T_i}{e n_i B_{\text{pol}}} \frac{dn}{dr} - u_{i,\parallel,p} \right]}_{=-u_{\text{pol}} B / B_{\text{pol}}}, \quad (3.36)$$

where p denotes the passing particles and ν_{ii} is the ion-ion collision frequency. This equation shows that any finite poloidal rotation will lead to an increase in the parallel velocity. Therefore, the expected poloidal rotation in NC theory results from the parallel motion along the magnetic field (which has a poloidal projection due to the pitch angle). In the banana regime, the poloidal flow damping can be understood as the friction between passing and trapped particles, with the trapped particles unable to rotate poloidally.

The concept of poloidal flow damping is taken into account in the poloidal projection of the momentum conservation equation (3.4) where the viscous stress tensor occurs [23]:

$$\langle (\nabla \Pi)_\theta \rangle = \alpha (u_\theta - u_\theta^{\text{neo}}), \quad (3.37)$$

where α expresses the time-scale on which the poloidal velocity is damped to its neo-classical value and depends on plasma parameters and especially on the collisionality. In general, the process occurs on time-scales of the ion-ion collision time.

3.5 Plasma confinement

It was shown in section 1.1 that good plasma confinement is needed to achieve thermonuclear conditions and plasma ignition. The global energy confinement time is defined as the ratio of the thermal stored energy of the plasma W_{th} and the net input power P_{net} , i.e. the injected heating power P_{inj} minus the temporal derivative of the thermally stored plasma energy $\partial W_{\text{th}}/\partial t$:

$$\tau_E = \frac{W_{\text{th}}}{P - \frac{\partial W_{\text{th}}}{\partial t}}; \quad W_{\text{th}} = \int \frac{3}{2} n (T_i + T_e) dV, \quad (3.38)$$

where V is the plasma volume. The confinement of the plasma is limited by radial transport, radiation losses, thermal conduction and convection processes [44]. In section 3.2 it was shown that the experimentally measured transport is significantly larger than predicted from neoclassical theory. In order to address the physics defining τ_E , it was explored empirically using scaling laws. Unfortunately, there is not a single scaling law that can describe the confinement time adequately for all experiments. Instead, different confinement regimes have been found. The two most known ones are the low and the high confinement mode (L- and H-mode). In the following, the L-mode will be split into plasmas with and without auxiliary heating.

3.5.1 Ohmically heated L-mode plasmas

In the early 1970 at the Tokamak-3 operated in Moscow, it was found that τ_E increases linearly with n_e and plasma current I at low plasma densities: $\tau_E \sim \langle n_e \rangle^{0.5} a I$ [106]. In later scalings, the current dependency vanished due to its strong correlation with the plasma density [107, 108]. Combining experimental data from various tokamaks a

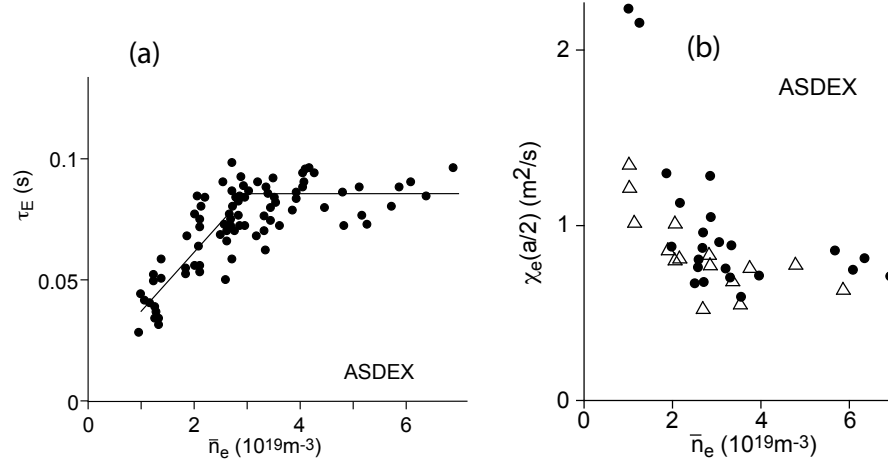


Figure 3.9: Energy confinement time (a) and electron thermal diffusivity χ_e (b) as a function of line-averaged electron density for ohmically heated discharges in ASDEX. The circles and triangles correspond to plasma currents of 380 and 320 kA, respectively. At the LOC-SOC transtion, χ_e becomes independent of n_e . This figure is adapted from [105].

scaling for the so-called linear Ohmic confinement regime was derived [109]:

$$\tau_E \sim n_e^{0.9} a^{0.98} R^{1.63} Z_{\text{eff}}^{0.23} \quad (3.39)$$

where a is the minor, R the major radius of the plasma and Z_{eff} the effective ion charge. Assuming low radiation losses and discharges with a small impurity content, the following scaling was derived: $\tau_E[\text{s}] = 0.07 (n/10^{20}) a R^2 q$ [110]. The linear increase of τ_E with n lead to optimistic concepts for future fusion reactors which were designed at a rather moderate sizes [111].

In 1979 it was, however, found at the ISX-A tokamak that τ_E saturates above a critical n_e (see figure ??a and figure 3.10a) [112]. In the subsequent years, this behavior was confirmed in a large number of tokamaks [105, 113, 114] and a scaling for the saturation density was derived [44]:

$$n_{e,\text{sat}} = 0.6 \cdot 10^{19} I R A^{0.5} \kappa^{-1} a^{-2.5} \quad (3.40)$$

where $\kappa = b/a$ is the elongation of the plasma with a and b being the half axes of an elipse. An example of the transition from the linear to the saturated Ohmic confinement can be seen in the figures 3.9a and 3.10a for an ASDEX and an AUG discharge, respectively.

One hypothesis that has been considered for a long time is that the transition from the LOC to the SOC regime is due to a change in the dominant turbulence regime from trapped electron mode in LOC to ion temperature gradient in SOC [91, 112, 114–116]. The increase in τ_E in LOC is attributed to two super imposed mechanisms: first, the electron thermal diffusivity (see figure 3.9b) decreases with increasing n_e and, second, an increase in n_e improves the coupling of the electrons to the ions, which confine the

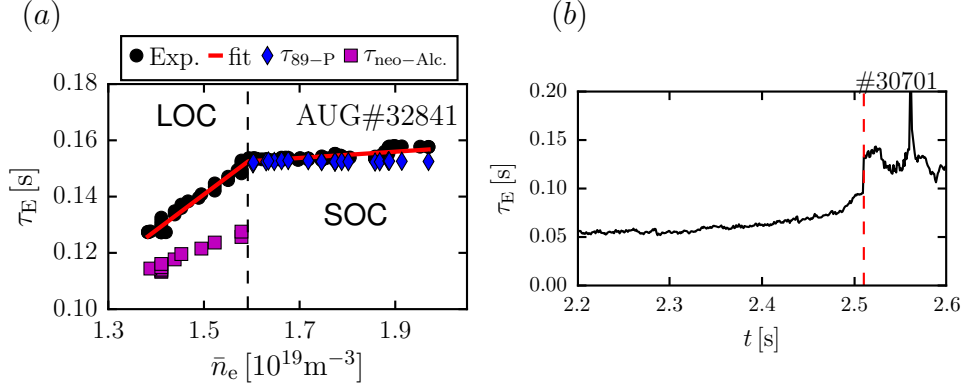


Figure 3.10: (a): Comparison of the experimentally measured τ_E (black circles) to two different scalings: the neo-Alcator scaling (purple squares) [110] for the LOC regime and the ITER89-P L-mode scaling [122] (blue diamonds). (b): τ_E as a function of time for a discharge with a transition from L- to H-mode. At 2.5 s, the amount of neutral beam heating is increased leading to a sudden increase of τ_E by a factor of 2.

energy better due to their lower temperature gradient. In the SOC regime, the thermal diffusivity of electrons and ions become independent of n_e (see figure 3.9b) such that an increase in n_e does not affect τ_E anymore and the energy transport is covered by the ions. The physics pictures of the LOC-SOC transition emerged through experiments at various machines: ASDEX [105], FT [117], FTU [118] and Tore Supra [119].

Recent gyrokinetic simulations done at AUG [120] suggest, however, that the LOC-SOC transition is not determined by a change from TEM to ITG driven turbulence. It is rather the ion energy transport that gets stronger at higher densities. The TEM to ITG transition is, however, necessary to explain the observation of the electron density peaking seen in the parameter regime of the LOC-SOC transition [121].

To date, experimental observations have not been able to either confirm or refute the underlying physics of this picture and the LOC-SOC transition requires further assessment. In chapter 7 the discussed technique will be applied to measure the radial electric field and, thereby, to extract the turbulent phase velocity, which is indicative for the turbulence regime.

3.5.2 L-mode plasmas with additional auxiliary heating

In order to increase the energy content of the plasma, additional heating was applied using neutral particle injection or electromagnetic waves (see section 2.2). The results in the beginning were, however, quite disappointing since it was found that the confinement degrades with increasing heating power [110]:

$$\tau_{E,\text{Goldston}} [\text{s}] = 0.037 \cdot \frac{I [\text{MA}] R^{1.75} [\text{m}] \kappa^{0.5}}{P^{0.5} [\text{MW}] a^{0.5} [\text{m}]} \quad (3.41)$$

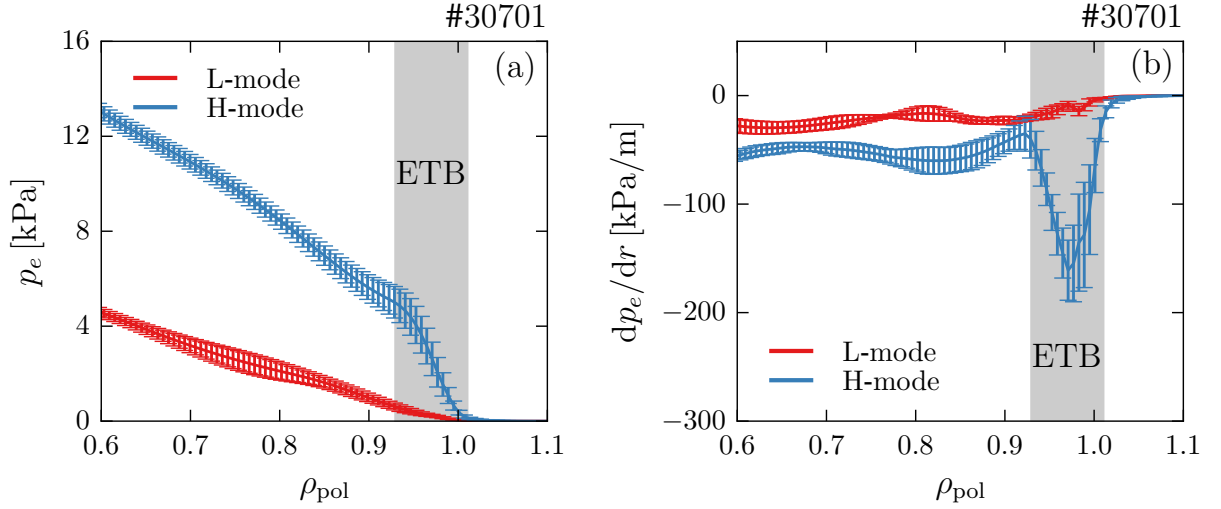


Figure 3.11: Electron pressure profiles p_e (a) and gradients dp_e/dr (b) in L- (red) and H-mode (blue). The increase of the pressure results from the steepening of the gradient in a small region close to the separatrix (edge transport barrier, ETB). This figure has been adapted from [124].

This scaling was derived before large tokamaks, like JET, went into operation. The power degradation ($\tau_E \propto P^{-0.5}$) remained with the revisited 'ITER89-P' L-mode scaling [122].

In 1982, it was found at ASDEX that, under certain plasma conditions, an abrupt transition to higher confinement [123] is possible. An example for this behavior can be seen in figure 3.10b for a discharge of AUG. In the beginning, the plasma is in L-mode and the usage of additional auxiliary heating (red dashed line) leads to an increase in τ_E by a factor of roughly 2. This discovered high confinement mode (H-mode) is a promising operation scenario for future fusion devices.

3.5.3 High confinement mode (H-mode)

It can be seen easily from equation (3.38) that an increase in the electron and ion pressure at constant volume and heating power will lead to an improvement in τ_E . This is exactly what happens in the high confinement mode. The electron and ion pressure increase when the applied heating power is above a certain auxiliary power threshold [125, 126]. From figure 3.11, it can be seen that the increase results mostly from larger gradients in the plasma edge where a pedestal is formed. This region is known as the edge transport barrier (ETB). In the plasma core, it has been observed that the profiles are rather stiff, i.e. there are only small changes observed in the normalized temperature and density gradient lengths (L_T and L_n) even over large parameter variations [127, 128]. This behavior is thought to be a result of a threshold in the turbulent transport instabilities on the gradients such that above a certain gradient the transport is largely increased and changes in the applied heating power will only have a small effect on the plasma profiles. In the edge, however, the turbulence is believed to be largely suppressed in the

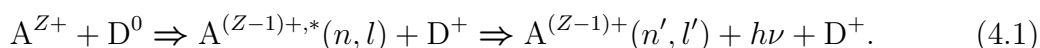
H-mode due to the strong radial electric field and the associated $\vec{E} \times \vec{B}$ shear flow, which is thought to stabilize turbulence. Therefore, a strong increase of the plasma pressure can be maintained in that region. Due to the core profile stiffness, the increase gained in the plasma edge leads to an overall increase in the plasma pressure and, thus, in confinement.

Chapter 4

Charge Exchange Recombination Spectroscopy at AUG

4.1 Measurement principle

Charge exchange recombination spectroscopy (CXRS) [129, 130] is the most common plasma diagnostic to measure T_i , u_{tor} , u_{pol} , and n_{imp} in present day tokamaks. This technique exploits the line radiation emitted during the charge exchange process between neutral atoms, typically D or H, and impurity ions (A) with charge Z :



Here, n is the principle and l the orbital quantum number. The recombination process (first arrow) leaves the impurity ion in an excited state $\text{A}^{(Z-1)+,*}$. This state has a certain lifetime, after which it decays and emits a photon $h\nu$ with an energy corresponding to a characteristic wavelength λ (second arrow). The charge exchange (CX) reaction tends to populate high energy and angular momentum levels with a maximum in the distribution at around $n \approx Z^{0.75}$ [129]. The spectroscopic observation of the emitted photons with dedicated systems is known as CXRS. Emissions from CX reactions cover the X-ray, ultra violet, and visible spectral regions. CXRS, however, is typically focused on the visible spectral lines for which high resolution spectrometers, lens fiber optics, and high quantum efficiency detectors are readily available.

Figure 4.1b shows an example spectrum and illustrates the measurement principle further: the spectrum consists of two contributions. The *active* component results from CX processes between high energy deuterium neutrals injected with the NBI sources at AUG and fully stripped impurity ions inside the plasma ($\rho < 1$). The *passive* component originates from CX processes with thermal deuterium located at the plasma edge ($\rho \geq 1$) and electron or ion impact excitation of hydrogen like impurity ions. The CXRS measurement gives, in principle, line-integrated results and collects the radiation from both, the active and the passive components. Due to the different temperatures and rotations in the different regions of the plasma, these two components are separated in wavelength and line broadening and can be distinguished as is shown in figure 4.1b.

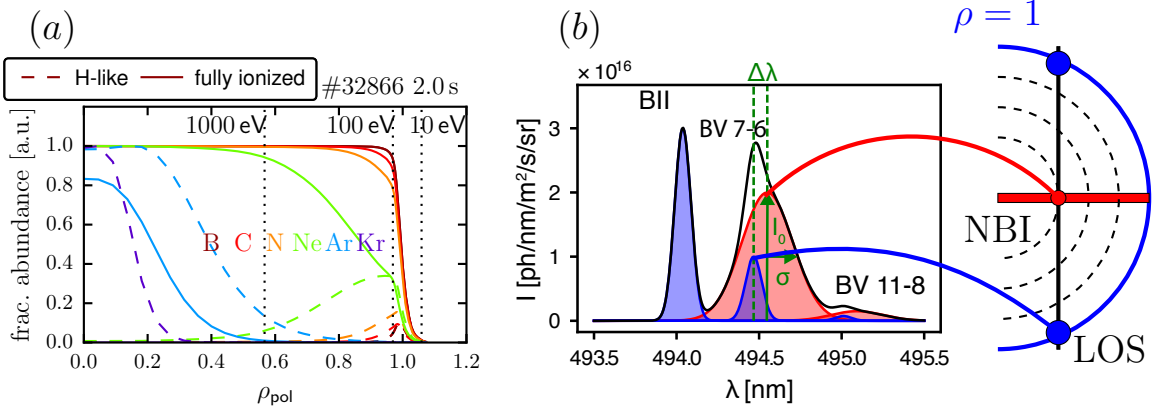


Figure 4.1: (a): Fractional abundance for the H-like (dashed line) and fully ionized (solid line) charge states of boron (B), carbon (C), nitrogen (N), neon (Ne), argon (Ar), and krypton (Kr) in an AUG plasma. The charge state distribution is normalized to the maximum density occurring for the hydrogen-like or fully ionized ion. These calculations have been performed using the impurity transport code STRAHL [131, 132]. (b) Example for a typical boron CX spectrum measured in the plasma core. The total spectrum consists of three spectral lines (BII, BV 7-6, and BV 11-8) with contributions from two different regions in the plasma: The active components (red) come from the intersection volume between the LOS and the NBI source. The passive components (blue) originate from a volume close to the separatrix where the impurity ion is not fully stripped. The CXRS quantities of temperature, rotation, and density are evaluated from the Doppler broadening σ , the Doppler shift $\Delta\lambda$, and the integrated intensity I , respectively.

There are two NBI operation scenarios regularly used for the CXRS at AUG. In the first scenario, the NBI source is operated with a constant power (see for example figure 1.5a) and a fit with a Gaussian has to be used for each active and passive component to deduce the CXRS quantities (see figure 4.1b). In the second scenario, the NBI source is switched on and off with a certain duty cycle (NBI blips, see for example figure 7.2b). Here, the frames before and after the beam blip can be used to determine the passive spectrum (blue components in figure 4.1b) and, therefore, the active signal (red components in figure 4.1b) can be isolated by subtracting off the passive signal. The latter method enables, in general, to fit the spectra with a higher accuracy since the passive and active contributions do not have to be separated with the fit.

CXRS focuses typically on low- Z impurities such as B, C, and N rather than high- Z elements and main ions. This is partially due to the fact that high- Z elements are usually not fully-stripped inside the plasma (see figure 4.1a). From this figure it can be seen that the typically observed impurity ions (B, C, and N) are fully stripped at the pedestal top, i.e. at a normalized radius of $0.9 < \rho_{pol} < 0.95$, and there is only a small fraction of hydrogen-like impurity ions inside the plasma leading to an additional CXRS contribution in between the active and passive parts in figure 4.1a. Impurity ions with higher charge numbers, such as Ne ($Z = 10$), Ar ($Z = 18$), and Kr ($Z = 36$) tend to have a significant fraction of hydrogen-like impurity ions inside the plasma such that a

clear distinction between active and passive signals is more complicated and needs Abel inversion techniques to reconstruct profiles of the CXRS quantities. Additionally, the atomic data for non hydrogen-like atoms and high- Z elements is not that reliable and harder to compute such that the measurement is then mostly restricted to partial profiles (i.e. for example densities of certain charge states in the plasma instead of the impurity density).

The line radiance observed along a LOS of a CXRS diagnostic is given by [129]:

$$L_{\text{CX}}(\lambda) = \frac{h\nu}{4\pi} \sum_{j=1}^M \sum_{n=1}^{n_{\text{max}}} \int_{\text{LOS}} \langle \sigma_n v \rangle_{j,\text{eff}} n_{\alpha,Z} n_{\text{N},j,n} dl, \quad (4.2)$$

where $n_{\alpha,Z}$ is the density of the impurity ion α with charge Z , $n_{\text{N},j,n}$ is the neutral density with j corresponding to the summation over M neutral components and n being the main quantum number, and l the coordinate along the LOS. There are typically 3 energy components for hydrogen beams and a cloud of neutral atoms around the NBI source in the plasma volume to be considered (such that $M = 4$). In general, it is sufficient to consider only the atomic states $n = 1, 2$, since the population density of higher states is very low. $\langle \sigma_k v \rangle_{j,\text{eff}}$ is the effective rate coefficient, where $\langle \rangle$ denotes the Maxwellian average over the cross-section σ_n and the relative velocity v between the neutral atom and the impurity ion, i.e. $v = |v_{\text{N},n} - v_{\alpha,Z}|$. Assuming a constant impurity density throughout the observation volume, equation (4.2) can be used to calculate the impurity density in the plasma:

$$n_{\alpha,Z} = \frac{4\pi}{h\nu} \frac{L_{\text{CX}}(\lambda)}{\sum_j \sum_n \langle \sigma_n v \rangle_{j,\text{eff}} \int_{\text{LOS}} n_{\text{N},j,n} dl} \quad (4.3)$$

The energy distribution of the impurity ions is given by a Maxwellian distribution such that the measured spectra obtained from CXRS have a Gaussian line shape [81]:

$$I_{\text{CX}}(\lambda) = I_0 \exp \left(-\frac{1}{2} \frac{(\lambda - \lambda_0 - \Delta\lambda)^2 m_{\alpha} c^2}{\lambda_0^2 T_{\alpha}} \right), \quad (4.4)$$

where λ_0 is the rest-wavelength of the transition, $\Delta\lambda$ the associated Doppler shift due to a finite rotation of the species, m_{α} the mass and T_{α} the temperature of the impurity species. The observed temperature is, therefore, given by the Doppler broadening:

$$T_{\alpha} = \frac{m_{\alpha} c^2}{\lambda_0^2} \sigma^2, \quad (4.5)$$

where σ is the standard deviation. In this work, it is assumed that the impurity temperature is equal to the main ion temperature. The thermal equilibration time between impurities and main ions [133] is on the order of μs and, therefore, short compared to local transport time scales (ms). Thus, the temperature of all ions will be denoted as T_i and no distinction between different species will be made throughout this thesis.

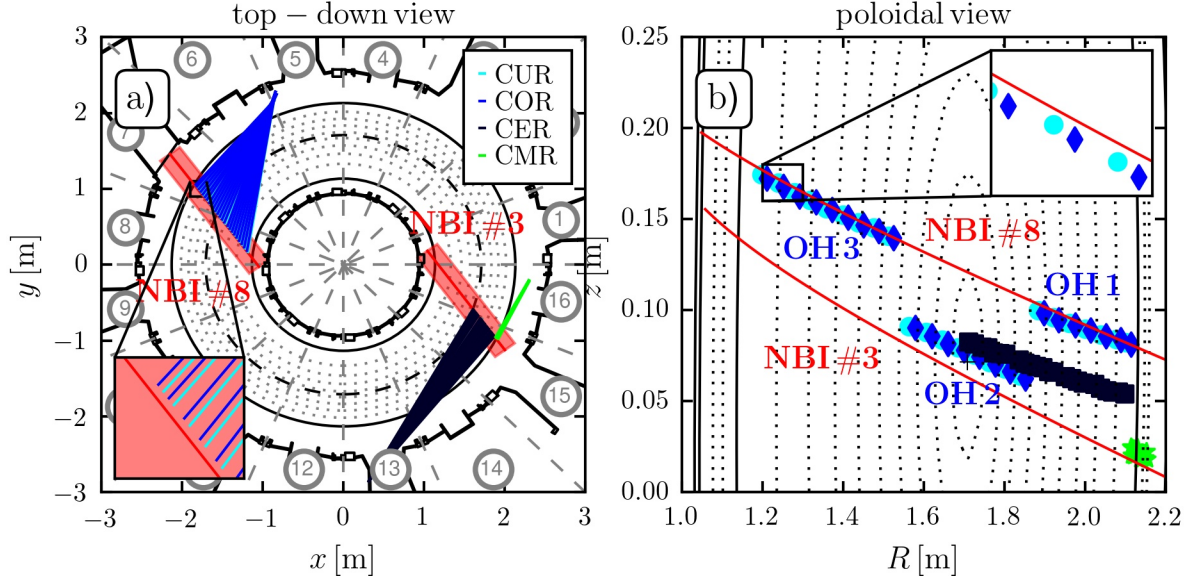


Figure 4.2: Overview of the LOSs of the main toroidal CXRS systems at AUG: (a) top-down view (b) poloidal view. The main core CXRS diagnostics relevant for this thesis are COR (blue), CUR (cyan), and CER (black) which are aligned along the NBI sources 3 and 8. Additionally, the edge toroidal CXRS system, CMR, is shown in green. The dotted lines represent the magnetic flux surfaces.

The Doppler shift of the emitted line ($\Delta\lambda$) is directly connected to the rotation velocity of the observed species ($\vec{u}_{\text{rot},\alpha}$):

$$\frac{\Delta\lambda}{\lambda_0} = \frac{\vec{u}_{\text{rot},\alpha} \cdot \vec{e}_{\text{LOS}}}{c}, \quad (4.6)$$

where c is the speed of light and \vec{e}_{LOS} the unit vector along the LOS.

4.2 Toroidal CXRS systems at AUG

The ASDEX Upgrade tokamak is equipped with several CXRS systems covering the plasma from the pedestal top on the HFS to the scrape-off-layer (SOL) on the LFS at the mid-plane. An overview of some of the available CXRS diagnostics is given in figure 4.2.

Three new toroidal optical heads, OH1, OH2, and OH3, were installed along the NBI source 8 for this thesis giving in total 70 LOSs covering the full minor radius (i.e. from the pedestal top on the LFS to the pedestal top on the HFS) [42]. OH1 is equipped with 20 LOSs imaging the LFS of the plasma from a major radius of 1.89 to 2.13 m. OH2 covers a major radius from 1.57 to 1.86 m and has in total 23 LOSs. Lastly, OH3 is equipped with 27 LOSs and covers the HFS of the plasma from a major radius of 1.2 to 1.54 m. Compared to the other two optical heads, OH2 is shifted slightly downwards in z enabling measurements close to the magnetic axis (see figure 4.2b).

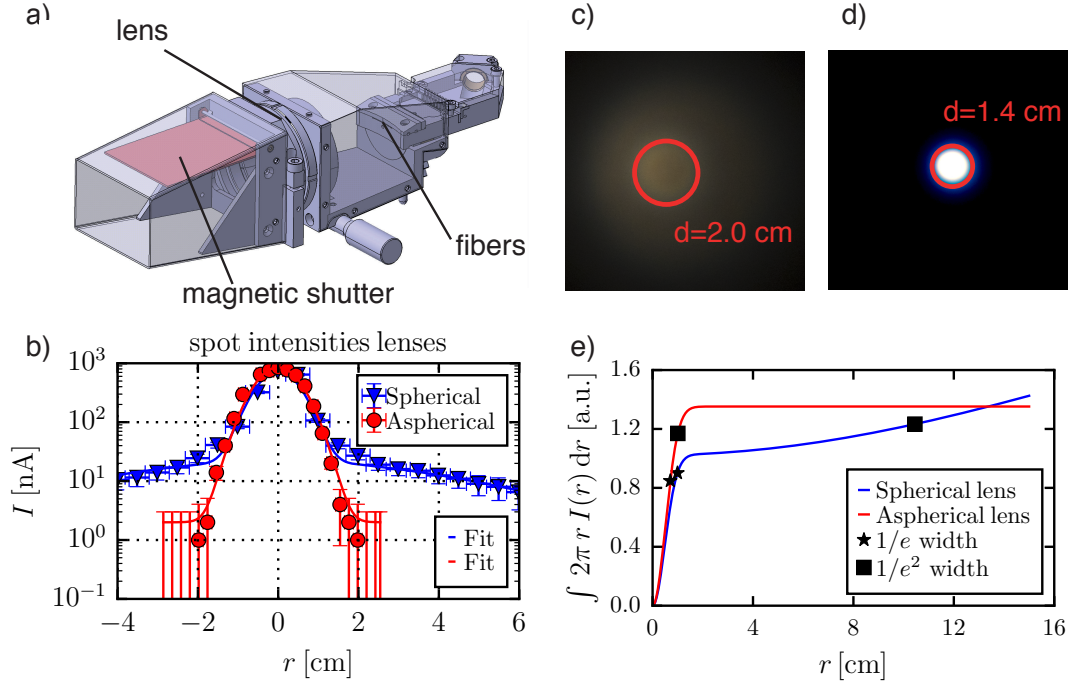


Figure 4.3: (a): CAD drawing of the optical head illustrating the position of the array of fibers, the lens and the magnetic shutter; (b): Comparison of the resulting spot-sizes using a spherical ($f/\# = 1.8$, blue) and an aspherical lens ($f/\# = 1.6$, red); image of spot-sizes for spherical (c) and aspherical (d) lenses; (e): Intensity distribution of light around center.

The optical heads (see figure 4.3a) have a fairly simple design: $400\ \mu\text{m}$ ($f/\# = 2.2$) silica fibers are placed behind an aspherical lens where the distance matches the focal length of the lens (50 mm diameter, 80 mm focal length, and $f/\# = 1.6$). Previously, standard spherical lenses were used with $f/\# = 1.8$. However, these lenses collected light from a large area (halo) around the focused light-spot (see figure 4.3c) compared to the aspherical lenses (see figure 4.3d). Through measurements of the light distribution with a diode (the light intensity is then proportional to the current of the diode, see figure 4.3b), it is possible to determine the $1/e$ width ($w_{1/e}$) and $1/e^2$ width (w_{1/e^2}) of the image from both lenses, i.e. the diameter of the spot-size including 63 and 86 % of the light. Using the aspherical lens, the $w_{1/e}$ width was reduced from 2.0 to 1.4 cm (by 30 %) and the w_{1/e^2} width from 21 to 2 cm (by 90 %) (see figure 4.3e). The lenses of the optical heads are protected from possible dirt and coatings occurring during glow discharges and boronizations by a magnetic shutter that is only open when the toroidal magnetic field is switched on (see figure 4.3a).

The collected light is transmitted by glass fibers with a diameter of $400\ \mu\text{m}$ to a high through-put ($f/\# = 2.8$) Czerny-Turner like spectrometer (see figure 4.4b). The fiber bundle is collimated with a variable entrance slit that is typically set to $100\ \mu\text{m}$ for standard operation. This setting was found to be optimal for the simultaneous measurement

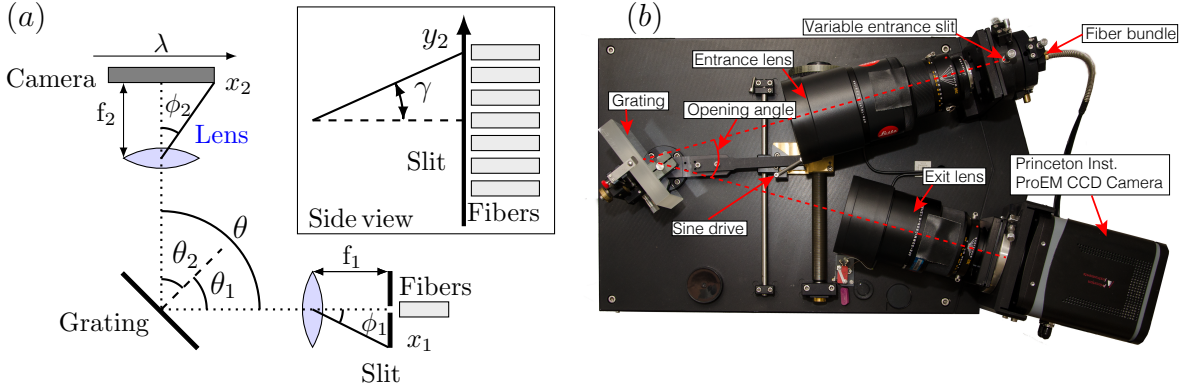


Figure 4.4: Schematic drawing (a) and image (b) of the high through-put $f/\# = 2.8$ spectrometer measuring the CXRS spectra on the LFS and HFS. The fibers are bundled in front of the variable entrance slit. The light from the fibers is collimated by an objective lens (entrance lens) with a focal length of $f_1 = 280$ mm onto a grating with 2400 grooves/mm controlled by a sine drive and is focused onto a high quantum efficiency CCD camera by an objective lens (exit lens) with $f_2 = 180$ mm. The opening angle between entrance and exit lens is $\theta = 30^\circ$.

of the LFS and HFS with one spectrometer¹. This results, however, in a non-Gaussian instrument function which is approximated with 5 Gaussians (see section 4.3) in order to be able to use the standard fitting tool CXSFIT [134], which can only treat Gaussian instrument functions. The spectrometer consists of two objective lenses with focal lengths of 280 mm ($f/\# = 2.8$, entrance lens) and 180 mm ($f/\# = 2$, focusing lens) and a grating with 2400 grooves/mm put onto a sine drive. The opening angle θ between the two objective lenses is 30° . The light from 25 vertically aligned fibers (see figure 4.4a) is focused onto a high efficiency CCD ProEM camera from Princeton Instruments [135]. The CCD chip has an active area of 512×512 pixels and a readout area of 528×512 pixels. The maximal time resolution of the spectrometer is set by the readout frequency ($f_{RO} = 10 \times 10^6$ pixels/s), the shifting-time of pixels from the active to the readout area ($v_s = 0.6 \mu\text{s}/\text{row}$), and an offset required to clean the serial register of the camera and to apply the pixel bias correction. By vertically binning the rows of the CCD to one channel, the number of rows on the camera that are readout are reduced (from 512 to 25) and, hence, the time resolution of the system is increased. The area onto which one fiber is images on the CCD camera is thereby called region of interest (ROI). The maximum repetition rate for the spectrometer is $\Delta t = 2.41$ ms for 25 ROIs.

The camera is typically operated in the continuous frame transfer mode, i.e. the CCD chip is simultaneously exposed and readout. Charges that are transferred to the storage area, therefore, cross areas of the chip that are illuminated during the next exposure. This creates a smearing of the transferred exposure. To measure the smear, there is one

¹Due to the beam attenuation, the signal level is significantly lower on the HFS (see figure 4.12e) compared to the LFS. The rather large slit width was chosen to gather as much signal as possible at a reasonable exposure time of the camera.

channel of the spectrometer not connected to the optical heads. With the measured smear from this channel, the smear from the other channels can be corrected as well.

The total shift time of the chip is 0.31 ms ($512 \times v_s$) such that the smear is a $\frac{0.31 \text{ ms}}{2.5 \text{ ms}} = 12\%$ effect at the maximum time resolution and a 3% effect at the standard time resolution of 10 ms . Theoretical calculations of the smear can reproduce the measured smear within 10% such that the uncertainty from the smear is on the order of 1% for the maximal integration times [42]. The frame transfer mode offers, therefore, a good opportunity to measure the CXRS with no lag time in between exposures.

Using the sine drive of the spectrometer the tilt of the grating can be changed (i.e. the angles θ_1 and θ_2 of figure 4.4a) and, thus, different wavelength regions imaged onto the camera. This enables the investigation of different impurity species. The CXRS system typically observes the B V ($n = 7 \rightarrow 6$) emission line at 494.467 nm or the N VII ($n = 9 \rightarrow 8$) emission at 566.937 nm . The central wavelength of the camera is calibrated after each plasma discharge with a Ne pen-ray lamp that emits Ne lines at specific wavelengths. This lamp is connected to the same channel used for the measurement of the smear effect and is switched on 15 s after the plasma discharge (see the following section).

4.3 Characterization and calibration of CXRS diagnostics

In order to interpret the CXRS measurements, a precise calibration of the whole system is necessary. The different steps and techniques used for the calibration of the different parts of the CXRS system are outlined in the following.

Spatial alignment

The determination of the 3-D LOS geometry defined by the alignment of the optical heads is performed by connecting a lamp emitting a broadband spectrum (white light) to the LOS from the laboratory. Thereby, the LOSs trajectories are illuminated in the plasma vessel. The optical head positions are aligned such that the lines-of-sight are focused onto the center of the NBI source in order to get the maximum CXRS signal. The trajectory of each LOS is determined by measuring the lens position of the optical head and several points along the LOS using a 3-D robotic arm placed inside the vacuum vessel. Knowing the mounting point of the robotic arm and the positions of the different robot joints, the absolute position of the LOS can be determined in the machine coordinate system with an accuracy of about 1 mm [136]. By fitting the measured points, the LOS trajectory can be determined with an error smaller than 1 mm .

The point along the LOS closest to the center of the NBI source corresponds not necessarily to the effective measurement position of the CXRS signal. According to equation (4.2), the line radiance of the LOS is proportional to the neutral distribution of the beam n_0 and the impurity density, where n_{imp} is assumed to be constant along the LOS. It is, therefore, the center-of-mass of the neutral distribution determining the effective measurement position of the LOS. Figures 4.5a-c shows the neutral distribution for three different LOS with respect to R and z , where n_0 has been calculated with the

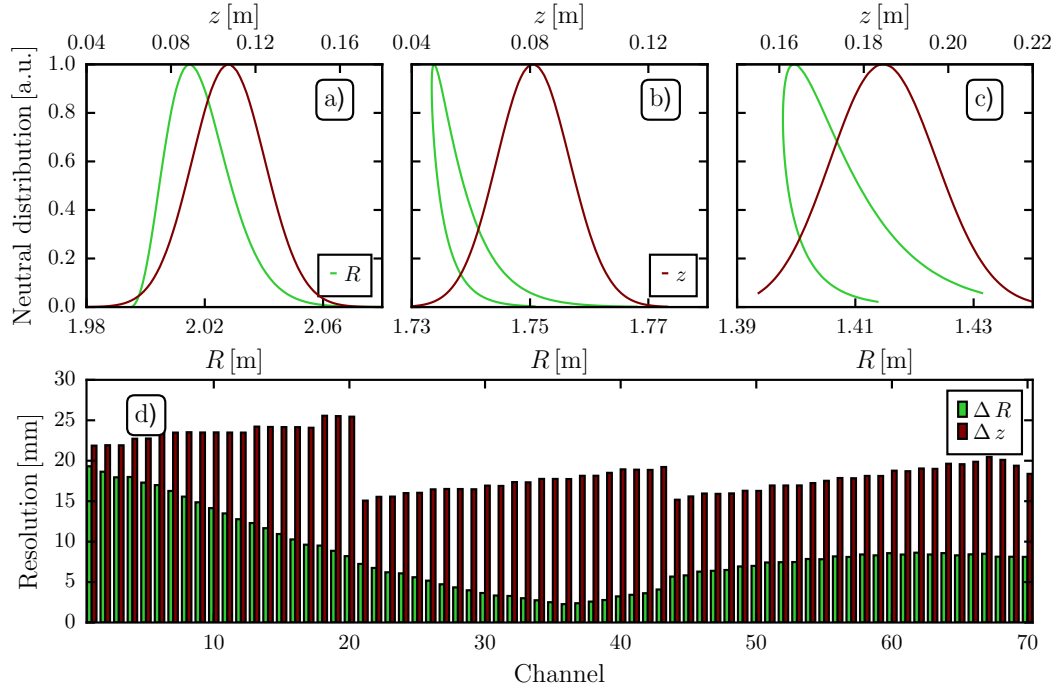


Figure 4.5: The spatial resolution of the 70 LOSs of the COR head can be obtained by calculating the neutral density distribution along the line-of-sight. (a)-(c) shows the neutral distribution along the LOS for three different fibers ('COR-10', 'COR-31', and 'COR-55') with respect to R (green) and z (maroon). The $1/e$ -width of this distribution gives the spatial resolution of the LOS (d).

neutral particle transport code FIDASIM [137]. The spatial resolution of the LOS is given by the $1/e$ -width of n_0 , which is 2.3 to 19 mm in R and 15 to 26 mm in z for all 70 LOSs (see figure 4.5d).

Intensity calibration

The intensity calibrations of the diagnostics are necessary to measure the impurity content of the plasma. In practice, the measured counts at the camera have to be converted to photons and, therefore, the sensitivity of the system has to be measured. The sensitivity, i.e. the efficiency of the system to measure counts for incoming photons (as a function of wavelength), is measured by using a standard integrating sphere (Labsphere, Model Unisource 1200) with a known spectral radiance (see figure 4.6a). In order to characterize the optical system two different sensitivities are necessary²: the optical head sensitivity and the spectrometer sensitivity. The latter sensitivity can be obtained by connecting the fibers from the entrance slit of the spectrometer to the integrating sphere (see figure 4.6c) and in order to measure the optical head sensitivity, the integrat-

²In principle, it is sufficient to characterize the transmission of the system with one measurement. In order to enable fiber and camera switching between different CXRS diagnostics at AUG two transmission curves are measured.

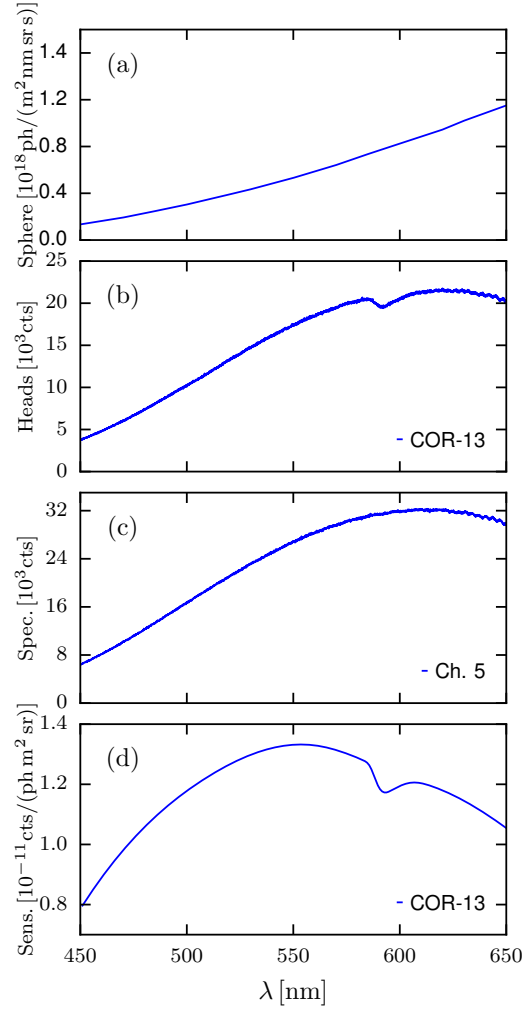


Figure 4.6: Intensity calibration for one LOS of the COR head: A light source with a known emission (a) is used for the calibration of the optical head (b) and the spectrometer (c). The resulting sensitivity for the LOS is shown in (d).

ing sphere is placed in front of the optical head inside the vessel (see figure 4.6b). The sensitivity is recorded in the wavelength region between 450 to 650 nm, which covers all of the CXRS spectral lines used during operation.

The sensitivity curve for the optical head (see figure 4.6b) shows a dip at roughly 600 nm resulting from the glass fiber absorption. This feature should in principle be visible in the sensitivity curve of the spectrometer as well (see figure 4.6c). Due to the fact that the glass fiber length between the spectrometer and the calibration sphere is far shorter (1 m) compared to the fibers guiding the light from the torus to the spectrometer laboratory (60 m), this feature is not visible in figure 4.6c. Through the comparison of the measured counts with the emitted photons from the light source, the sensitivity of the system can be calculated as a function of the wavelength (see figure 4.6d). The typical

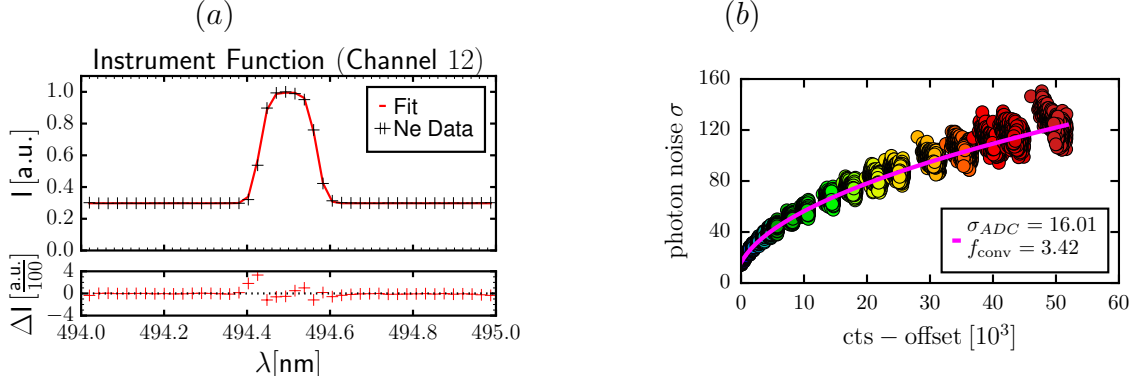


Figure 4.7: (a): The instrument function of channel 12 of the COR spectrometer can be described by the convolution of a box function and a Gaussian. A relative deviation between the fit (red line) and the experimental data (black crosses) is shown in the bottom row. (b): Measured photon noise as a function of measured counts. The data agrees with a conversion factor from counts to photons of 3.42 (represented by the pink line) for a controller gain of 3.

uncertainty in the intensity calibration is on the order of 10–15%, which is included in the calculation of n_{imp} .

Instrument function

The plasma temperature is given by the Doppler broadening of the spectral line, i.e. the width of the measured line. The measured spectral line shape, however, is the convolution of the Doppler broadening and the instrument function of the spectrometer. The instrument function can be measured in the laboratory using a low temperature calibration lamp (Ne and Hg lamps). At low temperatures, the line shape is determined by the instrument function of the spectrometer such that the measured line shape is to a good approximation the instrument function.

Figure 4.7a shows the measured instrument function for one channel of the COR spectrometer. In order to have as much signal as possible on the HFS, a rather large slit width of 100 μm has been chosen. The resulting instrument function is then given by the convolution of the box shaped slit and a Gaussian function.

Photon noise

The variation in the counts of the CCD camera while observing a temporally and spatially constant light source has two contributions: the photon noise and a noise introduced by the analog-to-digital conversion (ADC) of the incoming photons to a digital count signal. The photon noise can be described by a Poisson distribution $\sigma_{ph} = \sqrt{n_{ph}} = \sqrt{f_{conv} n_{counts}}$, where n_{counts} is the number of detected counts and f_{conv} the conversion factor from the detected photons to counts. This leads to the total count noise of [138]:

$$\sigma = \sqrt{\sigma_{\text{ADC}}^2 + f_{\text{conv}} n_{\text{counts}}}. \quad (4.7)$$

The conversion factor can be determined by measuring the standard deviation of the measured counts (photon noise), while gradually increasing the strength of the light source as shown in figure 4.7b. The increased light strength leads to an increase in the count rate, which is associated with an increased photon noise. This behavior can be described with a square root function.

Wavelength calibration

For an accurate measurement of the plasma rotation, a precise wavelength calibration is needed. During plasma discharges, there is, however, only one channel of the spectrometer not connected to the in-vessel optical heads that can be used to determine the wavelengths of the different pixels on the CCD chip. This section will derive an equation to connect the wavelength axis of this one channel to the other channels of the spectrometer.

The wavelength axis of the spectrometer is determined by the grating equation for a Czerny-Turner spectrometer:

$$n g \lambda = \cos \gamma (\sin(\theta_1 + \phi_1) + \sin(\theta_2 + \phi_2)), \quad (4.8)$$

where n is the diffraction order, g is the number of grooves/mm of the grating, λ is the wavelength, γ is the vertical angle of an off-axis ray, θ_1 and θ_2 are the incident and the diffraction angles, and ϕ_1 and ϕ_2 are the horizontal angle of the entrance slit and of the image plane, respectively (see figure 4.4). The horizontal distances x_1 and x_2 from the optical axis on the slit plane and the image plane can be defined as $\tan \phi_1 = x_1/f_1$ and $\tan \phi_2 = x_2/f_2$, respectively. On the optical axis ($\gamma = 0$, $\phi_1 = 0$, $\phi_2 = 0$), the central wavelength λ_0 is given by the grating and observation geometry:

$$\lambda_0 = \frac{\sin \theta_1 + \sin \theta_2}{n g}. \quad (4.9)$$

The dispersion of the image plane for a fixed central wavelength can be calculated by differentiating equation (4.8) with respect to x_2 ([139], appendix A):

$$\frac{\partial \lambda}{\partial x_2} = \left(\frac{\lambda_0}{f_2} \right) \frac{\cos \gamma \cos(\theta_2 + \phi_2) \cos^2 \phi_2}{\sin \theta_1 + \sin \theta_2}. \quad (4.10)$$

Figure 4.8a shows the dependence of the same wavelength on the distance from the axis. The parabolic shape is related to the dependence of λ on γ and can be deduced from equation (4.8) by a Taylor expansion up to second order assuming small angles, i.e. $\gamma \ll 1$ and $x_2 \ll f_2$ (see appendix A):

$$x_2 = \frac{\sin \theta_1 + \sin \theta_2}{2 f_2 \cos \theta_2} y_2^2. \quad (4.11)$$

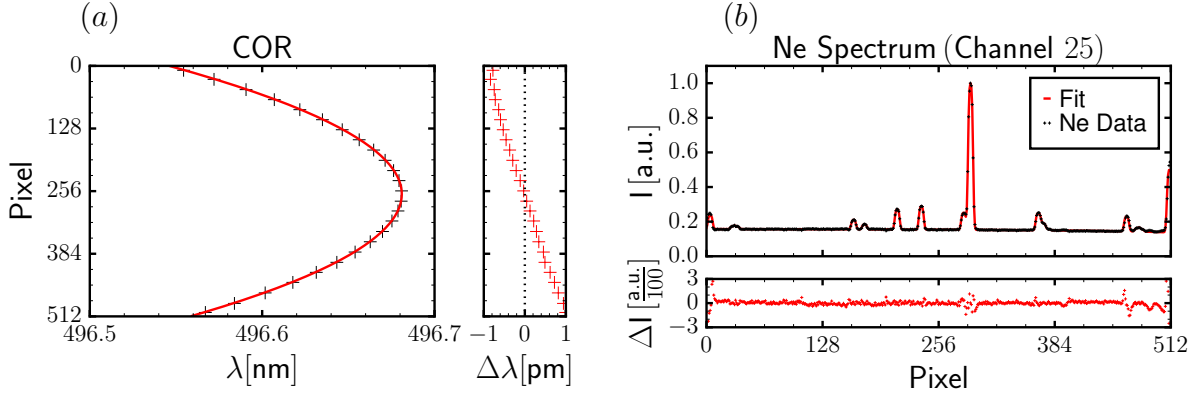


Figure 4.8: (a): Measured central wavelength of the different channels (black crosses) on the CCD as a function of the vertical position on the chip. A parabolic fit to the data is shown in red. The parabola fits within deviations of less than 1 pm. (b): Measured Ne spectrum in the calibration channel after the plasma discharge. By knowing the central wavelength of one channel, the other channels can be calculated by knowing the calibration parabola (see figure on the left side).

This equation shows that the different channels of the spectrometer are connected to each other through the wavelength parabola of the spectrometer. Knowing the wavelength axis of one channel, those for the other channels can be calculated according to the measured parabola. The wavelength calibration after the plasma discharge is done with a narrow-band light source (e.g. a Ne pen-ray lamp) for one channel after each plasma discharge (see figure 4.8b).

The indirect measurement of the poloidal rotation relies on an accurate measurement of the toroidal rotation and, hence, a very precise knowledge of the wavelength calibration is necessary. An error estimate of the wavelength calibration is given by fitting the whole spectrum at once and comparing this to the positions of the single Ne lines. This comparison reveals an error in the fitting of 1 pm, i.e. an error in the wavelength calibration of roughly of 1 km/s.

4.4 Corrections to CXRS measurements

Effects due to atomic physics may affect the measured spectra and can introduce errors in the temperature and rotation measurements if they are not properly taken into account. This section will discuss briefly the energy dependence of the CX cross-sections as well as the Zeeman and Stark effects and how important they are for the CXRS measurements.

4.4.1 Energy dependence of CX cross-sections

Figure 4.9 shows the effective rate coefficient for the most relevant low- Z impurities for the CX reaction from the ground state ($n = 1$) and the first excited state ($n = 2$) of the

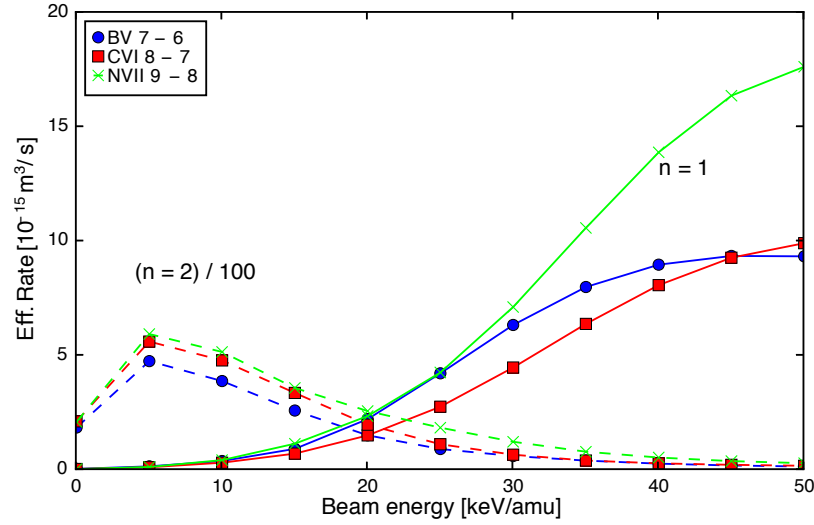


Figure 4.9: Effective CX rate coefficients as a function of beam energy for the impurities B, C and N. Besides the contribution from the $n = 1$ state, the rate coefficients for the excited neutrals ($n = 2$) are shown as well with dashed lines.

beam neutral. The rate coefficient for the $n = 2$ CX reaction is divided by 100 in order to show it on the same scale as the $n = 1$ contribution. Due to the small population of the $n = 2$ state, the contribution to the total emission from this population tends to be small despite the size of the rate. From the figure, one can see that the CX cross-sections are dependent on the beam energy and that larger beam energies lead to an increased signal (up to the maximum of 50 keV/amu). The beam boxes at AUG have the same input power but a different injection energy. The beam box 1 injects the neutrals with 60 keV and box 2 with 93 keV. The increase in signal (due to the higher injection energy) is, therefore, compensated by the injection of less particles from box 2. These two effects balance each other out such that the CXRS systems from box 1 and box 2 see similar radiances ([42] and figure 4.12e). The benefit of using NBI sources from box 2 for CXRS is the deeper penetration of the beam neutrals so that it is possible to have CXRS measurements on the HFS as well.

The main atomic physics effects resulting from the energy dependence of the CX cross-sections are an apparent wavelength shift (apparent velocity) and a reduction in the line width (apparent temperature) [140]. This results from the fact that the injected NBI neutrals collide with the ions gyrating around magnetic field lines. The ions are moving towards/away from the neutral particles at different points in their orbits and have, therefore, a slightly higher/lower collision velocity resulting in a higher/lower probability to undergo a CX reaction (see figure 4.9). This can distort the measured spectra by increasing/decreasing the observed line intensity on one side of the spectrum. Thus, the change in the line width and the line shift are not representative of the true temperature and rotation.

The corrections to the rotation measurements are dependent on the beam velocity, the viewing geometry of the LOS, and on the bulk plasma rotation [140]. For the

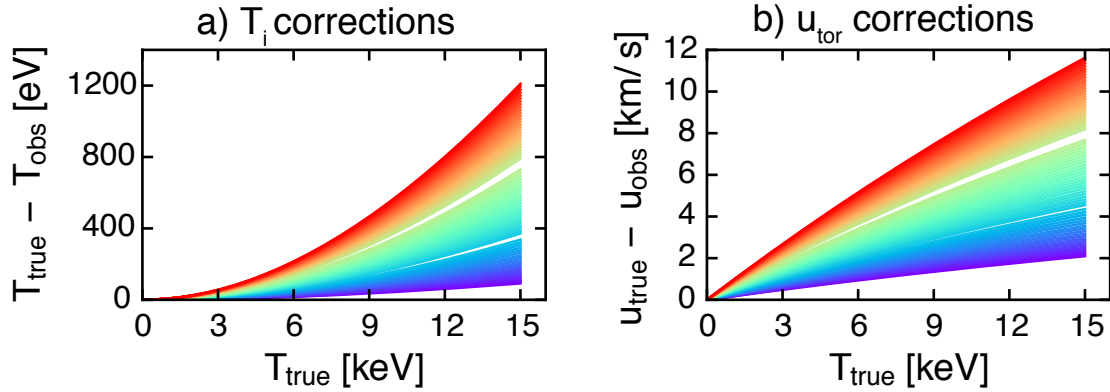


Figure 4.10: Temperature (a) and toroidal rotation (b) corrections to the CXRS measurements associated with the energy dependence of the cross-sections and the viewing geometry as a function of the true plasma temperature. The color coding shows the LOS of the COR head from 'COR-01' (LFS) in blue to 'COR-70' in red HFS). The analytical expressions given in [140] have been used to calculate the corrections and $u_{\text{tor}} = 100$ km/s has been assumed.

viewing geometry of the COR LOS, the corrections to u_{tor} are on the order of roughly 1–5 % (see figure 4.10b) and could, therefore, affect the indirect reconstruction of u_{pol} (see section 4.6.2). While the effects of the viewing geometry cancel out for a toroidal system, a net effect will remain for a poloidal CXRS due to the gyro-motion of the particles. This will be discussed in the next section.

Figure 4.10a shows the temperature corrections for the LOS of the COR optical head. It can be seen that the temperatures on the HFS are in general larger than on the LFS creating an asymmetry in the observed temperatures (but not the true ones!). This effect is, however, in general smaller than 2 % (for typical AUG temperatures of $T_i < 5$ keV) and is as well routinely corrected through the usage of look up tables.

4.4.2 Gyro-motion effect

For core poloidal rotation measurements the energy dependency of the CX cross-sections has a significant impact and can actually exceed the true u_{pol} values in the plasma core by one order of magnitude [141]. The so-called gyro-motion effect (see figure 4.11a) results from the fact that ions gyrating towards the NBI source have a larger probability for the CX reaction than those gyrating away from it (similarly to the previous section). This fact is illustrated by the different sizes of the arrows in figure 4.11a. After a certain lifetime τ of the excited state, during which the ion precesses along its gyro-orbit by the distance $\omega \tau$, a photon is released with the associated Doppler shifted frequency concomitant with the de-excitation. The asymmetry in the CX probability creates, then, a line shift depending on the lifetime of the excited state [28].

In figure 4.11b, the gyro-motion is calculated for typical plasma core and edge parameters. A poloidal LOS that is viewing in the z direction has been assumed for these

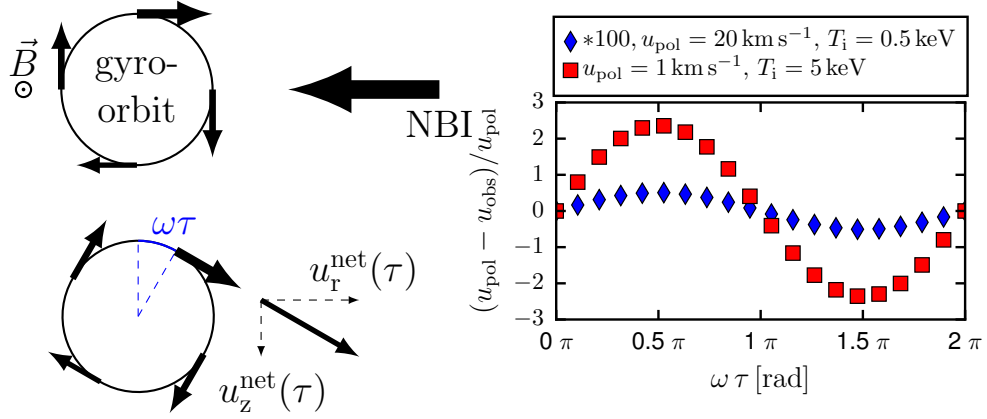


Figure 4.11: (a): Illustration of gyro-motion effect: The ions gyrating towards the neutral particle have a higher probability for a CX reaction than those gyrating away (indicated by arrow sizes). The precession of the ion along its gyro-orbit, during the lifetime τ of the excited state, leads to a net (apparent) rotation velocity pointing in the poloidal direction (downwards). (b): Comparison of the relative gyro-motion effect for typical plasma core (red squares) and edge parameters (blue diamonds). The effect for the plasma edge is multiplied by a factor of 100. The gyro-motion effect can be neglected for the plasma edge ($< 0.5\%$), while the maximal deviation for the plasma core is larger than the true value by a factor of 2.

calculations. It can be seen that the relative gyro-motion effect, i.e. the apparent shift related to the true u_{pol} , is dependent on $\omega\tau$: it is zero for $\omega\tau = k \cdot \pi, k \in \mathbb{N}$ and maximal for $\omega\tau = (k + 0.5) \cdot \pi$. The physics behind this dependency is rather intuitive: The gyro-orbit plane can be divided horizontally and ions that are in the upper part have a higher probability for a CX reaction than those in the lower part (up-down asymmetry). There is, however, no asymmetry in the z direction (measurement direction) for $\omega\tau = \pi, 2\pi, 3\pi, \dots$. This can be seen by dividing the gyro-orbit plane vertically. There are always two velocity vectors with the same collision velocity (located at the same z position on the left and right side of the gyro-orbit plane) whose projection into the z direction have the same value but different directions, i.e. there is no asymmetry between left and right. The asymmetry between left and right side of the gyro-orbit plane generates, however, the apparent rotation. The up-down asymmetry is fully transformed into a left-right asymmetry for the case that $\omega\tau = \pi/2, 3\pi/2, 5\pi/2, \dots$ giving the maximal effect of the gyro-motion on the measurement.

It can be seen additionally from figure 4.11b that the relative gyro-motion effect is rather small for the plasma edge ($< 0.5\%$). For the plasma core, however, the maximal effect is more than twice as large as the true rotation. The fact that the lifetime of the excited state is not known perfectly creates a rather large uncertainty on the true value of the poloidal rotation. This effect is, therefore, limiting the accuracy of direct measurements of the poloidal rotation in the plasma core.

4.4.3 Corrections due to Zeeman splitting and fine structure

In the presence of a magnetic field, spectral lines are split into several components which are energy shifted around the rest wavelength (Zeeman effect [142, 143]). Each of these lines has a Gaussian distribution with a Doppler width representing the true ion temperature. All of these components result in a total line shape that is Gaussian as well but with a wider line shape than given by the true ion temperature. The Zeeman effect leads, if not properly taken into account, to an overestimation of T_i [129, 144]. An estimate for the symmetrical wavelength displacement is given by [145]:

$$\Delta \lambda_{\text{Zeeman}} = 4.7 \times 10^{-9} \lambda_0^2 B [\text{T}] \quad (4.12)$$

where $\Delta \lambda_{\text{Zeeman}}$ and λ_0 are expressed in Å. For standard AUG parameters, i.e. $B_{\text{HFS}} = 3.5 \text{ T}$ and $B_{\text{LFS}} = 2 \text{ T}$, and for B V ($n = 7 \rightarrow 6$) one obtains a splitting from the Zeeman effect of $\Delta \lambda_{\text{Zeeman, HFS}} = 0.46 \text{ Å}$ and $\Delta \lambda_{\text{Zeeman, LFS}} = 0.26 \text{ Å}$. At AUG, the Zeeman effect is corrected automatically by calculating the local magnetic field and the angle between the LOS and \vec{B} .

Similarly to the Zeeman effect in a magnetic field, the Stark effect leads to a splitting of the spectral lines in an electric field and, hence, to a wider line shape. The electric field is present due to the motion of the ion in the magnetic field. In its rest-frame it experiences the electric field $\vec{E} = \vec{u} \times \vec{B}$ and, therefore, the spectral line shape is broader. The splitting of the spectral line due to the motion in a magnetic field is also known as motional Stark effect. An analytical expression to evaluate the related splitting of the spectral line is given in [129]. For relevant plasma conditions in the core of AUG (in a magnetic field of 2.6 T and ion temperatures of 5 keV), the maximal broadening of the B V ($n = 7 \rightarrow 6$) line is lower than 0.12 Å. For comparison, the thermal Doppler broadening for $T_i = 100 \text{ eV}$ is given by $\Delta \lambda_{\text{Doppler}} = 1.4 \text{ Å}$. The cumulative effect of thermal Doppler, Zeeman and Stark broadening can be approximated as:

$$\Delta \lambda = \sqrt{\Delta \lambda_{\text{Doppler}}^2 + \Delta \lambda_{\text{Zeeman}}^2 + \Delta \lambda_{\text{Stark}}^2}. \quad (4.13)$$

For the pedestal top at the LFS the cumulative effect is 5% and for the HFS 10%. Especially, the Zeeman effect at the pedestal top on the HFS (with magnetic fields of 3.5 T) can have a significant impact.

4.5 Validation of CXRS measurements

The measurements of different CXRS diagnostics can be combined giving full radial profiles, i.e. from the separatrix on the LFS to the separatrix on the HFS. A comparison between all CXRS measurements provides a consistency check of the different diagnostics. Figure 4.12 shows a comparison of the CXRS quantities (T_i , u_{tor} , and n_{imp}) for the different diagnostics presented in section 4.2. In this discharge, all CXRS systems were measuring the B⁵⁺ spectral line. Figures 4.12a, c, and e show that the profiles of the different diagnostics align very well when plotted against the major radius.

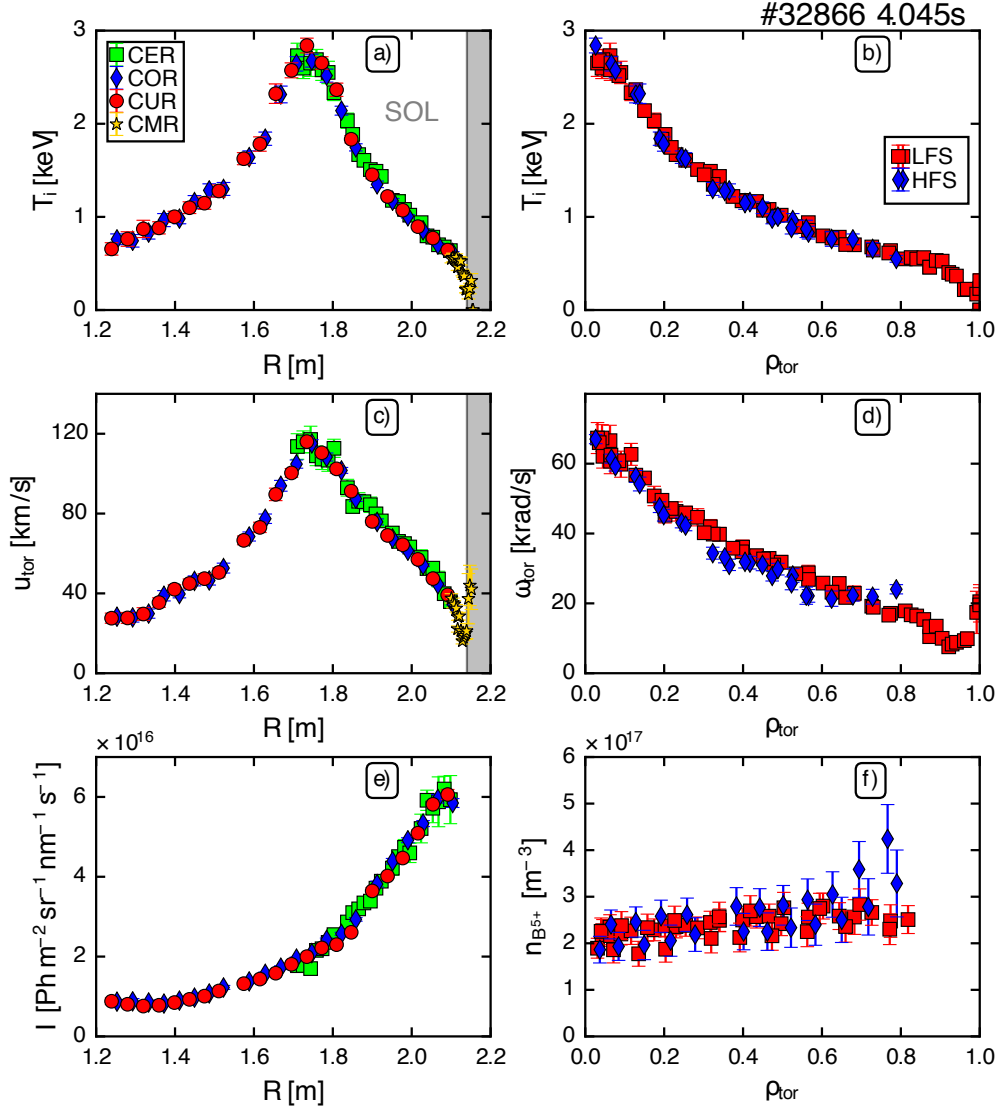


Figure 4.12: Comparison of radial profiles (as a function of R and ρ_{pol}) for: (a) & (b) ion temperature, (c) toroidal rotation velocity, (d) toroidal rotation frequency $\omega_{\text{tor}} = u_{\text{tor}}/R$, (e) intensity of the active BV ($7 \rightarrow 6$) CX line and (f) corresponding impurity density profile. The color coding in the plots (a), (c), and (e) shows the measurements of different CXRS spectrometers (CER: green, COR: blue, CUR: red, CMR: yellow) and the the plots (b), (d), and (f) a separation between LFS (red squares) and HFS (blue diamonds).

Figures 4.12b, d, and f show the comparison between the profiles on the LFS (red squares) and HFS (blue diamonds) as a function of the normalized toroidal flux coordinate ρ_{tor} . The ion temperatures align very well between LFS and HFS showing that the ion temperature is a flux surface constant. Figure 4.12d shows the toroidal rotation frequency $\omega_{\text{tor}} = u_{\text{tor}}/R$ as a function of the normalized toroidal flux coordinate. In general,

ω_{tor} does not have to be a flux function, since this implies that there is no poloidal flow (see section 3.3). For the data presented here, there is a small deviation between LFS and HFS giving a poloidal flow (see following section and figure 4.13). Figure 4.12f shows that the reconstructed impurity density profile for B^{5+} agrees within the uncertainties between the different diagnostics inside of $\rho_{\text{tor}} = 0.8$. The asymmetry between LFS and HFS starting at $\rho_{\text{tor}} = 0.8$ is discussed in chapter 6.

4.6 Measurement of the core poloidal rotation

For the plasma edge, the direct measurement of u_{pol} with CXRS is a standard technique. In the plasma core, however, the direct measurement is associated with large corrections that can easily exceed the true poloidal rotation. This section will give a short overview of the difficulties associated with the direct measurement of u_{pol} in the plasma core and, subsequently, introduce the indirect technique enabling measurements of u_{pol} with an accuracy of 1 km/s or better.

4.6.1 Challenges associated with the direct measurement of u_{pol}

There are two main effects complicating the direct measurement of the poloidal rotation in the plasma core:

1. The apparent velocity introduced by the gyro-motion effect can exceed the true poloidal rotation velocity up to one order of magnitude (see section 4.4.2) such that corrections larger than the actual value are necessary. Additionally, the lifetime of the excited state is only known to a certain accuracy creating uncertainties on the correction factor that are at least on the order of the measured value.
2. For the plasma core, neoclassical theory predicts small poloidal rotations (1 to 2 km s^{-1}) (see section 3.4). These values are in the same range as typical uncertainties created by the calibration of the CXRS systems (see section 4.3).

Therefore, a more accurate method is needed with error bars smaller than the expected velocities in order to address the question of the nature of the poloidal rotation. A promising technique to deduce the core poloidal rotation with a high accuracy is the indirect measurement technique introduced next.

4.6.2 Indirect measurement of u_{pol}

The indirect measurement technique was established first at the PDX tokamak in 1982 [38] and was established recently at DIII-D [39] and TCV [40], as well. The basic principle for this technique, which is the equation of the general plasma flow, has been introduced in section 3.3. Equation (3.27) states that any plasma flow can be expressed as the sum of a rigid body rotation and a component parallel to the magnetic field: $\vec{u} = \hat{\omega} \vec{e}_{\text{tor}} + \hat{u} \vec{B}$. Measuring u_{tor} at two distinct points on the same flux surface enables the reconstruction of the two flux functions $\hat{\omega}$ and \hat{u} and, therefore, the indirect measurement of u_{pol} . In

the following first results of the u_{pol} reconstruction for the case without impurity density asymmetries will be shown.

Without impurity density asymmetries

In order to relate the locally measured u_{tor} values to the flux functions and finally to u_{pol} it is important to have the correct signs and to take the magnetic field structure and local coordinate system into account. Therefore, the tokamak coordinate convention scheme (COCOS) proposed in [146] will be used for the sign conventions. Within this scheme, the magnetic field is defined as in equation (3.22); implying for the standard AUG parameter the following: $s_b = -1$ and $s_j = -1$ (COCOS index 3).

Explicit equations for the flux functions \hat{u} and $\hat{\omega}$ can be derived by evaluating equation (3.30) at the HFS and LFS mid-plane:

$$\hat{u}(\psi) = s_b F^{-1} \left(\frac{u_{\text{tor,HFS}}/R_{\text{HFS}} - u_{\text{tor,LFS}}/R_{\text{LFS}}}{R_{\text{HFS}}^{-2} - R_{\text{LFS}}^{-2}} \right), \quad (4.14)$$

$$\hat{\omega}(\psi) = \frac{u_{\text{tor,HFS}} R_{\text{HFS}} - u_{\text{tor,LFS}} R_{\text{LFS}}}{R_{\text{HFS}}^2 - R_{\text{LFS}}^2}. \quad (4.15)$$

Putting equation (3.30) into the radial force balance introduced in equation (3.6) shows that the radial electric field and, hence, $\vec{u}_{\vec{E} \times \vec{B}}$ of the plasma can be measured with toroidal LOS only³:

$$E_r = \frac{\nabla p_\alpha}{e Z_\alpha n_\alpha} + u_{\perp,\alpha} = \frac{\nabla p_\alpha}{e Z_\alpha n_\alpha} + s_j \hat{\omega}(\psi) R B_{\text{pol}} \quad (4.16)$$

Compared to the direct measurement the indirect measurement of u_{pol} has a number of advantages. The largest advantage is that it is not sensitive to the gyro-motion effect introduced in section 4.6.1 because the LOS are rather parallel to the magnetic field and see only little perpendicular motion of the particles. Furthermore, the asymmetry between LFS and HFS toroidal rotation frequency is amplified with the safety factor: $\Delta\omega_{\text{tor}} \approx 4q u_{\text{pol}}/R_0$ (see appendix B) which enables an accurate measurement of u_{pol} for plasma discharges with large q values, i.e. with small plasma current. Lastly, systematic errors are reduced by comparing u_{tor} on the HFS and the LFS measured on a single spectrometer.

Figure 4.13 shows the indirect measurement of u_{pol} for the discharge #32866 at 4.045s. The light crosses in figure 4.13a shows the data used for the Monte Carlo error calculation (see below) and the solid lines are the best fits to the experimental data. A small asymmetry on the order of 2 to 4 krad/s is visible in the data (see figure 4.13b) leading to a non-zero \hat{u} component (see figure 4.13c) and, thus, a poloidal flow is reconstructed (see figure 4.13d).

³Here the following expression of the perpendicular velocity has been used: $u_{\perp} = \hat{\omega} R \frac{B_{\text{pol}}}{B}$

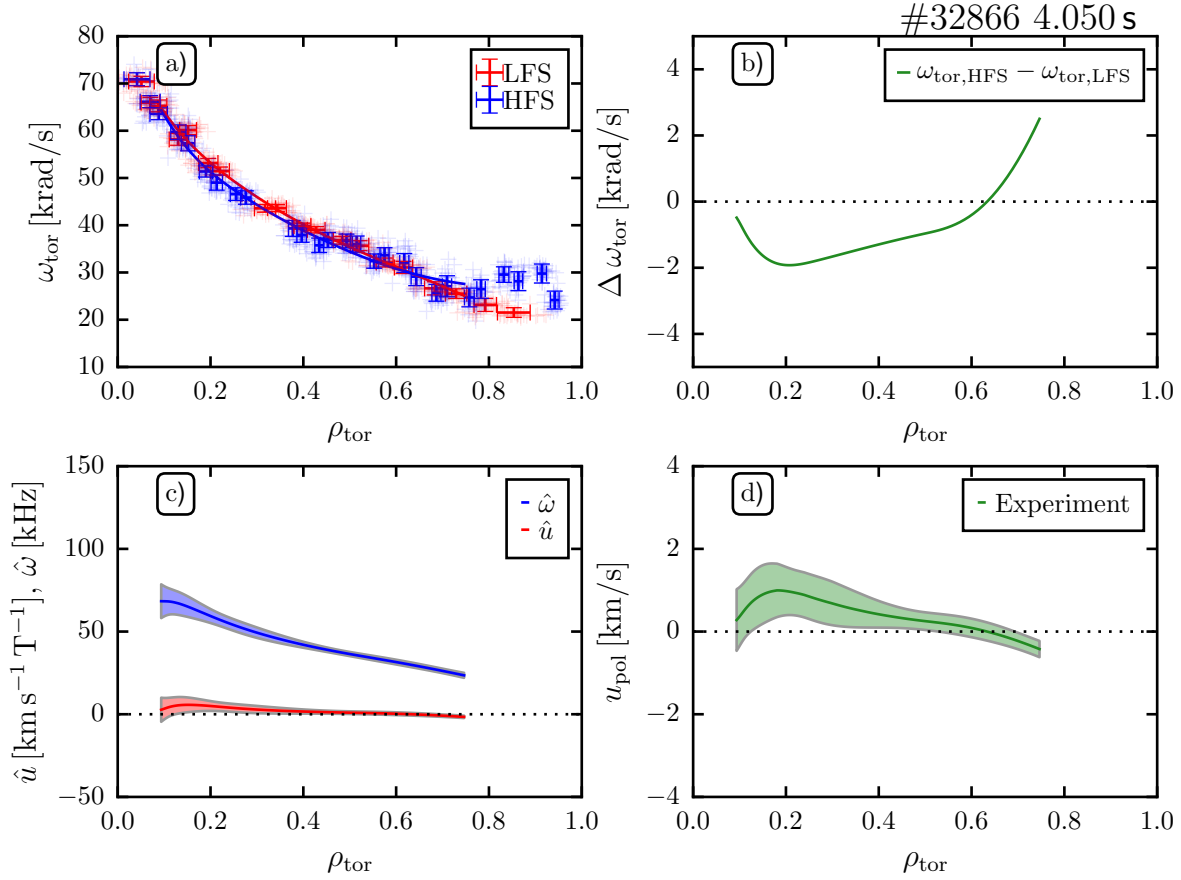


Figure 4.13: Indirect measurement of u_{pol} . (a) shows the measured ω_{tor} and its corresponding uncertainties on LFS and HFS. The small crosses indicate the data used for the Monte Carlo error estimation. (b) illustrates that there is an asymmetry in ω_{tor} leading to a poloidal rotation in the ion diamagnetic direction for $\rho_{\text{tor}} < 0.6$ (d). (c) shows the flux functions $\hat{\omega}$ and \hat{u} with corresponding uncertainties.

Error calculation

Error propagation is in general very complex for derived quantities even though all experimental uncertainties are, in principle, known. Especially for the case that the derived quantity is dependent on the gradients resulting from fitting procedures or when the quantity is the result of a complex numerical computation, the error propagation is very tough to implement (if possible). For the indirect measurement of u_{pol} , one challenging part is, for example, the mapping from the major radius to the normalized flux coordinate. This step is essential to deduce asymmetries in ω_{tor} . The errors on the flux surface positions can only be calculated with additional computational effort. Another example is that the neoclassical calculation of u_{pol} depends on the gradients of the input profiles. An error propagation would only be feasible by adding a corresponding error treatment to the neoclassical codes. In such cases, a more practical solution is a Monte Carlo approach.

In general, the error calculation from a Monte Carlo code is based on the calculation of the mean value and the standard deviation of the quantity of interest. The indirect measurement, however, yields in principle only one measurement. Therefore, a set of virtual measurements is created randomly by varying the measured data with a normal distribution within their uncertainties. For a toroidal rotation measurement this means, for example, that the set of virtual measurements is created by using the uncertainties of the measurement position (in r and z), the spot-size, and the error on the velocity itself. The results are shown by the light crosses in figure 4.13a. Subsequently, the flux functions and the corresponding u_{pol} value is calculated for each virtual measurement giving as well an estimate for the error of u_{pol} (see error bands in figure 4.13d).

Chapter 5

Validation of the indirect measurement technique

The previous chapter showed that the indirect measurement technique of the poloidal rotation in the plasma core is less prone to systematic errors compared to the direct measurement and enables thus the determination of the direction of the poloidal flow. This chapter aims at validating the measurement technique, outlining possible limitations, and estimating the effects of uncertainties in the magnetic equilibrium on the u_{pol} reconstruction.

5.1 Artificial data

In order to test the accuracy of the u_{pol} reconstruction, artificial datasets using realistic profiles for \hat{u} and $\hat{\omega}$ from equation (4.14) and (4.15) were used to test the quality of the reconstruction. Together with the magnetic field which is taken from the discharge #30722 at 1.9s, the toroidal rotation values for the different channels of the COR optical head can be calculated, which are subsequently used as input profiles for the u_{pol} reconstruction. The profiles of the flux functions \hat{u} and $\hat{\omega}$ are calculated by fitting a spline function through a number of radially distributed points (see black dots in figure 5.1c and d). The thereby created profiles for the flux functions \hat{u} and $\hat{\omega}$ are shown with solid black lines in the figures 5.1c and d. The previous chapter demonstrated that the poloidal rotation is given by B_{pol} times \hat{u} , so that the u_{pol} profile in panel (b) is calculated from the poloidal magnetic field profile shown in figure 5.1a and \hat{u} . In order to reconstruct u_{pol} , the artificial toroidal rotation values are required for the 70 LOSs of the COR optical head. With the knowledge of the magnetic field and the geometry of the LOS in the torus, these values can be calculated by projecting the total plasma flow given by \hat{u} and $\hat{\omega}$ into the LOSs direction. The quantities for the 70 LOSs are shown in panel e for the HFS channels in blue and the LFS channels in red. The solid green lines in panels b, c, and d illustrate the reconstructed profiles for u_{pol} , \hat{u} , and $\hat{\omega}$. It can be seen that the implemented reconstruction algorithm reproduces the profiles very well.

In order to add error bars to the reconstructed values, the typical error bars of the u_{tor} measurement are added to the values in figure 5.1 as noise and the radial resolution of the

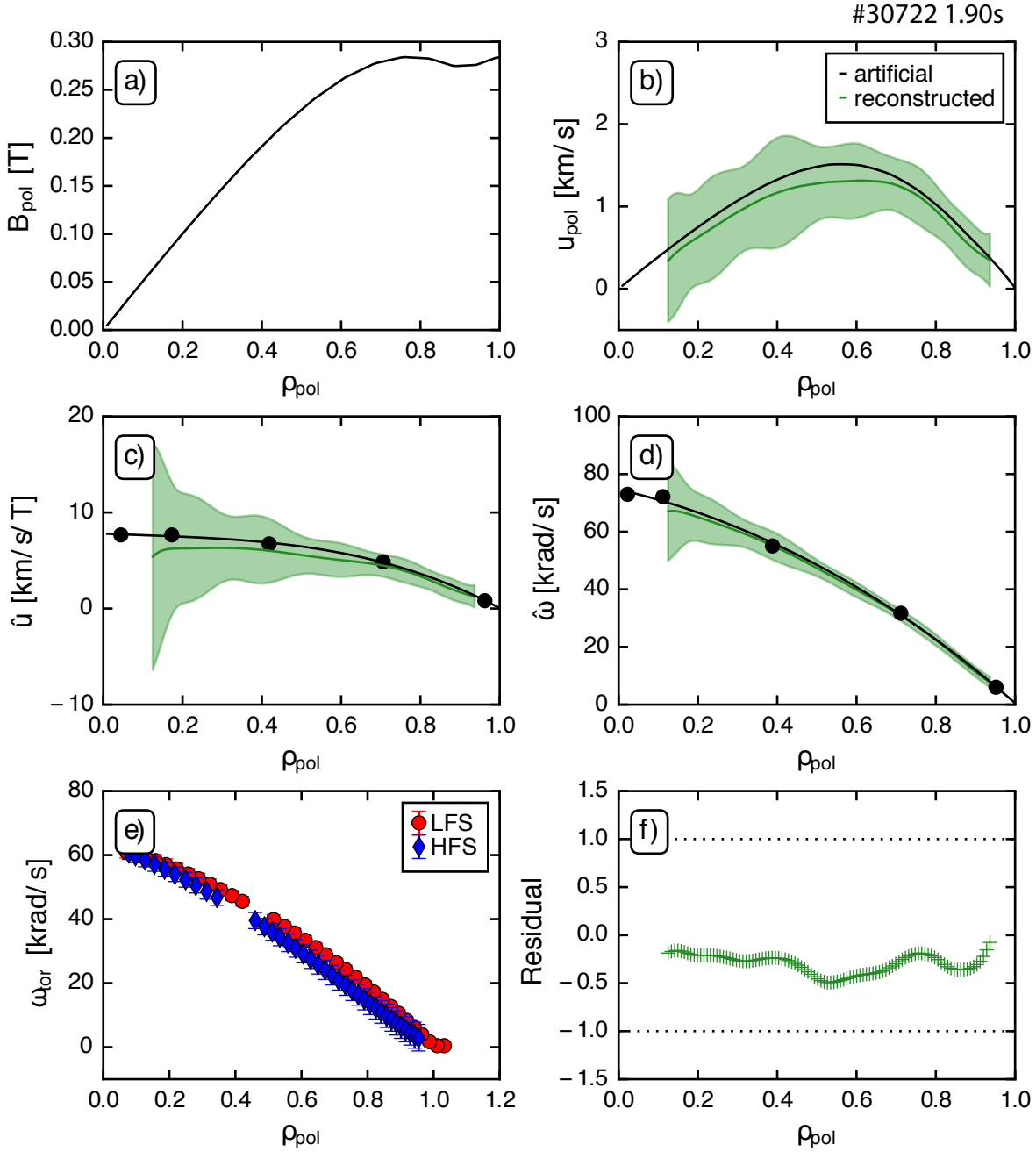


Figure 5.1: Reconstruction of the poloidal rotation profile with artificial data. (b) an artificial u_{pol} profile (black line) has been generated using (a) the standard B_{pol} profile from EQH and a (c) \hat{u} profile constructed with a spline (black line) through a number of points (black dots). Together with a $\hat{\omega}$ profile (d), the full plasma flow is given and the measured quantities for the 70 LOSs can be calculated via the projection into the LOS (e, the LFS points are shown in red dots and the HFS in blue diamonds). From these artificial measurements, the poloidal rotation (b) as well as the \hat{u} (c) and $\hat{\omega}$ (d) profiles can be reconstructed (green line with error bands). Figure (f) shows the residual of the u_{pol} reconstruction.

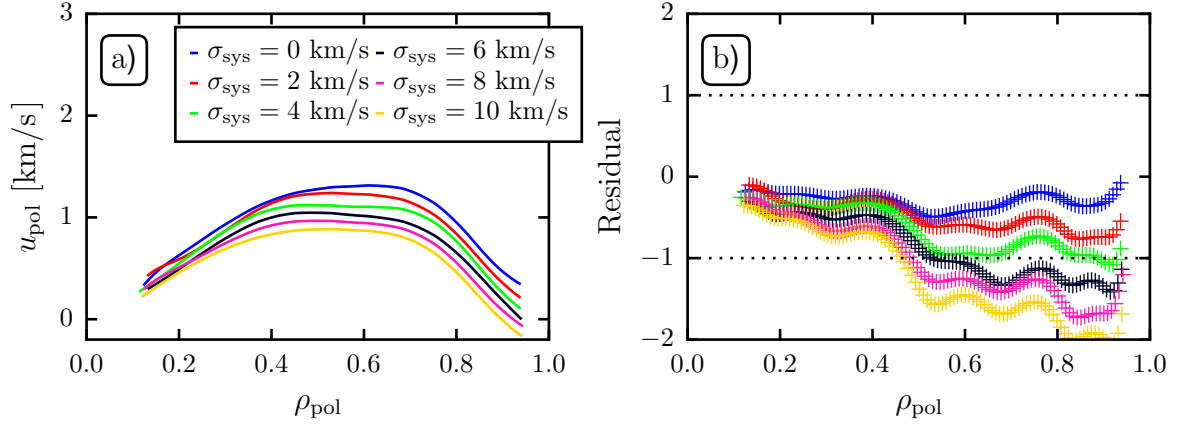


Figure 5.2: Effects of systematic errors on the u_{pol} reconstruction. Different systematic errors (0 to 10 km/s) are added to the artificially generated quantities from figure 5.1e. Figure (a) shows the resulting u_{pol} profiles for the different systematic errors and (b) the corresponding residual of the reconstruction.

different LOS (shown in figure 4.5) is as well taken into account for the error estimation. The calculation of the error on the profiles is the same as outlined in section 4.6.2, i.e. a set of generic u_{tor} profiles is generated by varying the toroidal rotation value and the radial resolution of each channel within their uncertainties. For each of these generic profiles, the poloidal rotation is reconstructed such that the error on the profiles is given by the standard deviation of the u_{pol} profiles from the mean value. Due to the radial coverage of the 70 LOSs, there is a small jump in z between the optical heads OH1/OH2 and OH2/OH3, respectively. This jump gets important for the u_{pol} reconstruction when the profiles are fitted as a function of the minor radius r . The fitted u_{pol} profiles feature unphysical jumps / spin-ups at around mid-radius. Mapping the kinetic profiles to the magnetic equilibrium first, the jump in z has only a small to little effect on the u_{pol} reconstruction as it is shown by the smaller values of u_{pol} in figure 5.1b at roughly $\rho_{\text{pol}} = 0.5$. The other parts of the u_{pol} profiles, i.e. $\rho_{\text{pol}} < 0.4$ and $\rho_{\text{pol}} > 0.6$, are well reproduced with the artificial data, i.e. the residual of the reconstruction (see figure 5.1f) is smaller than 0.5 for the typical measurement uncertainties of the diagnostic.

The reconstruction with artificial data enables as well to test effects of systematic errors (e.g. errors in the absolute wavelength calibration, figure 5.2). Different values of systematic errors in a range from 0 to 10 km/s are added to the artificial quantities (figure 5.1e). From figure 5.2b it can be seen that there are two regions with different effects of systematic errors on the u_{pol} reconstruction. An increase in the systematic error leads to only small deviations between the true and reconstructed u_{pol} profiles for $\rho_{\text{pol}} < 0.4$. For $\rho_{\text{pol}} > 0.4$, however, an increase in the systematic error has a larger impact and leads to a stronger reduction of the inferred poloidal rotation. This results from the measurement principle: u_{pol} is proportional to the difference in the rotation frequency on LFS and HFS. Additional systematic errors affect all channels simultaneously and lead to an offset when the measured quantities are divided by major radius R of the

measurement location:

$$u_{\text{pol}}^* \propto \Delta \omega_{\text{tor}}^* = \frac{u_{\text{tor,HFS}} + u_{\text{sys}}}{R_{\text{HFS}}} - \frac{u_{\text{tor,LFS}} + u_{\text{sys}}}{R_{\text{LFS}}} \quad (5.1)$$

$$= \Delta \omega_{\text{tor}} + u_{\text{sys}} \left(\frac{1}{R_{\text{HFS}}} - \frac{1}{R_{\text{LFS}}} \right) \quad (5.2)$$

This offset depends on the distance between the HFS and LFS measurement positions and is, therefore, smallest in the plasma center and largest at the pedestal top. The main systematic error source in the system is the wavelength calibration. With the usage of the Ne calibration lamp after each shot, the uncertainties were measured to be less than 2 km/s leading to a maximal systematic error of the u_{pol} reconstruction of 100 m/s for the profiles shown here.

5.2 Effects of uncertainties in the magnetic equilibrium

The indirect measurement technique is based on the evaluation of the toroidal flow at two distinct point on the same flux surface, i.e. at the same normalized flux coordinate $(\rho_{\text{tor}}, \rho_{\text{pol}})$ on the LFS and the HFS. CXRS measures, however, in real space coordinates (R, z, ϕ) so that a mapping to the magnetic equilibrium during the reconstruction process is necessary.

The standard magnetic equilibria (EQI and EQH) at AUG are calculated using solely the measurements of the different magnetic pickup coils. Additionally, advanced magnetic equilibrium reconstructions can be performed that take additional information such as the fast ion pressure, thermal pressure, isotherm constraints, and q -profile measurements into account (see section 2.4). These equilibria are not routinely available and were not calculated for the bulk of the plasma discharges utilized in this thesis.

As will be shown in this section, the standard magnetic equilibrium is not sufficiently accurate for some plasma discharges, leading to non-physically large poloidal rotation values and, therefore, an alternative method is needed to detect possible inconsistencies of the magnetic equilibrium and correct the input profiles for the u_{pol} reconstruction properly. Fortunately, this can be done to high accuracy by assuming that T_i is constant on flux surfaces. Due to efficient parallel transport along magnetic field lines, it is expected that in addition to the plasma pressure, the temperature of a given species is also constant on flux surfaces. If the LFS and the HFS profiles do not overlay this can then be interpreted as an error in the magnetic equilibrium and in this case, a shift is applied to the HFS points to bring them into agreement with the LFS ion temperature profiles.

The procedure of the magnetic equilibrium corrections is similar to what was done in [147] and is illustrated in figure 5.3 for the discharge #32866 at 7.5 s. By taking a close look at the ion temperature profiles shown in figure 5.3a one can see that there is a slight asymmetry between the T_i profiles on the LFS and the HFS in the plasma core ($\rho_{\text{tor}} < 0.3$) which could be related to not accurate reconstructions of the magnetic axis. In order to correct this misalignment, the HFS profiles (black squares) have been shifted

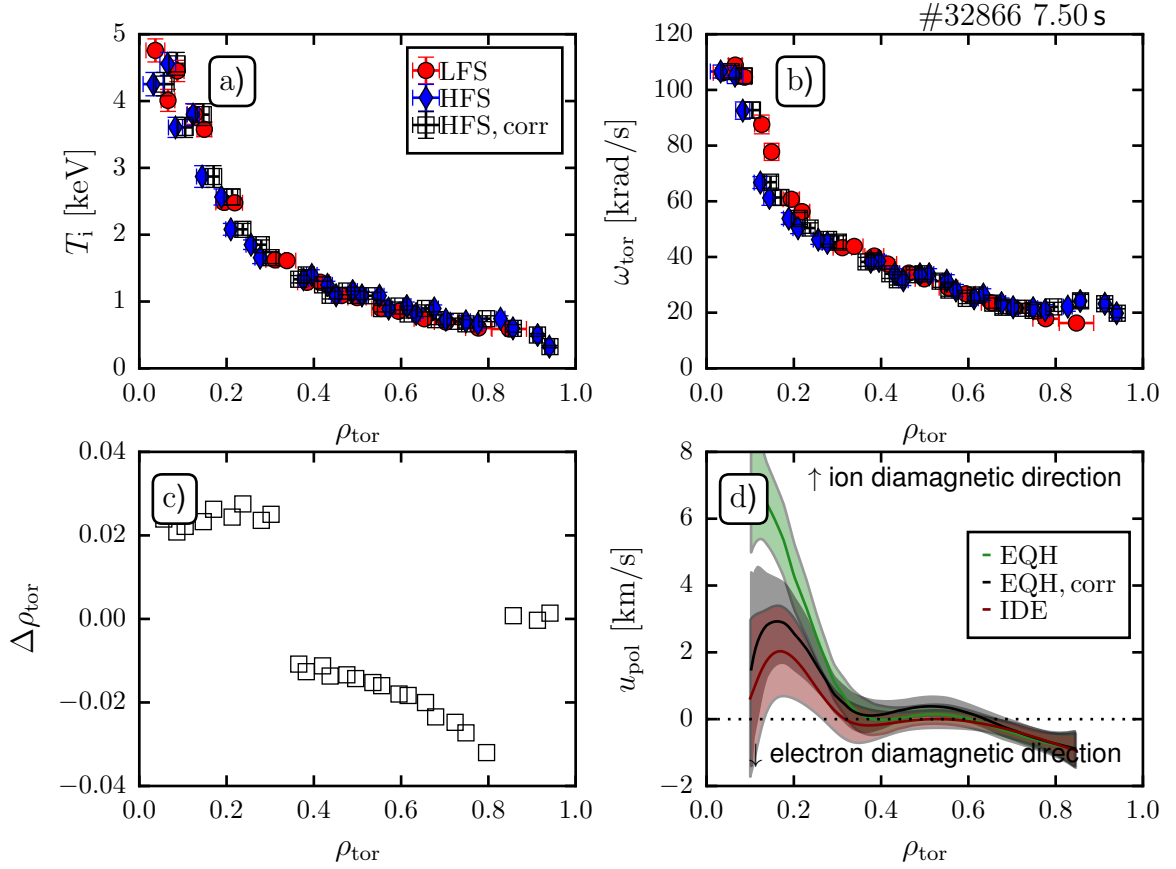


Figure 5.3: Illustration of uncertainties in the magnetic equilibrium on u_{pol} : (a) ion temperature (T_i) profiles on LFS (red) and HFS and the corresponding (b) ω_{tor} profile as a function of ρ_{tor} . The observed asymmetry in T_i has been corrected by shifts of the HFS profiles by roughly (c) $0.02 \sim 1$ cm and the corresponding profiles are shown in (a) and (b) with black squares. The resulting u_{pol} profiles are shown in (d) for the uncorrected equilibrium in green and with the shifted profiles in black. Additionally, the u_{pol} profile calculated with an advanced magnetic equilibrium (IDE) is shown in maroon.

by roughly $\Delta \rho_{\text{tor}} = 0.02$ or $\Delta r = 1$ cm (see figure 5.3c), which is within the uncertainties of the magnetic pickup coils. With the un-shifted profiles, u_{pol} values of up to 7 km/s are reconstructed inside $\rho_{\text{tor}} < 0.3$ (see green profile in figure 5.3d). Taking the shifted profiles, the maximum poloidal rotation is reduced to roughly 3 km/s, which is then in agreement with the u_{pol} reconstruction done with the advanced equilibrium code IDE. In this advanced equilibrium, the fast ion and thermal pressure profiles are included and the T_i profile is found to be symmetric such that no additional shifts are needed. Even though there are similar shifts necessary for $\rho_{\text{tor}} > 0.3$, all reconstruction methods show very similar values in this region. This results from the fact that the toroidal rotation frequency (ω_{tor}) profile is significantly flatter there than inside $\rho_{\text{tor}} = 0.3$ and the applied shifts have, therefore, only a minor influence on the reconstructed poloidal

rotation profile. This example illustrates that the outlined procedure of shifting the HFS profiles is a good approach to take care of inconsistencies in the magnetic equilibrium.

In order to validate this approach further and estimate the uncertainties introduced by the shifting of the HFS T_i and ω_{tor} profiles, this approach is compared to various equilibrium reconstructions for a larger number of profiles. For this, radial plots of the measured profiles are not particularly useful. Instead, time windows are selected over which the plasma is stable and the measured profiles are averaged over this time window. The averaged radial profile is then evenly divided into 10 ρ_{tor} bins and the averaged value is calculated per bin. Figure 5.4 illustrates this procedure. Panel a shows the experimental (red) and neoclassical (black) poloidal rotation profiles with corresponding error bars as well as the 10 radial bins. Panel b displays the averaged profiles from each radial bin in a chart where the x -axis corresponds to the experimentally measured u_{pol} values and the y -axis to the NC profiles from NEOART. Additionally, the 1-1 line (black line) is shown with a band of ± 1 km/s. In the case that the experimental values and the neoclassical predictions agree, they would lie on top of the 1-1 line. By using this format a large number of plasma discharges can be compared and it will become the standard diagram to compare the u_{pol} profiles from NC theory and the indirect measurement throughout this thesis. From figure 5.4a and b it can be seen that the poloidal rotation in the plasma core for this discharge is non-neoclassical. It points in the ion diamagnetic direction whereas the neoclassical prediction is in the electron diamagnetic direction. In the outer half of the plasma and towards the plasma edge ($\rho_{\text{tor}} > 0.6$) the experimental measurement direction switches to the electron diamagnetic direction and agrees with the predictions to within ± 1 km/s. This observation explains the fact that three data points lie in the sketched error band and the others outside of it (see figure 5.4b). The comparison shown here between experiment and theory is typical for the behavior observed in L- and H-mode discharges. Further information on this topic will be given in chapter 6, where the assembled poloidal rotation database is presented.

Using this method, the measured poloidal rotation profiles, taken from multiple time windows in the plasma discharge #32866, are compared in figure 5.5. Each panel corresponds to a different equilibrium used for the evaluation of the ‘measured’ data. In total, four different equilibria are compared: the standard EQH equilibrium, the EQH equilibrium with shifts according to the procedure outlined above, the IDE equilibrium and the EQI equilibrium taking pressure constraints into account. The averaged and binned u_{pol} values are displayed with black circles. The highlighted blue data points are due to inconsistencies in the magnetic equilibrium, which is very pronounced in the

Method	$\bar{u}_{\text{pol,exp.}}$ [km/s]	$\bar{u}_{\text{pol,NC}}$ [km/s]
EQH	(0.15 ± 0.7)	(-0.7 ± 0.2)
EQH + shifts	(0.17 ± 0.5)	(-0.7 ± 0.2)
IDE	(0.04 ± 0.4)	(-0.7 ± 0.2)
EQI + press. constr.	(-0.03 ± 0.6)	(-0.7 ± 0.2)

Table 5.1: Comparison of the weighted u_{pol} values for the different equilibria / methods.

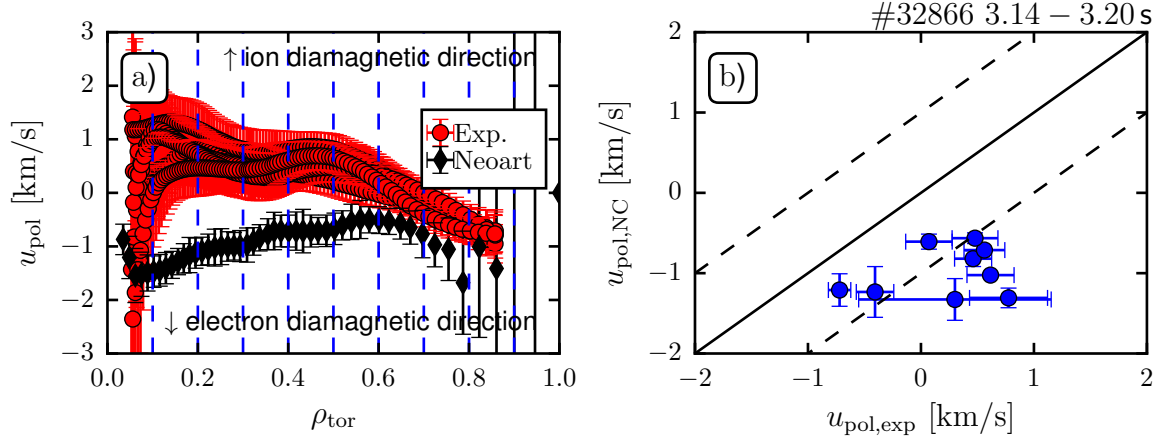


Figure 5.4: Introduction of the standard figure to compare the measured u_{pol} values to theory: (a) shows the u_{pol} profiles from the indirect measurement (red) and the corresponding profiles from NEOART (black) for the time interval 3.14 s to 3.2 s of the discharge #32866 and the 10 radial bins. (b) displays the corresponding plot of the experimentally measured poloidal rotations (x -axis) versus the neoclassical predicted poloidal rotation (y -axis) for the different intervals shown in (a).

standard EQH equilibrium and still visible in the EQI equilibrium with additional thermal pressure constraints. The bulk of the experimental points (black filled circles) is, however, very similar between all different equilibria. There is a significant shift of the experimental data from the 1-1 line in the ion diamagnetic direction. In order to compare the different poloidal rotation reconstructions, a weighted u_{pol} value is calculated for each equilibrium taking the error bars of the individual points into account. From table 5.1 it can be seen that all four cases have slightly different weighted poloidal rotations (-0.03 to $+0.17$ km/s). Comparing the diagrams in panels b and c, it can be seen that the differences in the values are small and that the shifting of the T_i profiles enables us to get rid of inconsistencies in the magnetic equilibrium making this approach viable for reconstructing u_{pol} for a large set of profiles. The difference between the largest and smallest value of table 5.1 can be taken as a first estimate of the error introduced from the magnetic equilibrium, i.e. ± 0.1 km/s.

5.3 Uncertainties in the q-profile

At AUG, the plasma current profile is reconstructed based on data from the magnetic pick up coils (see section 2.4) for the standard magnetic equilibria. The poloidal magnetic field is then given by the integral of the plasma current from the plasma core to the measurement position. The total plasma current is known very well. The exact distribution, however, is not well known and, therefore, the local B_{pol} in the plasma core is rather uncertain. Local measurements of the plasma current from the MSE, iMSE or polarimetry diagnostic provide additional information on the distribution of the plasma current (see section 2.4.2) and, hence, reduce the uncertainties in B_{pol} . It was shown in

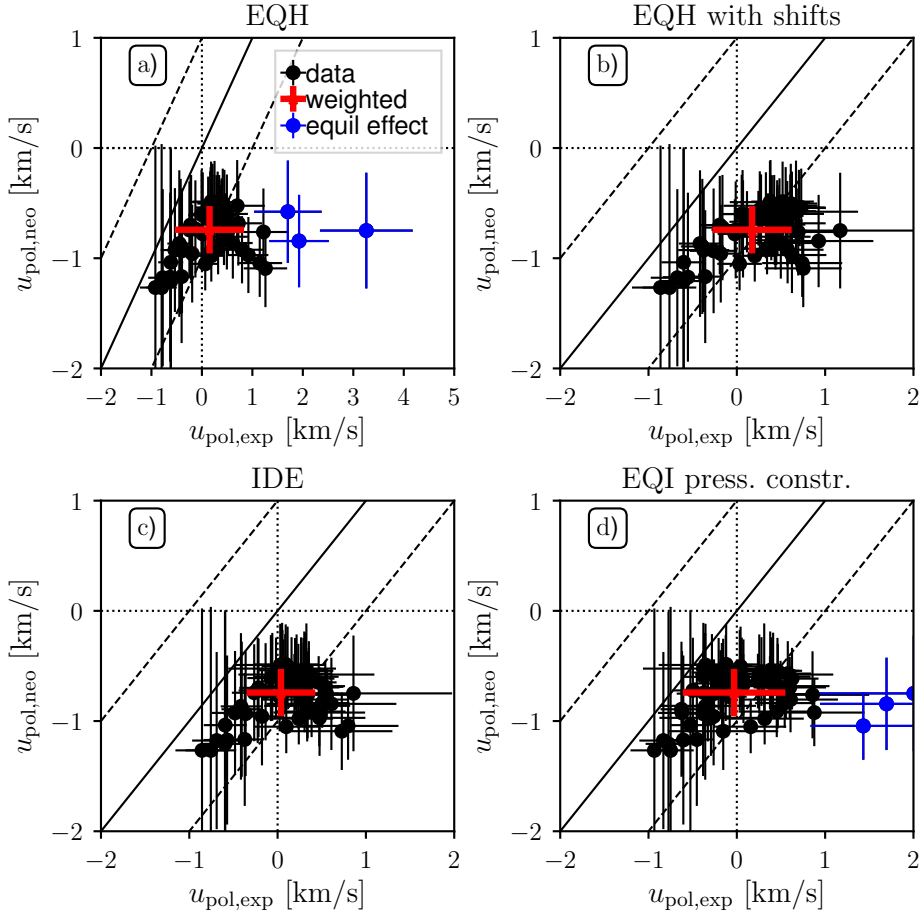


Figure 5.5: Comparison of the experimental u_{pol} values to neoclassical predictions calculated with NEOART for the discharge #32866 for four different magnetic equilibria: (a) standard EQH equilibrium, (b) EQH equilibrium with T_i corrections, (c) IDE equilibrium, and (d) EQI equilibrium with pressure constraints. The averaged and binned poloidal rotation values are shown in black circles with statistical error bars and measurement uncertainties for the experiment and NEOART. Data points that are linked to uncertainties in the magnetic equilibrium are highlighted in blue. Additionally, the weighted poloidal rotation is shown in red.

section 4.6.2 and in equation (3.31) that the poloidal rotation is given by the projection of the parallel plasma flow in the poloidal direction, i.e. as the product of the poloidal magnetic field with the flux function \hat{u} . Uncertainties in the magnetic equilibrium and in B_{pol} especially will, therefore, directly affect the u_{pol} reconstruction.

The q -profile¹ (blue) from the IDE code is shown in figure 5.6a. This code takes additional information into account from the MSE and POL diagnostics for the reconstruction of the plasma current. Additionally, the confidence band of the reconstruction

¹In a circular approximation, the local relation between toroidal magnetic field (B_{tor}) and B_{pol} gives the q -profile: $q = rB_{\text{tor}}/RB_{\text{pol}}$.

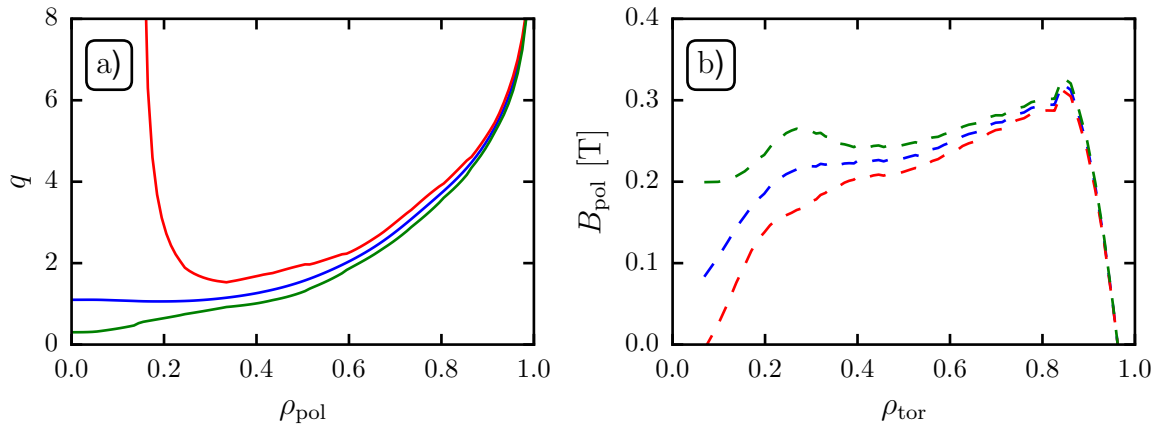


Figure 5.6: The IDE code provides (a) a confidence band on the q -profile (blue line: measurement, red: upper boundary; green: lower boundary). Taking the exact geometry of the flux functions into account, it is possible to calculate as well upper and lower values for (b) B_{pol} which gives an error estimation for the magnetic equilibrium.

is shown (upper boundary in red and lower boundary in green). One can see that the q -profile is known rather well for $\rho_{\text{pol}} > 0.3$ but the confidence band further inside is quite large. With these boundaries and by taking the exact geometry of the flux functions into account, one can calculate as well the upper and lower values for B_{pol} as shown in figure 5.6b. The relative uncertainty in B_{pol} in the plasma core is on the order of 100 % and gets smaller when going to larger radial values. Radial locations smaller than $\rho_{\text{tor}} = 0.2$ are of little interest since this region is dominated by MHD instabilities.

5.4 Phenomenology on impurity density asymmetries

A HFS-LFS impurity density asymmetry can have an impact on the indirect measurement of the poloidal rotation since, in this case, additional terms have to be added to the reconstruction algorithm (see section 3.3.2). It has been observed previously at AUG [148] and Alcator C-Mod [149] that there is an asymmetry in the impurity density profile located at the edge of the plasma. Up to now, however, it is unclear how far this asymmetry extends inwards. The new HFS-LFS spectrometer (see section 4.3) offers the opportunity to have a precise measurement of the n_{imp} profile across the entire plasma, so that the asymmetry itself as well as the starting point of the asymmetry can be determined. Before discussing the observations of n_{imp} asymmetries, the procedure for calculating the impurity density profiles from the measured CXRS intensities is outlined briefly.

The measured intensity from an active CXRS emission line can be directly linked to the impurity density as shown in equation (4.2). The assumption is made that n_{imp} is constant along a LOS such that it can be put in front of the integral. The evaluation of the n_{imp} profile is done with the charge impurity concentration analysis (CHICA) [150]

code. CHICA provides four different methods to calculate, respectively measure the line integrals of the neutrals along the diagnostic LOS. Two out of these four methods, namely the fast analysis and the collisional radiative model, are similar and will be treated as one reconstruction method in the following.

- Fast ion D_α simulation (FIDASIM) code: This code performs a Monte-Carlo simulation of the D_α spectrum. It includes a comprehensive physics model and allows for spreading of the beam and halo particles via collisions. This method is rather time consuming since the evaluation of one time point lasts roughly 0.5 to 5 min.
- Collisional radiative model and fast code: This method is based on a pencil code for the beam attenuation in the plasma and has also a halo model incorporated. The model assumes a steady state and takes a fixed geometry for the reconstruction such that a fast calculation of n_{imp} is possible (1 to 2 s per time point).
- Direct measurement with beam emission spectroscopy (BES): This technique uses the measurement of the $n = 3$ to $n = 2$ Balmer alpha line (D_α) of all energy components of the neutral beams. Using the same collisional radiative model as the above two methods, the populations of $n = 1$ and $n = 2$ atomic states can be reconstructed and the n_{imp} profile evaluated.

A detailed comparison between all reconstruction methods was performed for the plasma discharge # 32866 from 3.1 to 3.5 s. Figure 5.7 compares the resulting n_{imp} profiles for the different reconstruction methods. It has to be denoted that while the profile shape is the same for all methods (see figure 5.7a) a correction factor for the absolute magnitude of the impurity density profile had to be introduced in order to account for the different amplitudes of the n_{imp} profiles. The difference comes from the fact that FIDASIM and BES are predicting fewer neutrals than calculated with the fast/collisional radiative model. A reduced number of neutrals leads to higher n_{imp} values for the same measured intensity according to equation (4.2). Comparing the $n = 1$ and $n = 2$ states of the deuterium neutrals for the LFS (see figures 5.7c and d), one can see that the shape of the full energy component and halo predictions agree very well for the fast, collisional radiative model, and FIDASIM. The BES diagnostic, however, measures higher neutral densities for the halo (see figure 5.7d) and a smaller contribution for the full energy component (see figure 5.7c) for $\rho_{\text{pol}} > 0.6$. This could be related to the fact that the angle between the LOS and the beam injection direction is near 90° for the LFS making it harder to distinguish the different contributions from the passive D_α background. The associated Doppler shift is small and the different contributions are not well separated.

Figure 5.7b shows the comparison of the n_{imp} profiles on LFS and HFS. All considered reconstruction methods show that the n_{imp} profile is roughly four times higher on the HFS pedestal top than on the LFS. The onset of the n_{imp} asymmetry varies slightly between the different reconstruction methods. The BES diagnostic measures a faster attenuation of the full energy component and, therefore, an earlier starting point of the impurity density asymmetry

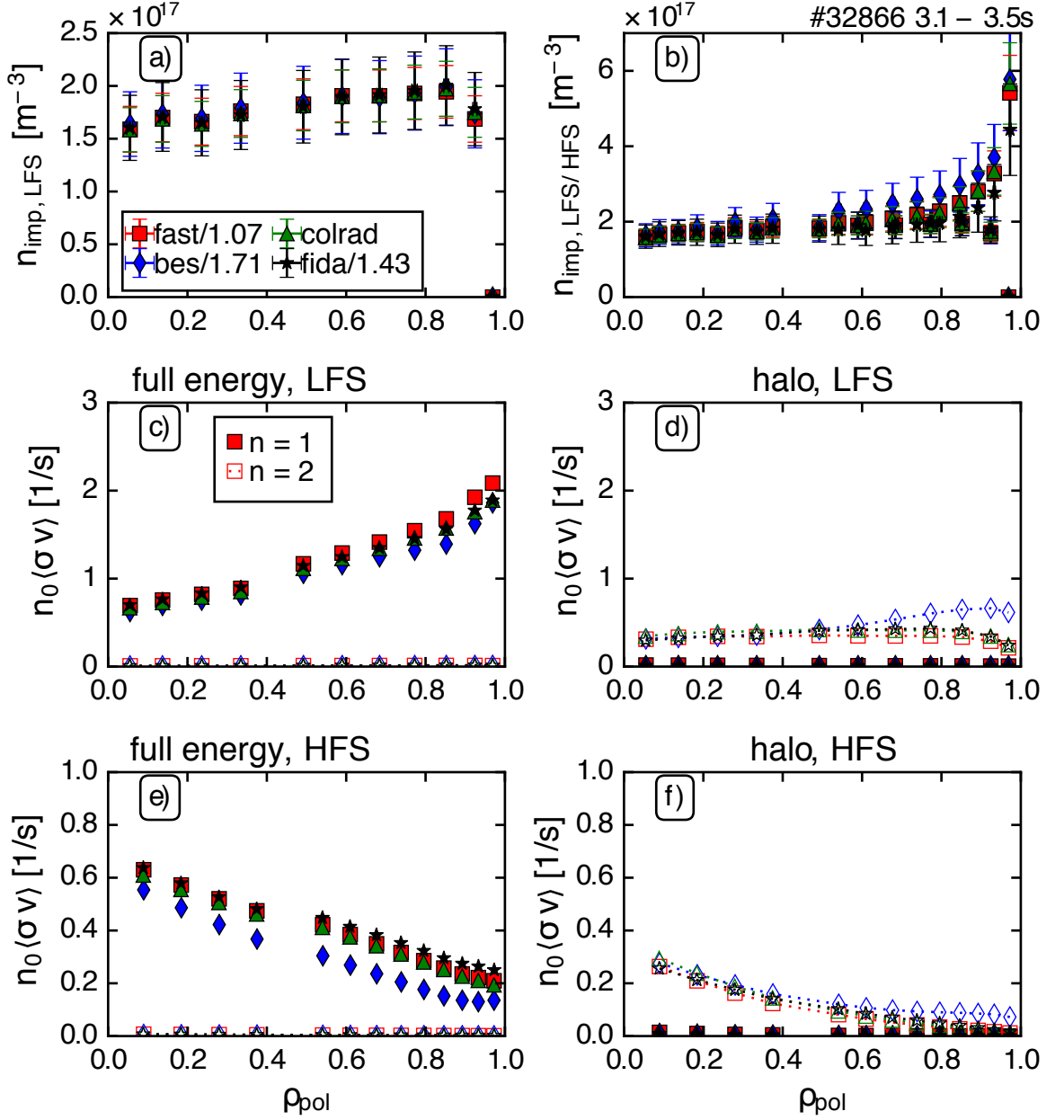


Figure 5.7: Comparison of the reconstructed n_{imp} profiles on (a) the LFS and (b) the HFS using different reconstruction methods (fast, collisional radiative model, FIDASIM and BES). Additionally, (c)-(f) the $n = 1$ (filled symbols) and $n = 2$ (empty symbols) are shown for the most important contributions, i.e. the full energy component of the beam (E1) and the beam halo. The densities (a) and (b) and the neutral contributions (c)-(f) are multiplied with a normalization factor (fast code: 1.07, FIDASIM: 1.43, and bes: 1.71) so that the integrated LFS n_{imp} profile match to the calculation done with the collisional radiative model.

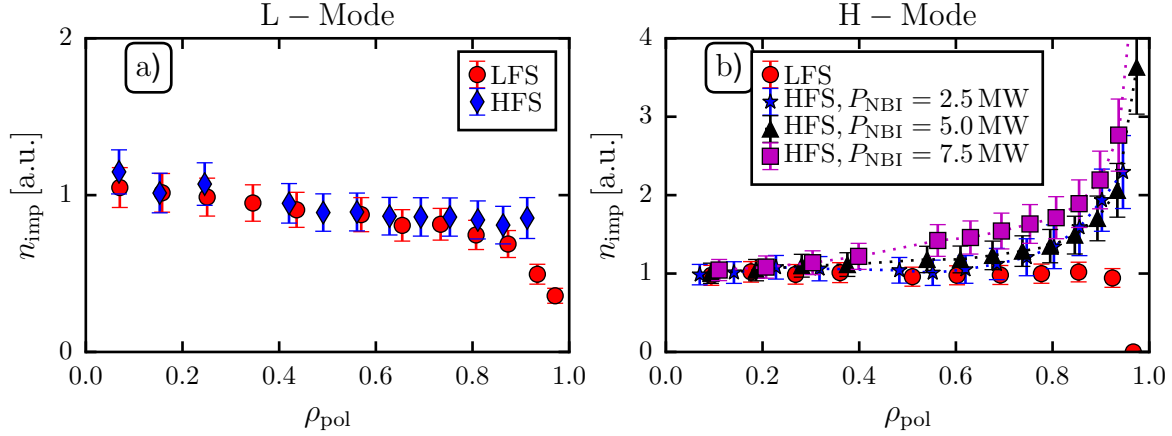


Figure 5.8: Comparison of the n_{imp} profile between LFS and HFS and in two distinct plasma regimes: L-mode (a) and H-mode (b). The impurity densities are normalized in the region between $0 < \rho_{\text{tor}} < 0.3$ such that asymmetries between LFS and HFS can be compared for different time points and plasma densities.

For this thesis, the new HFS-LFS spectrometer was operated for two complete campaigns with roughly 3500 shots. The observation of an asymmetry in the impurity density profiles was a standard investigation and can be best described by the following for L-mode and H-mode plasmas (see as well figure 5.8):

1. In L-mode plasmas, there is in general no impurity density asymmetry observed and the n_{imp} profiles match very well between the LFS and the HFS (see figure 5.8a). The usage of auxiliary power in these plasmas, however, is mostly restricted to NBI blips or to operation with reduced voltage. With the latter option, the signal on the HFS drops significantly (due to the stronger attenuation of the neutral beam at lower injection voltage) such that the observations are restricted to L-mode plasmas with NBI blips. In these cases, the impurity density reconstruction relies on the BES diagnostic.
2. In H-mode plasmas, n_{imp} asymmetries are regularly observed near the pedestal region with the HFS pedestal n_{imp} being a factor of 4 higher than the LFS (see figure 5.8b). The starting point of the n_{imp} asymmetry and relative amplitude between LFS and HFS varies with the applied heating power (see figure 5.8b). This dependency, however, was not investigated further in the framework of this thesis.

In figure 5.9, the u_{pol} reconstruction is compared taking the n_{imp} asymmetry into account (blue) and without the asymmetry (red). The reconstruction is done for the time point with the largest n_{imp} asymmetry in figure 5.8. It can be seen that it affects the reconstruction mostly at the plasma edge ($\rho_{\text{pol}} > 0.9$), where it brings the measured values to typical values of u_{pol} observed in the edge transport barrier. Further inside, i.e. $\rho_{\text{pol}} < 0.9$, the u_{pol} profile is unaffected. Since this thesis treats the core poloidal flow, the asymmetry in the n_{imp} profile can, in general, be ignored.

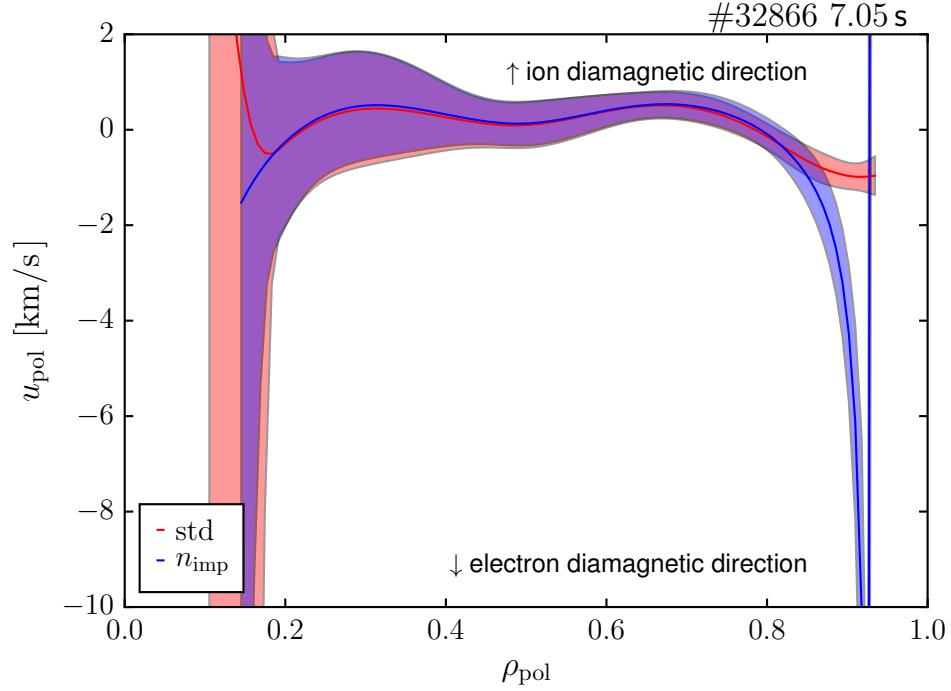


Figure 5.9: Comparison of the standard u_{pol} reconstruction (red) with a reconstruction taking the n_{imp} asymmetry into account (blue).

5.5 Changing the drift directions

The coordinate system of the indirect measurement technique is independent of the configuration of plasma current and toroidal magnetic field direction and gives an absolute direction of the poloidal rotation in terms of the poloidal angle θ . The poloidal rotation is the projection of the plasma flow into the machine coordinate system and the plasma flow is dominated by turbulence and drifts related to the magnetic field topology. The physics coordinates to describe the direction of u_{pol} are, therefore, the ion and electron diamagnetic drift directions, i.e. in which direction (upwards/downwards) propagates the ion or electron fluid due to the diamagnetic drift (see section 3.1.3). By changing the direction of the toroidal magnetic field, the electron and ion diamagnetic directions change sign relative to θ and the reconstructed u_{pol} changes sign accordingly. A very simple test of the reconstruction algorithm is, therefore, to change the drift directions by changing the direction of the toroidal magnetic and to compare the resulting u_{pol} profiles in time windows with similar plasma conditions.

The reversal of B_{tor} cannot be done in the lower single null (LSN) configuration since the divertor tiles of the lower divertor are optimized for operation with a toroidal magnetic field in the counter-clockwise direction which will be called negative direction in the following. Therefore, the upper single null (USN) configuration was taken (see figure 5.10c) for this test of the reconstruction method. This configuration is characterized by the fact that the magnetic field lines of the separatrix (red/black line) end in the upper divertor instead of the lower divertor. Figure 5.10a shows that the time trace of

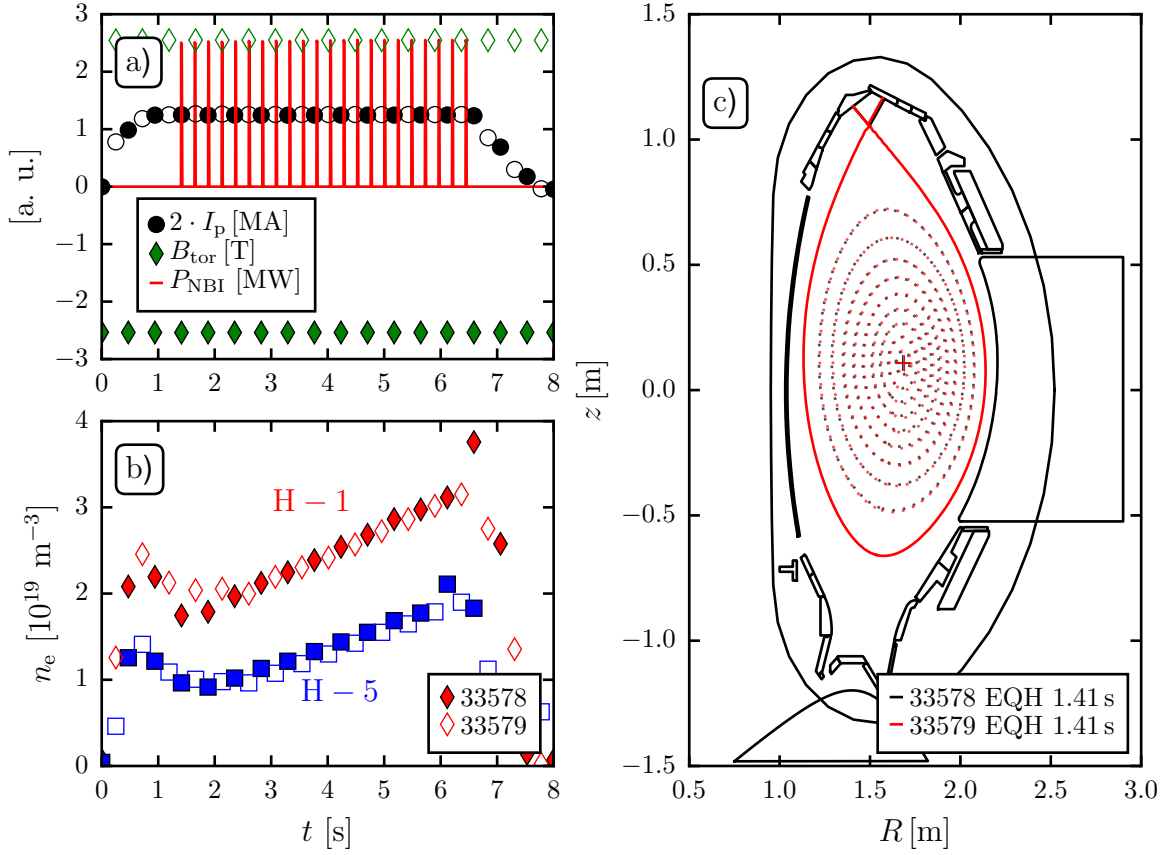


Figure 5.10: Timetrace of (a) the plasma current (black circles), toroidal magnetic field (green diamonds), and the neutral beam power from source 8 (red line) and (b) of the line-integrated density from H-1 (red diamonds) and H-5 (blue squares) for a plasma discharge with standard B_{tor} direction (#33578, negative B_{tor} , filled symbols) and reversed B_{tor} (#33579, positive B_{tor} , open symbols). (c) The plasma shape, i.e. the positions of the different flux functions, is very well reproduced between the discharges.

the plasma current (600 MA) and the neutral beam power from source 8 (red line) agree very well between the discharges. An absolute value of $B_{tor} = 2.5$ T was taken which was negative in discharge #33578, i.e. counter-clockwise in the top-down view on AUG, and positive in discharge #33579 (compare open and filled green diamonds in figure 5.10a). Figure 5.10b shows that the electron densities in these plasmas were very similar.

Figure 5.11a-c show that the ion temperature, toroidal rotation frequency, and the $\hat{\omega}$ profiles are the same comparing the two discharges. The flux function \hat{u} is, however, in opposite directions for the discharges with positive (green) and negative (brown) B_{tor} . Therefore, the u_{pol} profiles point as well into different directions in the machine coordinate system (see panel e) which is in both cases the ion diamagnetic direction (see figure 5.11f). The different sizes of the error bars result from different CXRS signal levels between the two discharges, i.e. the impurity content in the discharge #33579

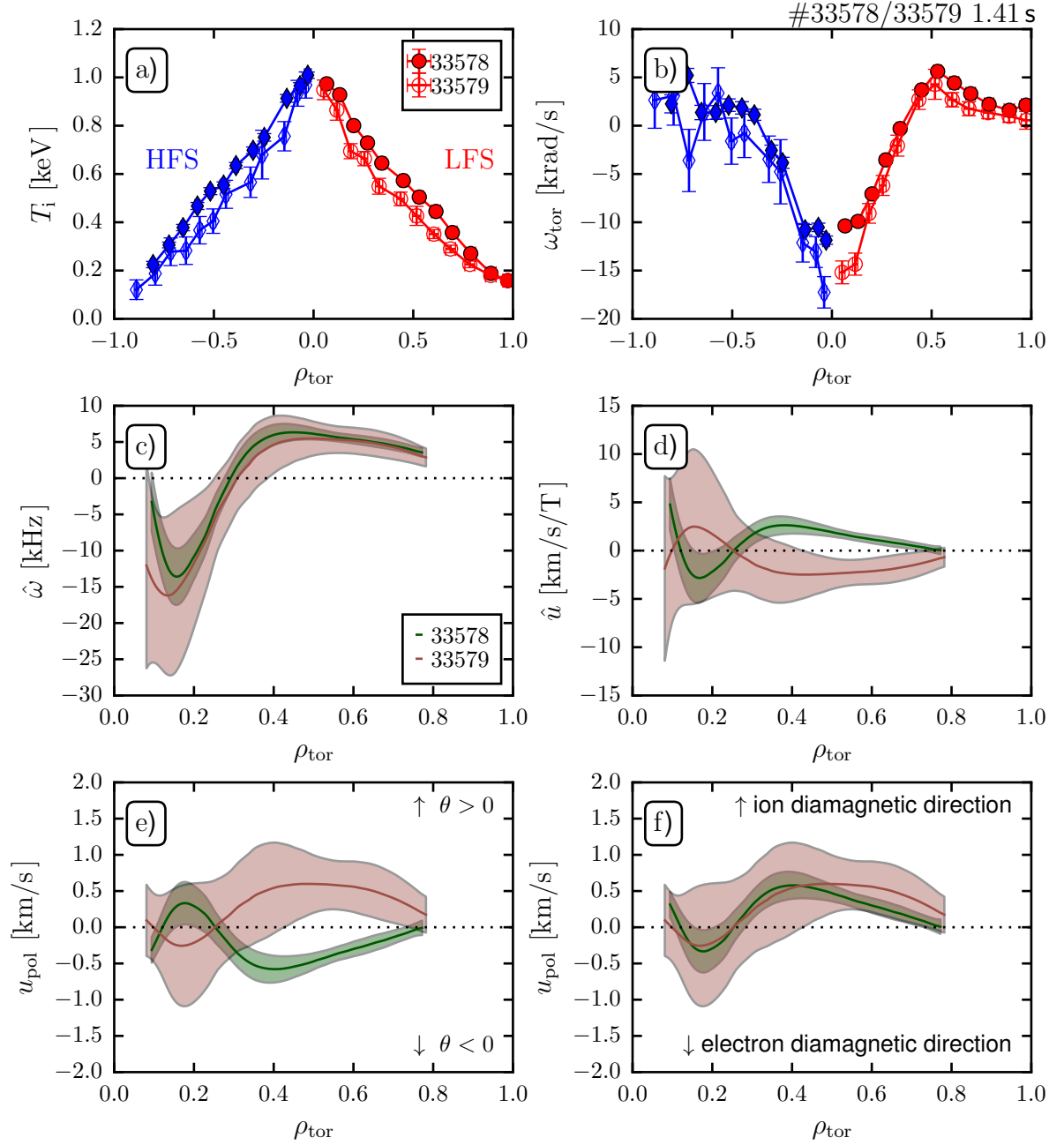


Figure 5.11: Profile of (a) the ion temperature and (b) the toroidal rotation frequency of the plasma discharge with negative B_{tor} (filled symbols) and positive B_{tor} (open symbols). The HFS profiles (blue) are plotted with a negative magnetic flux coordinate in order to distinguish them better from the LFS (red) profiles. Figures (c) and (d) show the flux functions \hat{u} and $\hat{\omega}$ for #33578 in green and #33579 in brown. The poloidal rotation profile is shown in the machine coordinates in (e) and relative to the electron and ion diamagnetic drift direction in (f).

was smaller compared to #33578. This set of discharges is a nice illustration of the measurement principle and shows that the drift directions are properly reconstructed.

Chapter 6

Characterisation of the core poloidal flow structure at ASDEX Upgrade

In previous studies, direct measurements showed that the poloidal rotation is neoclassical in the edge region of AUG [151, 152] and Alcator C-Mod [153, 154]. In the plasma core, however, a wide variety of results has been obtained. While there are measurements with large discrepancies with the predictions [33–35, 155], other studies show agreement within the uncertainties of the measurements [29–32]. This is, in part, due to lower overall rotation values that are comparable to the corrections related to atomic physics effects [28, 141], as discussed in section 4.4. In addition, the signal to noise ratio decreases towards the plasma core leading to larger error bars of the CXRS measurements.

The upgrade of the core CXRS diagnostics at AUG (chapter 4 and [41, 42]) enables an indirect measurement of the core poloidal rotation through the evaluation of the inboard-outboard asymmetry of the toroidal rotation [38–40] with an accuracy better than 1 km/s [41]. Recent studies using this technique from TCV show a very good agreement with the neoclassical predictions at high collisionalities [40]. Calculating the differential rotation between impurity and main ion toroidal rotation, the main ion u_{pol} was derived at DIII-D to be significantly more in the ion diamagnetic direction as predicted from neoclassical theory at low collisionalities [37]. This behavior could be important for the confinement of future fusion devices like ITER, which will be operated at even lower collisionalities. In order to address the question of the nature of u_{pol} in the core of AUG plasmas, a database of experimentally measured impurity poloidal rotation velocities under different plasma scenarios has been built up and will be presented in this chapter.

6.1 Flow predictions from neoclassical theory

In the neoclassical theory, the impurity poloidal rotation can be understood as friction between the impurity and main ion such that it is additionally dependent on the main ion and impurity ion densities. Since the energy and momentum collision times are on the order of a few μs (see section 4.1, [133]), the main and impurity ion temperatures are expected to be equal and, therefore, the following equation for the impurity poloidal

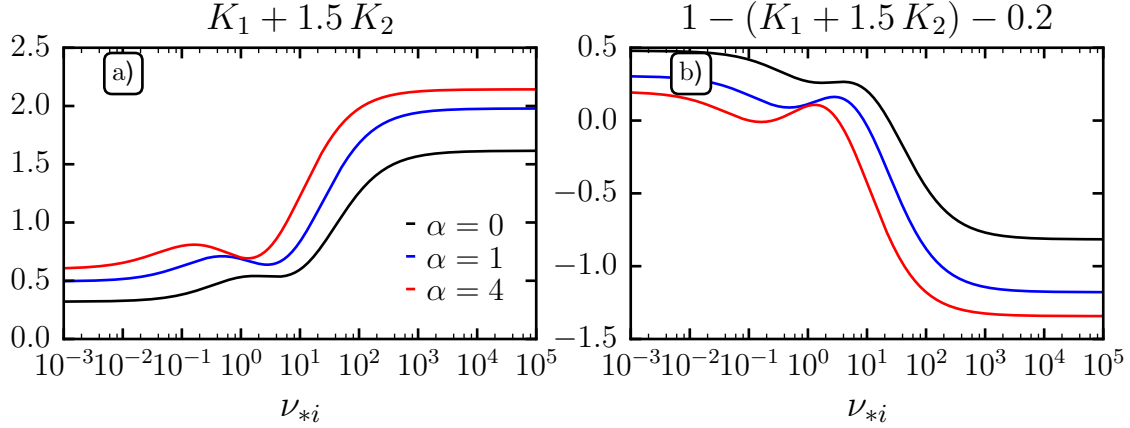


Figure 6.1: Dependence of the viscosity coefficients defined in [100] on the main ion collisionality and the impurity strength parameter $\alpha = n_Z Z_Z^2 / n_i Z_i^2$. (a) shows the sum of K_1 and K_2 as they occur in the equations for u_{pol} and (b) illustrates the factor C^* from equation (6.1) for B as trace impurity.

rotation can be derived [32]:

$$u_{\text{pol},Z} = \frac{B_{\text{tor}} T_i}{Z_i e \langle B^2 \rangle} \left[\frac{Z_i}{Z_Z} \frac{1}{n_{\text{imp}}} \frac{\partial n_{\text{imp}}}{\partial r} - \frac{1}{n_i} \frac{\partial n_i}{\partial r} - \frac{1}{T_i} \frac{\partial T_i}{\partial r} \underbrace{\left(1 - (K_1 + 1.5 K_2) - \frac{Z_i}{Z_Z} \right)}_{C^*} \right] \quad (6.1)$$

The impurity poloidal rotation is expected to depend mostly on the normalized gradients ($L_x = -\frac{1}{x} \frac{\partial x}{\partial r}$) of the impurity density, the main ion density and the main ion temperature with an additional ion temperature dependence through the factor in front of the bracket. There is an additional dependence on the collisionality via the viscosity coefficients K_1 and K_2 as introduced in section 3.4. Figure 6.1a shows the dependence of the sum $K_1 + 1.5 K_2$ for different impurity concentrations on the main ion collisionality defined as the ratio of the ion-ion collision frequency ν_{ii} to the bounce frequency: $\nu_{*i} = \nu_{ii} R q \epsilon^{-1.5} v_{\text{th},i}$. In terms of concentrations, the cases shown correspond to a pure deuterium plasma ($\alpha = 0$), and boron concentrations of 4% ($\alpha = 1$) and 16% ($\alpha = 4$). The boron concentrations in AUG are typically around 1 to 2% directly after boronizations and about 0.5% in the subsequent weeks after the boronization making the blue and black cases of interest for this work. This collisionality dependence leads to the fact that the contributions to the poloidal rotation from the main ion density (n_i) and T_i terms point into different directions: at low ν_{*i} , i. e. for $\nu_{*i} < 1-10$ (depending on α), C^* is positive and the contributions from the gradients in n_i and T_i add up. At higher collisionalities, the contributions point into opposite directions and partially cancel out.

In order to estimate the expected poloidal rotation values from NC theory for AUG, different u_{pol} profiles are calculated for a set of artificial kinetic input profiles with the code NEOART. In this study, the profiles of n_e , T_i , and n_{imp} were varied. The reason that the variation of n_i was substituted by a variation in n_e is based on the setup of the code. The implementation at AUG is designed to calculate the NC quantities from

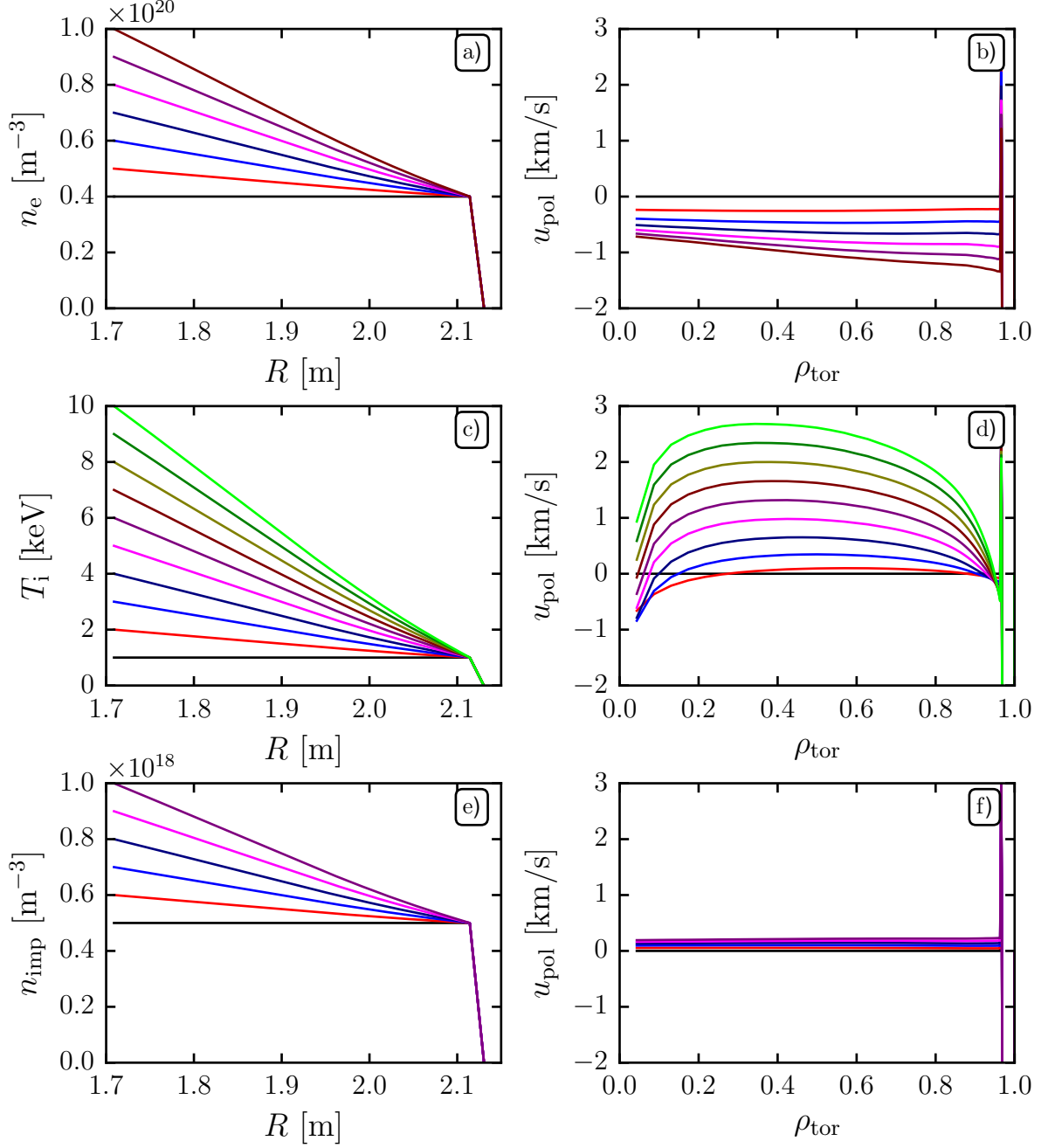


Figure 6.2: Calculation of the NC poloidal rotation (b, d, and f) for a set of artificial input profiles (a, c, and e). This figure shows a single parameter variation of the kinetic input profiles, i.e. the shown poloidal rotation velocities in the column on the right hand side reflect only changes in n_e , T_i , or n_{imp} . The gradients in the other profiles are set to zero (black profiles).

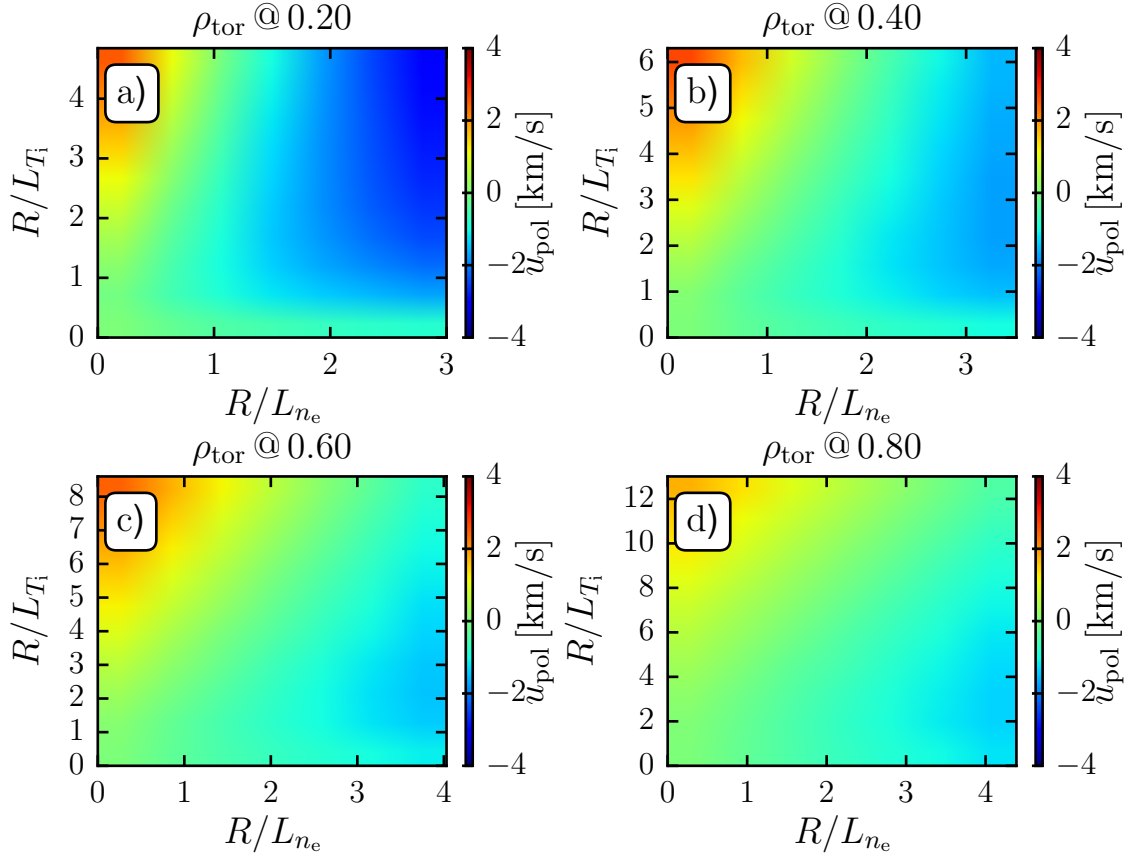


Figure 6.3: Combined variation of the normalized electron density and ion temperature gradient at different radial locations: (a) $\rho_{tor} = 0.2$, (b) $\rho_{tor} = 0.4$, (c) $\rho_{tor} = 0.6$, and (d) $\rho_{tor} = 0.8$ (same dataset as shown in figure 6.2).

experimental measurements. Since there are no direct measurements of the main ion density, the code calculates n_i from the electron density profile and the impurity density profiles, making use of the quasi-neutrality condition $n_e = \sum Z_i n_i$.

Figure 6.2 shows the input profiles in the left column and the resulting u_{pol} profiles in the panels on the right hand side in the same color coding. The variations shown here correspond to a single parameter variation, i.e. while the gradients in one quantity are varied, the other gradients are kept to zero (black profiles). It can be seen that the variation in T_i and n_e have the largest impact on the u_{pol} profile. The contributions point in different directions. The n_{imp} variations also affect n_i : A peaked n_{imp} profile leads to a hollow n_i profile if a flat n_e profile is taken. The actual effect of a pure n_{imp} variation, i.e. of a variation where n_i is kept the same, is expected to be even less than the variation shown, since the contributions from equation (6.1) for n_{imp} and n_i have different signs and the contributions from the hollow and peaked profile, therefore, add up.

This effect can also directly be seen directly from equation (6.1). The ranges of the experimentally measured normalized gradient lengths of n_{imp} and n_i are very similar and

thus the factors in front of the gradients matter. The contribution from the impurity density gradient is multiplied by Z_i/Z_Z , i.e. by the charge ratio between the main and impurity ion, which is 0.2 for the example shown here. This simple estimation is in-line with the calculations shown in figure 6.2.

The u_{pol} profiles in figure 6.2 are useful to get a first idea of the expected u_{pol} values but do not reflect the experimental conditions. Figure 6.3 shows, therefore, the simultaneous variation of the electron density and ion temperature gradient at different radial positions for the case of a flat impurity density profile: (a) $\rho_{\text{tor}} = 0.2$, (b) $\rho_{\text{tor}} = 0.4$, (c) $\rho_{\text{tor}} = 0.6$, and (d) $\rho_{\text{tor}} = 0.8$. The predicted u_{pol} values are shown as a contour plot where blue colors correspond to negative rotation velocities, i.e. in the electron diamagnetic direction, and colors in the red spectrum to positive rotation, i.e. in the ion diamagnetic direction. For the extreme cases, i.e. small gradients in n_e and large gradients in T_i (or vice versa), the same trends as in the previous figure are reproduced. With simultaneous gradients in n_e and T_i , the picture is a little bit different. Large gradients in n_e and T_i lead in panel (a), i.e. close to the magnetic axis of the plasma, to strong poloidal rotation velocities in the electron diamagnetic direction. Considering the other panels, however, the contributions from n_e and T_i are balanced out and rotation velocities at around zero are expected for these regions and parameters, since the contributions from the gradients in T_i and n_e cancel each other.

6.2 Comparison to different neoclassical codes

Chapter 4 showed that the toroidal rotation frequency is typically smaller on the HFS than on the LFS implying a poloidal flow in the ion diamagnetic direction for standard AUG geometry. The previous section illustrated that the neoclassical prediction of impurity u_{pol} depends on the gradients in n_i , T_i , and on the ion collisionality. Therefore, the experimentally measured kinetic profiles were taken to calculate the neoclassical predictions of u_{pol} .

Figure 6.4 shows the comparison of the experimentally measured impurity u_{pol} (black line) to predictions from the neoclassical codes NEOART (red triangles), NEO (blue diamonds) and NCLASS (green squares) for one time point of an L-mode discharge (see figure 6.4a) and one time point of an H-mode discharge (see figure 6.4b). There are no error bars on the u_{pol} profiles from NEO and NCLASS. For NEOART, a stand alone version was used and the kinetic input profiles were varied according to the uncertainties of their measurements (a similar procedure to the calculation of the error in the experimentally measured u_{pol} values). By calculating the mean and standard deviation of the poloidal rotation resulting from this variation, it was possible to provide realistic uncertainties on u_{pol} from NC theory, which are on the order of 1 km/s, i.e. roughly the same resolution as obtained with the indirect measurement technique. The errors on the NEOART profiles are assumed to be good estimates for the errors on the poloidal rotation profiles from NEO and NCLASS. Therefore, it can be seen from figure 6.4 that there is very good agreement between the different NC codes giving a poloidal rotation in the electron diamagnetic direction all across the plasma.

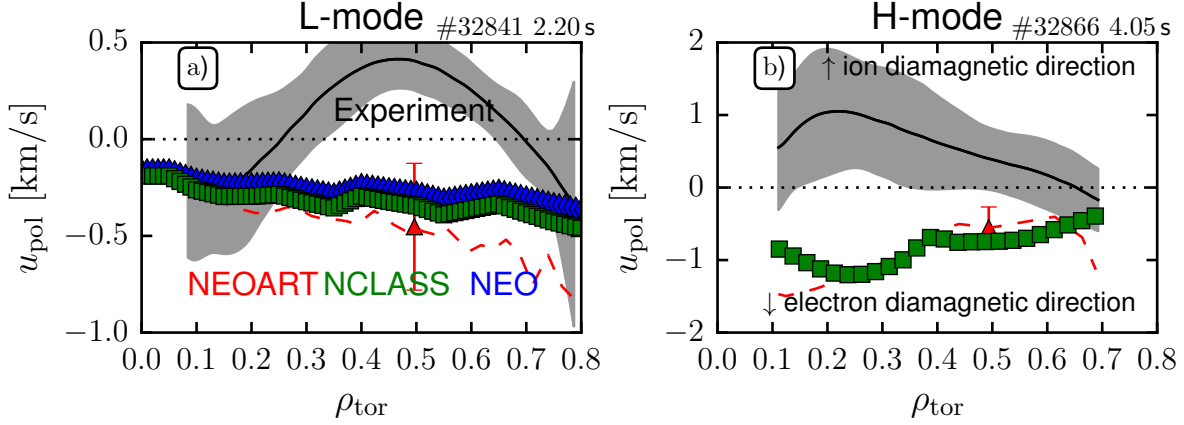


Figure 6.4: Comparison of experimentally measured poloidal rotation velocities with the indirect measurement technique (black) to neoclassical predictions from the codes NEOART (red), NEO (blue) and NCLASS (green) for one plasma discharge in (a) L-mode and one in (b) H-mode.

The experimentally measured poloidal rotation shown in figure 6.4 is, however, in the ion diamagnetic direction in the plasma core and switches sign to the electron diamagnetic direction towards the plasma edge. This means that the experimentally measured poloidal rotation is non neoclassical at mid-radius and in the core of H-mode plasmas. In order to study this observation in a more systematic way, a poloidal rotation database has been built up which will be presented in the following section. In addition, the L-mode portion of the database will be further discussed in chapter 7 when the poloidal rotation in Ohmically heated L-mode plasmas is discussed in greater depth.

6.3 Poloidal rotation database

This section is dedicated to the main physics goal of this work, i.e. the characterization of the core poloidal flow at AUG. It has been shown in previous sections that the flow in the core of AUG is consistently in the ion diamagnetic direction for both L-mode and H-mode plasmas. These profiles came, however, from individual time points of individual discharges and may not be representative of the full range of AUG discharges. Therefore, a database has been assembled that spans the available AUG parameter range. The individual entries of the database are gathered by averaging over stable time intervals of a plasma discharge and a radial binning into 10 equally spaced ρ_{tor} intervals (see as well section 5.2 and figure 5.4).

The poloidal rotation database was made with data from the 2015 campaign of AUG. This campaign had in total 1948 plasma discharges from # 31777 to # 33724 and interesting plasma discharges were selected, in a first step, according to the following criteria:

- The flat top of the plasma discharge is at least 2s and the main ion species is deuterium.

- The injected power of NBI source 8 has to be larger than 1.8 MW. For powers below this, the HFS CXRS signal is too low leading to large errors of the u_{pol} reconstruction.
- Additionally, it is required that information about certain quantities was written to shotfiles:
 - The raw data of the CXRS diagnostic with a corresponding Ne spectrum for the wavelength calibration.
 - Information on the magnetic equilibrium and the magnetic axis provided with the standard CLISTE evaluation
 - The standard diagnostics for the measurement of n_e and T_e as well as for the radiated power in the plasma.

These criteria lead to a reduction of the number of interesting discharges from 1948 to 616. In a second step, the discharges were checked further:

- Equilibrium: A stable plasma shape is required in order to minimize mapping effects from the real space coordinates to the magnetic flux functions. Therefore, it is for example required that there are stable phases in the discharge where the magnetic axis as well as the inner and outer radii of the plasma are not moving significantly.
- Phases of discharges were excluded where the external magnetic perturbation coils are used.
- The total heating power of NBI box II is limited to 5 MW. In order to avoid inferring CXRS signals from the sources 5 and 7, phases of plasma discharges with additional NBI heating from the sources 5 and 7 were excluded. Additionally, time intervals immediately before and after changes in auxiliary heating power from NBI, ECRH, and ICRH are excluded from the database.

With these additional constraints, the total number of usable shots is reduced to 198. In these discharges, time intervals were identified that are stable in terms of density, temperature, plasma radiation and heating power for at least 200 ms. This condition is, however, not applicable for L-mode discharges since these use NBI blips for measurement purposes.

It is relatively time consuming to calculate the NC and experimental u_{pol} profiles, meaning that it was not possible to add all of the mentioned discharges to the database. Instead, a subset of plasma discharges was identified that contains the largest possible scans in heating power, plasma current, normalized electron density gradient, normalized ion temperature gradient, and safety factor q and the database was built from these discharges. In total 70 time intervals from 19 discharges (4 L-mode and 15 H-mode discharges) were included into the database.

Figure 6.5 shows an overview of the assembled database. From panel (a) it can be seen that R/L_{n_e} is varied between 0 and 5 and R/L_{T_i} between 0 and 12. There is a number of

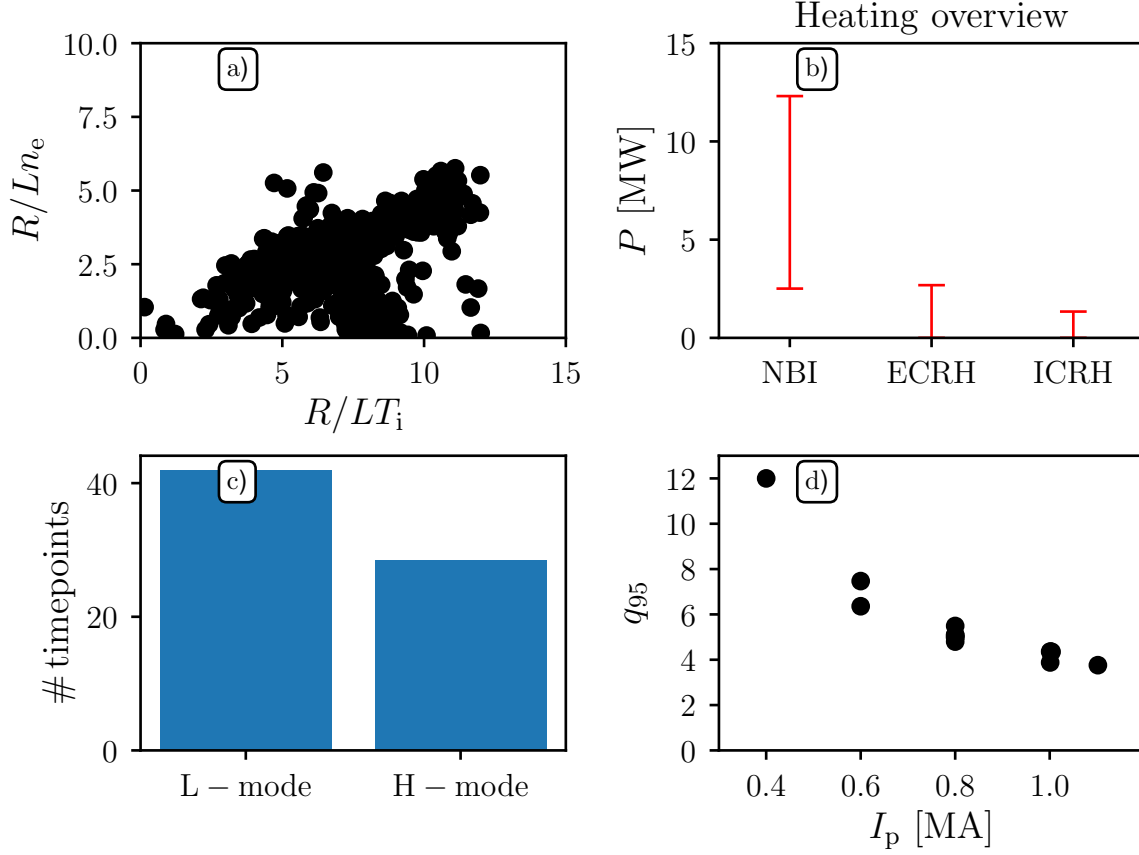


Figure 6.5: Overview of the assembled u_{pol} database showing (a) the variations in R/Ln_e and R/LT_i , (b) the auxiliary heating of the plasma for NBI, ECRH, and ICRH, (c) total number of time points in L-mode and H-mode discharges, and the variations of the edge safety factor and plasma current.

discharges which feature simultaneously large R/Ln_e and R/LT_i gradients and another set of discharges with small gradients in the electron density and large gradients in the ion temperature. Panel (b) shows the variation in the database in terms of auxiliary heating power from NBI ranging from 2.5 to 12.5 MW as well as the scan in ECRH and ICRH. Figure 6.5c illustrates that the current database consists of 42 time points from L-mode discharges and 28 points from H-mode discharges and panel (d) shows the variation in the edge safety factor q_{95} from 4.0 to 12.0 and of the plasma current from 0.4 to 1.1. These parameter variations cover the operational space of ASDEX Upgrade.

Figure 6.6 shows an overview over the complete database distinguishing between L-mode and H-mode data. Comparing the absolute variations in the theoretical predictions, it can be seen that the covered range of the u_{pol} profiles in H-mode (-1.2 to 0.0 km/s) is slightly larger than for L-mode (-1.0 to 0.0 km/s). This results from the different correlation between ion temperature gradient and electron density gradient and will be covered in the next section. Furthermore, the variation in the experimental data from L-mode is significantly more than from H-mode. This results from the different

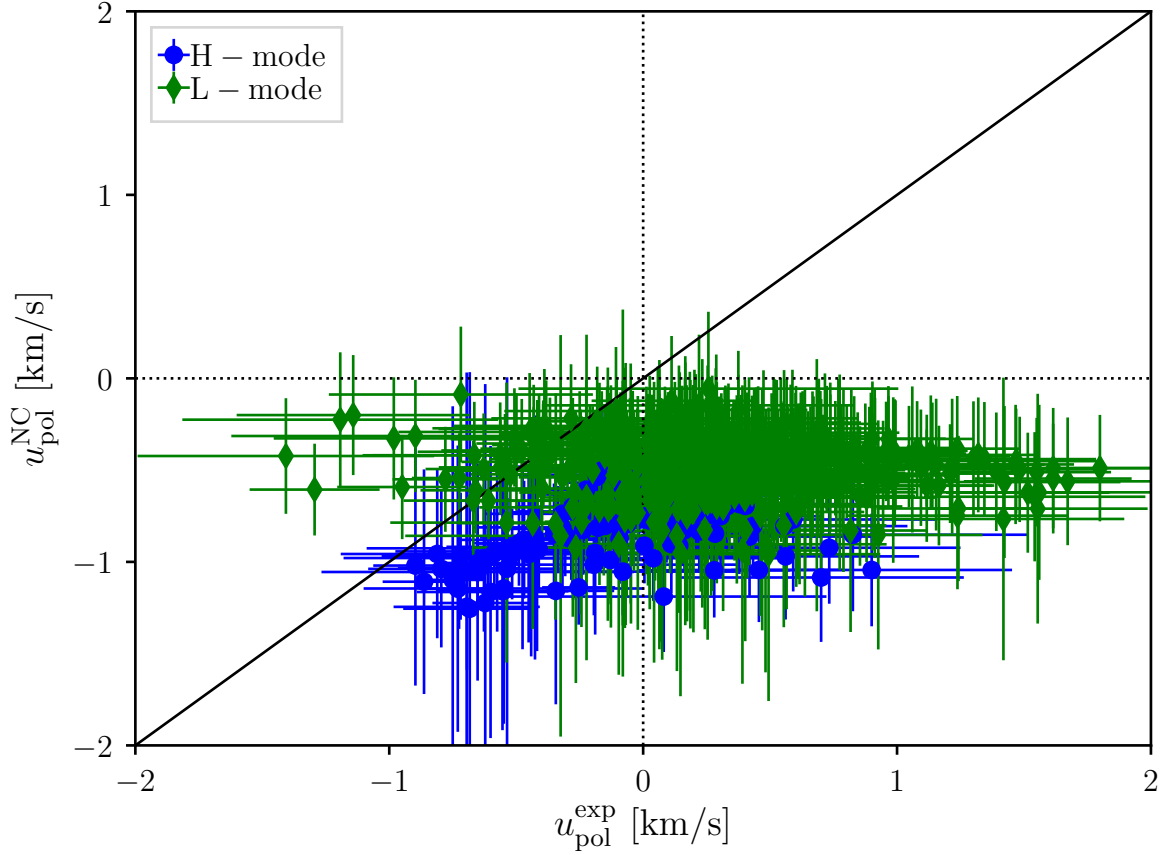


Figure 6.6: Overview over the assembled u_{pol} database with H-mode (blue) and L-mode (green) discharges. The estimation of the neoclassical poloidal rotation is done with the code NEOART.

measurements techniques in the two plasma scenarios. In H-mode, intervals where the plasma is stable are averaged leading to a reduction of the variation in the profiles.

It can be seen from figure 6.6 that for both plasma scenarios, the weighted mean of the data points is on the right hand side of the 1-1 line implying that the measured u_{pol} values are more in the ion diamagnetic direction than predicted from neoclassical theory. Additionally, there is a substantial number of points that have the opposite drift direction than predicted from neoclassical theory. This shift is outside of the error bars of the profiles and shows that there is a non neoclassical poloidal rotation for some regimes and/or certain radial regions at AUG.

In figure 6.6, the code NEOART is used for the evaluation of the neoclassical prediction for u_{pol} . For a subset of 6 discharges (4 L-mode and 2 H-mode discharges), there are as well predictions from the neoclassical codes NCLASS and NEO. A comparison between the u_{pol} profiles from the different codes can be found in figure 6.7. It can be seen that the profiles from the different codes agree in general well. Additionally, there are a region for NC predictions from NCLASS and NEO where NEOART predicts u_{pol}

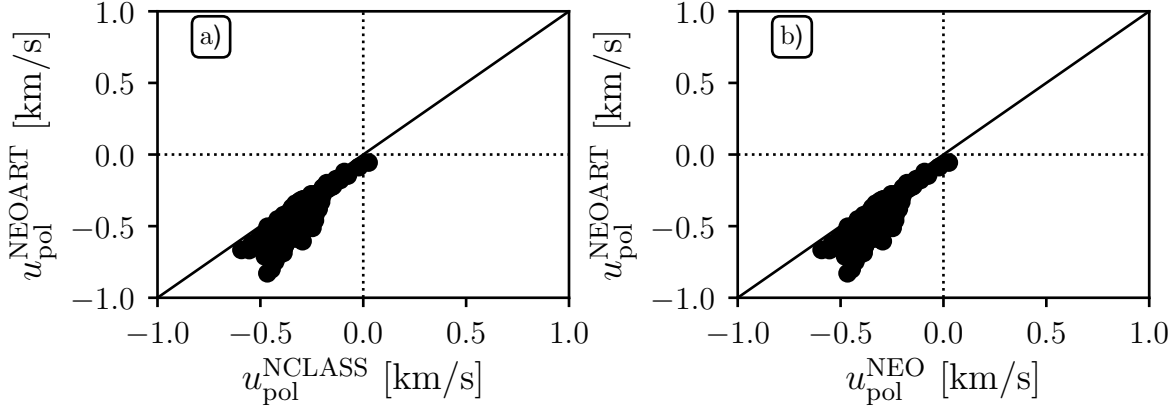


Figure 6.7: Comparison of the neoclassical predictions from NEOART (y -axis) to the neoclassical codes (a) NCLASS and (b) NEO.

values that are more in the electron diamagnetic direction than from the other codes, i.e. the cloud of the points is located below the 1-1 line.

In order to characterize the dependencies of the database further, it is separated according to radial regions in the plasma. The motivation for this results from figure 6.4 where it is shown that the u_{pol} profiles agree within the uncertainties with the neoclassical predictions towards the plasma edge and that the poloidal flow direction changes in the core from the electron diamagnetic direction to the ion diamagnetic direction. Figure 6.8 compares the profiles in the plasma core (left hand side) to the profiles outside of $\rho_{\text{tor}} = 0.6$ (right hand side). Additionally, the profiles are separated between H-mode (blue, top) and L-mode (mode, bottom). By comparing panel a and b one can see that this change in direction is present in the H-mode discharges: Most of the points from panel b align within their uncertainty with theory showing a similar trend as predicted from neoclassical theory. From panel a it can be seen that not all of the gathered data shows a different drift direction than predicted from neoclassical theory. This could point towards the fact that there are different dependencies present in this dataset which will be examined in the following. For the L-mode data, no clear trend is visible. The experimental data has large variations in both regions, the core and outside of $\rho_{\text{tor}} = 0.6$. This picture gets clearer when a change in the confinement regime is taken into account, which will be discussed further in the next chapter.

6.4 Parameter dependencies

The neoclassical prediction of u_{pol} depends on the collisionality and the gradients in the ion temperature and density profiles (see sections 3.4 and 6.1). In order to characterize the nature of the core poloidal flow at ASDEX Upgrade, these dependencies are tested with the database build up for this thesis.

Figure 6.9 examines the parameter dependencies on the L-mode dataset. Panels a, b, and c show the experimentally measured profiles in red and the theoretical predictions

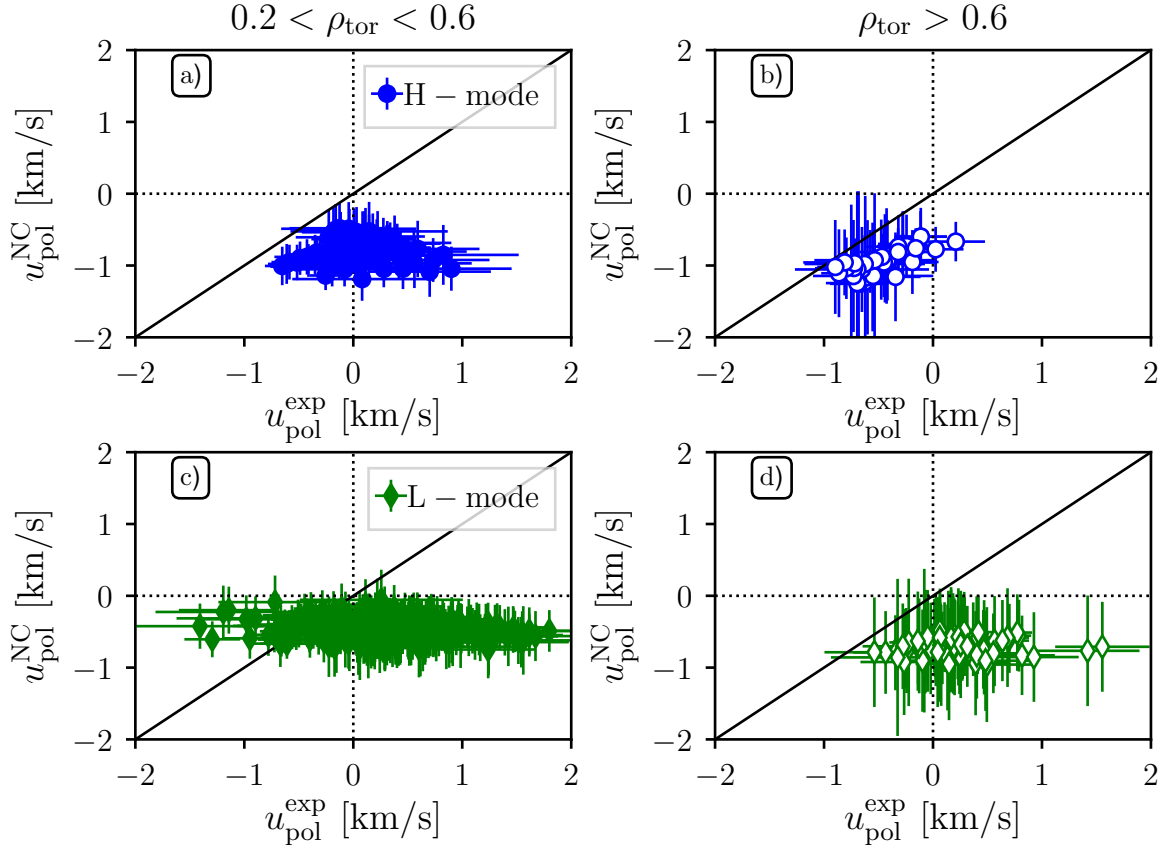


Figure 6.8: Comparison of the experimentally measured u_{pol} profiles with the neoclassical predictions in the plasma core (a, c) and outside of $\rho_{\text{tor}} = 0.6$ (b, d) for different plasma scenarios (H-mode: blue, L-mode: green).

in black as a function of R/L_{ne} (a), R/L_{Ti} (b), and the main ion collisionality (c). Similarly to the overview plot of the database (figure 6.6) no clear trends are visible. The experimental velocities are consistently more in the ion diamagnetic direction for larger R/L_{Ti} and R/L_{ne} values, but in general no clear correlation between the experimentally measured values with one of the parameters predicted from neoclassical theory is found. For the L-mode data, there is a clear correlation between the gradients in R/L_{Ti} and R/L_{ne} (see panel d) meaning that the largest gradients of density are present at the same time as the largest gradients in temperature.

The same parameter dependencies as for the L-mode are shown in figure 6.10 for the H-mode. The dependencies obtained with R/L_{Ti} and R/L_{ne} are slightly ambiguous. There are two branches for R/L_{ne} where the first one shows the opposite trend as predicted from theory, i.e. the measured u_{pol} values are more in the ion diamagnetic direction and the theoretical value goes slightly more in the electron diamagnetic direction. The other branch agrees within the uncertainties with the neoclassical predictions. These two branches relate to the different areas in the plasma, i.e. in the plasma core and outside of $\rho_{\text{tor}}=0.6$. A similar behavior is found when investigating the dependencies on

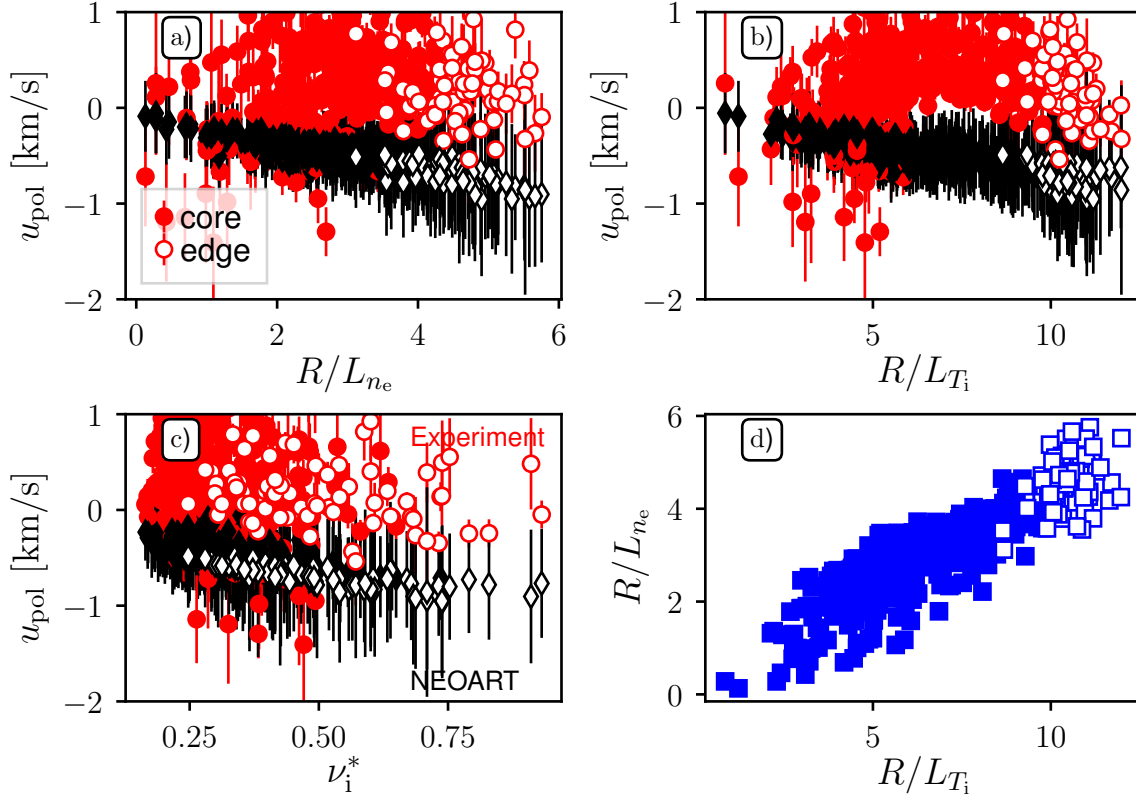


Figure 6.9: L-mode parameter dependencies of the experimentally measured u_{pol} profile (red) and the theoretical predictions (black) on (a) R/L_{ne} , (b) R/L_{Ti} , and (c) the ion collisionality. Additionally, the correlation between R/L_{ne} and R/L_{Ti} is shown in panel (d). Both, core (filled symbols) and edge (open symbols) data are shown.

the ion temperature gradient (panel b). There is one branch agreeing with the neoclassical predictions and the other one is shifted roughly by 1 km/s in the ion diamagnetic direction. From panel c, it can be seen that there is a clear trend with the collisionality: there is an increasing difference between the experimentally measured poloidal rotation velocities and the theoretically predicted ones for smaller collisionalities. This behavior is further illustrated in figure 6.11a where the trends of the experimental and theoretical u_{pol} values are shown. It can be seen that the difference between the measured impurity poloidal rotation and the predicted one from NEOART becomes larger for smaller collisionalities.

One explanation for the observation of non neoclassical poloidal rotation could be the effect of turbulence on the plasma flow. The turbulent drive is expected to grow with the square of the normalized Larmor radius (ρ^*) and in the H-mode dataset of the poloidal database a clear dependency on ρ^* is observed (see figure 6.11b), i.e. the difference between the experimentally measured and theoretically predicted impurity flows become larger with increasing ρ^* .

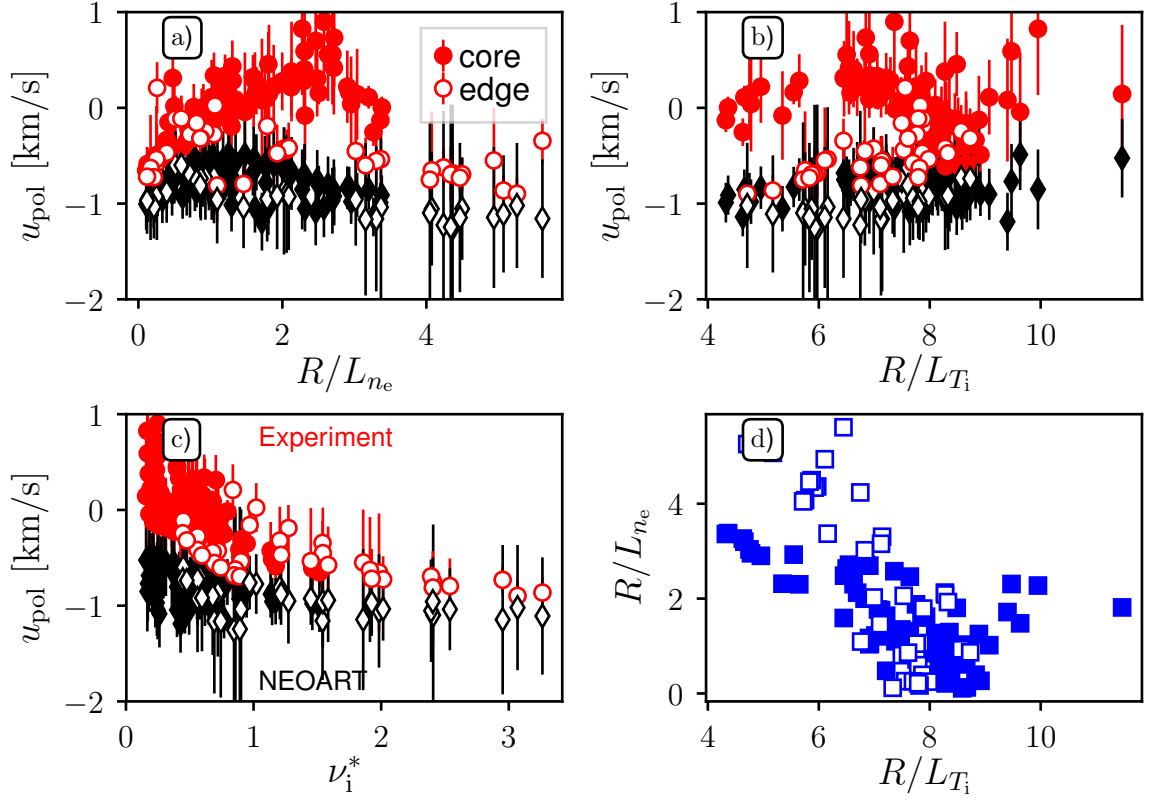


Figure 6.10: H-mode dependencies of the experimentally measured u_{pol} profile (red) and the theoretical predictions (black) on (a) R/L_{n_e} , (b) R/L_{T_i} , and (c) the ion collisionality. Additionally, the correlation between R/L_{n_e} and R/L_{T_i} is shown in panel (d). The data is shown in the same color coding as in figure 6.8: data points from the edge are shown with open symbols and those from the core with filled symbols.

It is important to note here that the neoclassical damping increases with collisionality. Therefore, a possible explanation of the observed dependencies is that there is a balance between neoclassical damping and turbulent drive of u_{pol} . At low collisionalities, i.e. when the neoclassical damping is the weakest and the turbulent drive the strongest, the experimental values show a clear non neoclassical poloidal rotation. With increasing collisionality, the turbulent drive decreases and the neoclassical damping increases such that the experimental values are neoclassical. In order to test this hypothesis an estimation of the Reynolds stress in the H-mode discharges is necessary, as for example done in [27, 34]. This investigation will be the topic of future experiments and publications since a precise measurement of the level of density fluctuations is necessary.

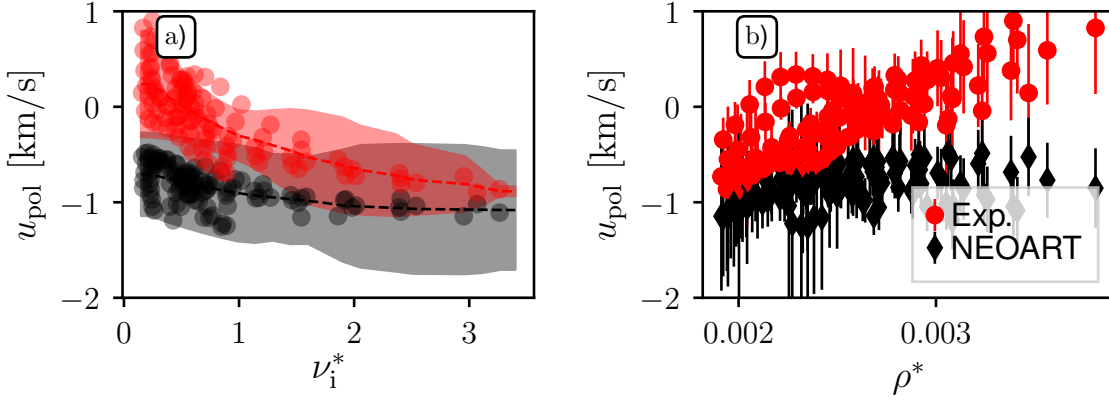


Figure 6.11: (a) Averaged poloidal rotation as a function of the main ion collisionality and (b) dependency of the poloidal rotation on the normalized Larmor radius.

6.5 Implications for the main ion poloidal rotation

The experimental data presented so far corresponds to CXRS measurements done on boron showing that the impurity poloidal flow in the core of AUG is non-neoclassical for a wide range of plasma parameters. Unfortunately, there is no diagnostic capable of measuring the main ion poloidal flow at AUG. From neoclassical theory it is, however, known that the impurity poloidal flow is caused due to friction with the main ions such that implications for the main ions can be gained knowing the impurity u_{pol} .

Figure 6.12a shows the theoretical poloidal rotation profiles of the plasma discharge # 32866 at 1.5 s for the main ion species deuterium and the impurity ion boron. It can be seen that the main ion poloidal rotation is in the ion diamagnetic direction in the plasma core until $\rho_{\text{tor}} = 0.7$ and in the electron diamagnetic direction at larger radii. Assuming that the drive of the impurity poloidal rotation is friction with the main ions, then the measured non-neoclassical impurity poloidal rotation indicate that the main ion poloidal rotation must be even further in the ion diamagnetic direction.

In 2013, measurements of the main ion poloidal rotation were obtained at DIII-D by measuring the complete plasma flow of impurity ions and calculating the radial electric field from the force balance equation. Together with measurements of the main ion toroidal rotation, an evaluation of the main ion poloidal rotation was possible. In a series of experiments using ECRH heating and low torque NBI input, the authors came to the conclusion that the deuterium poloidal flow exceeds the neoclassical predictions for main ion collisionalities smaller than 0.1 (see figure 6.12b)[40].

This observation is in-line with the arguments presented above. The measured non-neoclassical main ion poloidal rotation drags the impurity ion poloidal rotation as well further in the ion diamagnetic direction than predicted from neoclassical theory. Since the effect is caused from friction, the resulting difference between the measured and predicted impurity poloidal rotation is smaller than observed with measurements on the main ion species. In order to test this interpretation further, it would be necessary to experimentally measure the main ion u_{pol} at AUG.

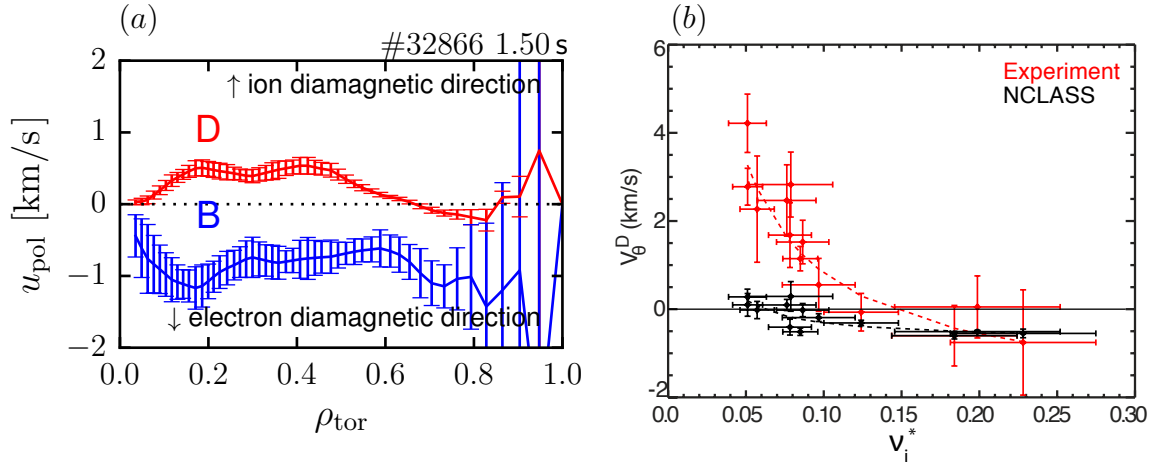


Figure 6.12: (a): Neoclassical calculation of the main and impurity ion poloidal rotation performed with NEOART. (b): Measured main ion poloidal flow at DIII-D (taken from [37]).

6.6 Conclusions

The neoclassical impurity u_{pol} depends on the gradients of n_i , T_i , and n_{imp} and has an additional dependency on the plasma collisionality through the neoclassical viscosity coefficients. By using typical plasma parameters of AUG, it was shown that the expected u_{pol} values are a few km/s.

In order to characterize the nature of the core poloidal rotation at AUG, a poloidal rotation database was built up for this Ph.D. thesis covering a wide range of the AUG parameter space. The core impurity poloidal rotation, i.e. for $\rho_{\text{tor}} < 0.6$, is found to be in the ion diamagnetic direction for both L-mode and H-mode discharges. Neoclassical theory predicts values in the electron diamagnetic direction and, therefore, non-neoclassical impurity poloidal rotation velocities are generally observed at AUG. These results are consistent with main ion poloidal rotation measurements from DIII-D. The H-mode dataset shows an increasing difference between measured and predicted u_{pol} profiles which could be linked to a combined effect of lower neoclassical damping of the poloidal rotation and a larger turbulent drive at the low collisionalities.

Chapter 7

Measurement of the $\mathbf{E} \times \mathbf{B}$ velocity across the LOC-SOC transition

(Parts of this chapter are published in: *A. Lebschy et al. NF 58 (2018) 026013 [69]*)

It was introduced in section 3.5 that L-mode tokamak plasmas with only Ohmic heating feature two main plasma regimes in terms of the energy confinement time: τ_E scales linearly with n_e up to a certain density after which it saturates. The regimes above and below the critical density are known as the linear Ohmic confinement (LOC) and saturated Ohmic confinement (SOC) regimes. The commonly accepted theory for the transition from LOC to SOC was a change in the dominant loss mechanism from electron- to ion-dominated transport implying a transition from TEM to ITG turbulence [112, 114, 116, 121, 156]. Recent modeling work from AUG suggests, however, that the saturation of τ_E is not due to a change in the dominant turbulence regime. It is rather the ion energy loss that gets stronger at higher densities due to the reduced dilution of the plasma and the stiff ion temperature profile that leads to a saturation of τ_E [120].

The indirect measurement of the poloidal rotation in the plasma core at AUG ([41] and chapter 4) is the missing ingredient to gain information on the dominant type of turbulence through the comparison of the $\vec{u}_{\vec{E} \times \vec{B}}$ from CXRS measurements and the perpendicular velocity of density fluctuations ($u_{\perp} = \vec{u}_{\vec{E} \times \vec{B}} + v_{\text{ph}}$) from turbulence propagation measurements (see section 2.3.6). The difference between the two quantities is the phase velocity of the dominant turbulence. v_{ph} is directed in the electron diamagnetic direction for TEM turbulence and in the ion diamagnetic direction for ITG turbulence.

This chapter starts with a general overview of LOC-SOC experiments performed at different devices and presents subsequently measurements of u_{pol} , u_{tor} and $\vec{u}_{\vec{E} \times \vec{B}}$ across the LOC-SOC transition and comparisons to predictions from neoclassical theory, extending previous work performed at AUG [157]. Additionally, measurements of v_{ph} are shown for a subset of the presented discharges

7.1 Overview of performed LOC-SOC experiments

Ever since the discovery of the LOC-SOC transition, an extensive study of these plasmas has been performed in order to get information on the physics and the turbulence present

in these discharges. In the following, a short overview of different experiments will be given organized as follows: experiments with indications for TEM in LOC, indications for ITG in SOC, and indications for a change from TEM to ITG are presented. A clear separation into the three categories is, however, not always possible for the mentioned experiments. Due to the large number of experiments performed during the last decades, only a small selection of experiments can be presented. It is recommended to check the references of the listed publications for further information.

Measurements of TEM in LOC

- In the early 1990's, measurements of the turbulence using coherent CO_2 laser scattering in Tore Supra showed that the level of density fluctuations in the electron diamagnetic direction followed the electron heat diffusivity, i.e. they decreased and saturated at the LOC-SOC transition. The saturation of the energy confinement time was, therefore, explained by a saturation in the electron channel. These measurements showed, additionally, that fluctuations propagated in the ion diamagnetic direction at velocities which exceed neoclassical predictions and that there is no sudden increase at the transition from LOC to SOC [119].
- The injection of modulated ECRH into a plasma allowed to get information on the TEM transport in plasma discharges [158]. Using this technique, it was shown at AUG that the propagation velocity of these heat pulses decreased strongly with increasing collisionality implying a stabilization of the TEM modes. Gyrokinetic calculations performed for these discharges suggested that the stabilization went in hand with a transition to ITG dominated transport [159].
- By cross correlating the signals of two electron cyclotron emission channels, which are separated in terms of frequency, the local electron temperature fluctuations were studied in LOC and SOC discharges at Alcator C-Mod. These measurements showed a robust reduction of the relative fluctuation level in the SOC regime compared to the LOC regime for low frequency fluctuations. Linear stability calculations for the long wavelength turbulence showed that the LOC discharges are TEM dominated and the SOC discharges ITG dominated [160].

Measurements of ITG in SOC

- Using the technique of coherent far-infrared Thomson scattering to characterize density fluctuation spectra at two discrete wavenumbers, a low frequency turbulence feature was observed at DIII-D. This feature was present in SOC, but not in the LOC regime and the onset of the fluctuations coincided with the saturation of the energy confinement time [156].
- With a far-infrared laser scattering system, the presence of density fluctuations propagating in the ion diamagnetic direction was observed at the TEXT tokamak. The onset of this feature occurs at electron densities where a clear saturation of τ_E was measured. In addition to the measurements of the fluctuations in the ion

diamagnetic direction, indications for turbulence propagating in the electron diamagnetic direction were measured in LOC and in SOC. The relative amplitude between the measured electron and ion turbulence decreased with increasing electron densities suggesting that the ion turbulence becomes eventually more important in the SOC regime [161].

Measurements of a transition from TEM to ITG

- The study of low frequency density fluctuations with a CO₂ laser scattering system and correlation techniques in the Alcator C-Mod tokamak showed that the poloidal group propagation velocity of the fluctuations is measured to be in the electron diamagnetic direction for typical densities of the LOC regime. At higher densities, the velocity is found to be in the ion diamagnetic direction [162].
- Quasi-coherent (QC) structures were measured in fluctuation spectra at Tore Supra and TEXTOR. The name originates from the characteristics that the width of the mode spectra is of the order of the dominant frequency. They appear typically at a frequency between 30 and 120 kHz. The onset of QC structures has been found during ECRH where turbulence is suspected to be driven by electron modes. Together with instability calculations, a correlation between the onsets of QC modes and TEM was found [163]. In later experiments, QC modes were found to disappear in the SOC regime [164].
- Ohmic L-mode discharges have an interesting behavior regarding the peaking of the electron density. In the beginning, an increase in the collisionality leads to a stronger peaking and later on to a decrease in the peaking. This phenomenon is related to the dominant transport mechanism. For low collisionalities, typically in the LOC regime, the transport is dominated by TEM and at higher densities, i.e. in the SOC regime, the transport is dominated by ITG [121].
- Studies of the perpendicular velocity with Doppler reflectometry at AUG showed a transition from the ion diamagnetic direction to the electron diamagnetic direction at the LOC-SOC transition. This phenomena was related to the change of the turbulent phase velocity from electron to ion diamagnetic direction prediction by linear gyrokinetic calculations [165, 166]. Measurements of the intrinsic rotation with CXRS at TCV showed later on, that the toroidal rotation switches sign from the co- to the counter-current direction [167] in these plasmas such that a possible change of v_{ph} has to be disentangled from the changing $\vec{u}_{\vec{E} \times \vec{B}}$ (see section 7.4).

This short overview shows that a significant amount of work has been done in order to characterize the dominant turbulence present in these plasmas. Most of the experiments support the commonly accepted theory that the LOC regime is TEM and the SOC regime is ITG dominated. However, in most of the cases, only plasmas deep in the LOC and deep in the SOC regime were considered and the point of the change of the dominant turbulence regime stayed unclear. Additionally, almost all experiments utilized indirect measurements of the dominant turbulence and direct evidence of a change of the dominant phase velocity is still missing.

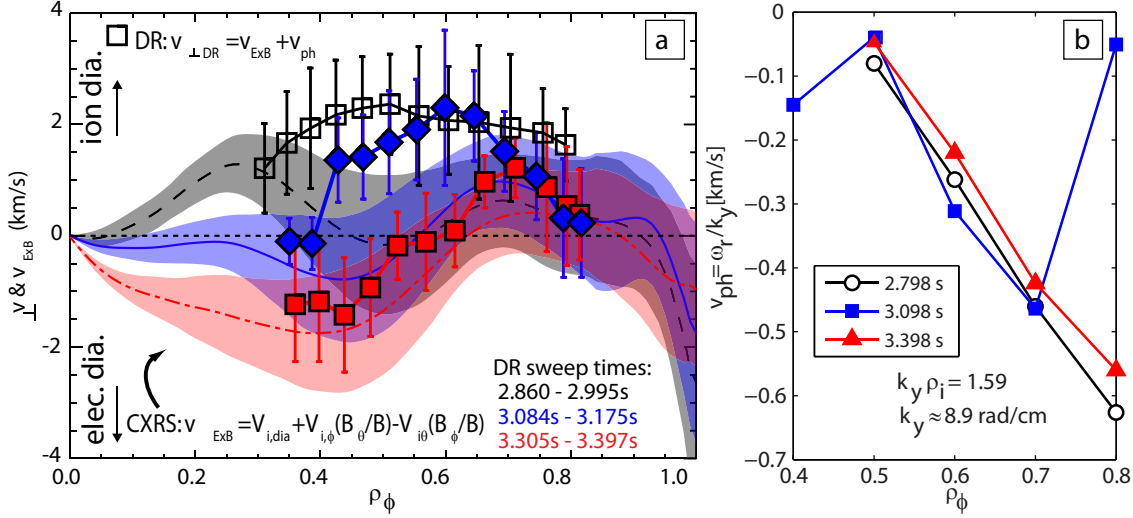


Figure 7.1: (a) Comparison of the $\vec{E} \times \vec{B}$ velocity determined with the radial force balance equation (lines) and the perpendicular rotation measured by the Doppler reflectometry (symbols). (b) Calculations of the turbulent phase velocity with linear gyrokinetic calculations at $k_{\perp} \rho_i = 1.59$, which corresponds to the turbulence size-scales measured by the Doppler reflectometry. This figure is taken from [157].

7.2 Discharge design and measurement technique

One way to gain additional information on the type of turbulence present in tokamak plasmas is to measure the turbulent phase velocity. At AUG, there are various reflectometry systems measuring the perpendicular propagation velocity of density fluctuations, which is the sum of v_{ph} and $\vec{u}_{\vec{E} \times \vec{B}}$ (see equation (2.8) and section 2.3.6). Figure 7.1a shows a recent comparison of u_{\perp} (symbols) and $\vec{u}_{\vec{E} \times \vec{B}}$ (lines) with respect to different time intervals across the LOC-SOC transition [157]. The second time interval (blue) corresponds to a measurement at the transition from LOC to SOC, while the black profile corresponds to the previous measurement interval in LOC and the red to the subsequent one in SOC. Here, the $\vec{E} \times \vec{B}$ velocity is calculated with the radial force balance equation based on CXRS measurements of u_{tor} and neoclassical prediction of u_{pol} . Qualitatively, all profiles show similar behavior, i.e. the rotation outside $\rho_{\text{tor}} = 0.7$ stays unchanged and the rotation further inside switches sign from the ion diamagnetic direction to the electron diamagnetic direction. At first glance, this could be interpreted with a turbulent phase velocity of 2 km/s in the ion diamagnetic direction. Gyrokinetic simulations (see figure 7.1b) show, however, that v_{ph} is expected to be smaller than 0.6 km/s and in the electron diamagnetic direction. With the new CXRS system installed along NBI source 8 it is now possible to measure the poloidal rotation in these plasmas with high accuracy and, therefore, to confirm if there is a non-neoclassical poloidal rotation or a turbulent phase velocity exceeding the gyrokinetic predictions.

Figure 7.2 shows the typical discharge design for the measurement of the core plasma flow across the LOC-SOC transition. The data shown here comes from the AUG dis-

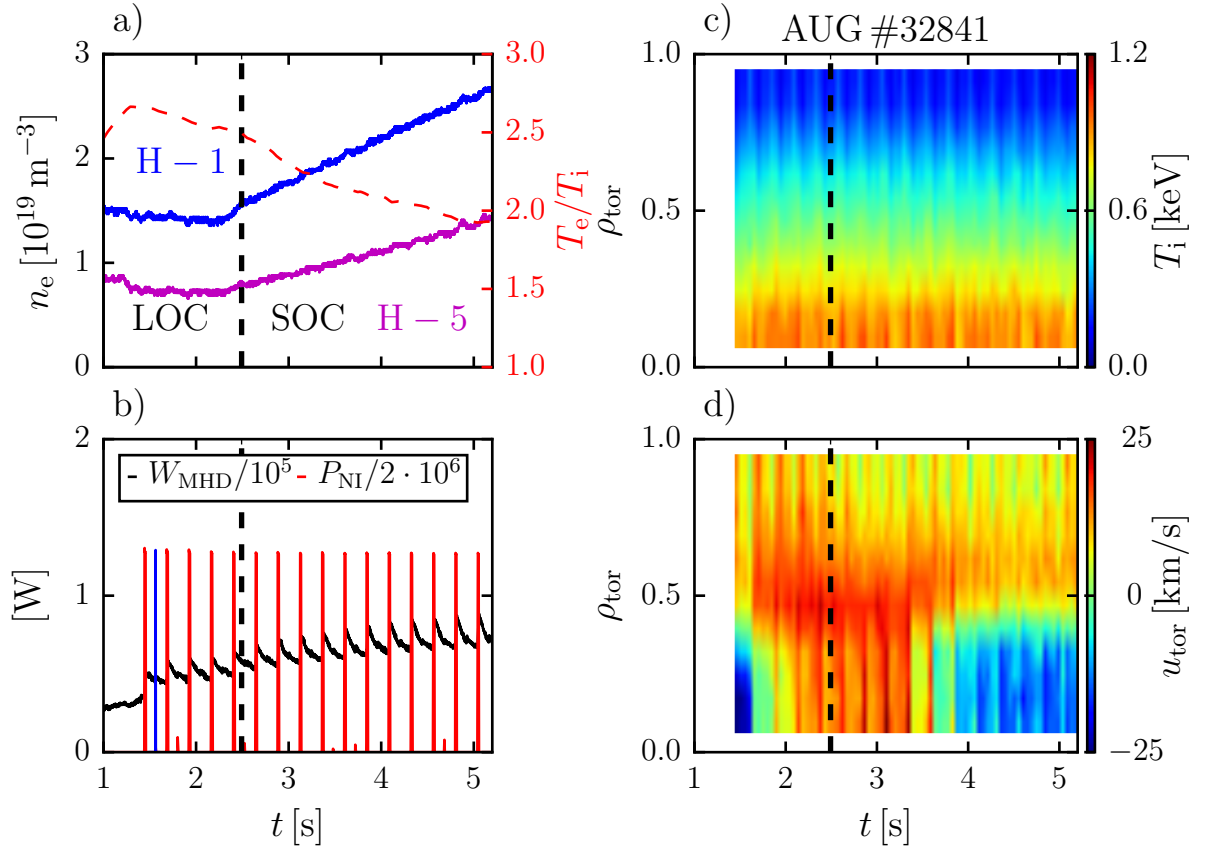


Figure 7.2: From top to bottom and left to right: time evolution of (a) the electron density for one core (blue, H – 1) and edge (magenta, H – 5) channel of the laser interferometry diagnostic as well as T_e/T_i (dashed red line), (b) the plasma stored energy (W_{MHD}) in black, the physics NBI blips in red and one of the conditioning blip occurring after each physics blip in blue, (c) contour plot of the ion temperature and (d) the toroidal rotation for a low density L-mode plasma with a density ramp. The point of the LOC-SOC transition is marked with a dashed black line.

charge # 32841. The LOC and SOC regimes are divided by a critical density, such that an intentional increase of the plasma density (see panel a) with a feedback gas puffing algorithm leads to the LOC-SOC transition. Thereby, the coupling between electrons and ions is increased leading to a decrease of T_e/T_i at higher n_e (see red dashed line in panel a). The LOC-SOC transition for the discharge shown in figure 7.2 occurs at a density of $1.6 \cdot 10^{19} \text{ m}^{-3}$ at 2.5 s (see as well figure 3.10a). This time point is marked with a vertical dashed black line in all four panels.

In order to obtain CXRS measurements in these Ohmic L-mode plasmas, a combination of fast CXRS measurements, i.e. the exposure time of the diagnostics is set to 4 ms, and the usage of NBI blips with a duration of 12–16 ms are applied [169]. It was found that the NBI source 8 does not always deliver a constant injected power across a given blip as well as from one blip to another. If the capacitors of the NBI sources are not

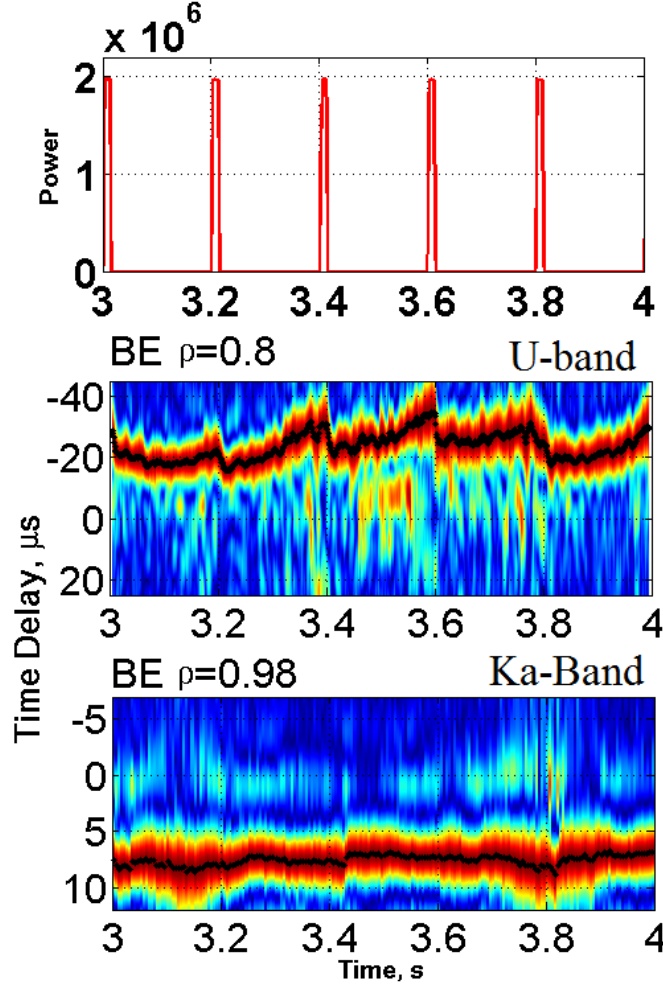


Figure 7.3: Evolution of the time delay between two antennas of the PCR diagnostic at two different radial positions (taken from [168]).

fully discharged during the blip, the next blip cannot provide a steady power. Therefore, the injection pattern of the beam blips was designed such that there is a small conditioning blip with a duration of 5 ms, which is the minimum length possible for the NBI sources, in between two physic's blips with durations of 12-16 ms. Figure 7.2e shows the injection pattern of the beam blips with the physic's blips in red and an example for one conditioning blip in blue. From panel c it can be seen that, while the conditioning blips have a very small effect on the plasma stored energy (W_{MHD}), the physic's blips lead to a strong increase of W_{MHD} . Therefore, the physic's blips are set 240 ms apart, which is roughly two energy confinement times. Since the momentum and energy confinement times are expected to be similar, the momentum impact from the NBI injection vanishes before the next physic's blip and the phases before the physic's blips can be compared for a dedicated analysis of the momentum changes in these Ohmic L-mode discharges.

One way to track the momentum evolution in the plasma from beam blip to beam blip is the time delay measurement of the poloidal correlation reflectometry diagnostic

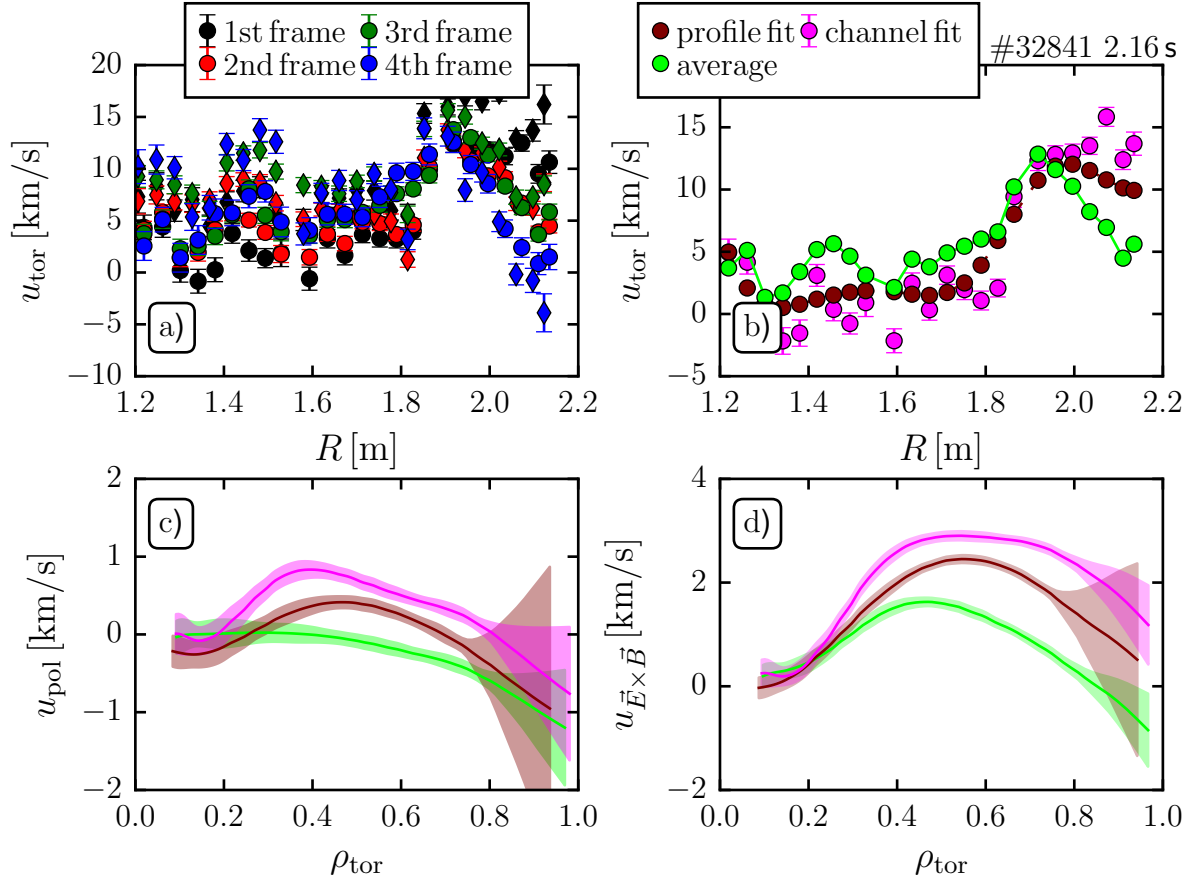


Figure 7.4: (a) Subsequent measurement frames in one beam blip (1st to 4th frame) showing the evolution of u_{tor} , (b) resulting u_{tor} profiles for different backwards extrapolation methods, (c) reconstructed u_{pol} profiles taking the average u_{tor} profile across the beam blip (green), and the two backwards extrapolation methods (profile fit: maroon; channel fit: magenta), (d) the resulting $\vec{u}_{\vec{E} \times \vec{B}}$ profiles.

which is related to the perpendicular velocity of the density fluctuation inside the plasma. Figure 7.3 shows the NBI blips and the time delay of the reflected microwave between two different receiving antennas (B and E) at two different radial locations ($\rho_{\text{pol}} = 0.8$ and 0.98). It can be seen that the perpendicular velocity, which is inversely proportional to the time delay, is not affected by the blips at $\rho_{\text{pol}} = 0.98$. Deeper inside the plasma, at $\rho_{\text{pol}} = 0.8$, the beam blip leads to a reduction of the absolute value of the time delay and, thus, to an increase in the perpendicular velocity. Before the next beam blip, the perpendicular velocity relaxes back to roughly the same values as from the blip before. Assuming that the NBI blip has mostly an impact on u_{tor} , figure 7.3 provides information on the evolution of u_{tor} in between beam blips.

As explained in the chapter 4, the usage of NBI blips enables a fairly simple determination of the active CXRS signal by subtracting off the passive signal measured in the adjacent frames to the beam blip (see section 4.1). The length of the physic's blip is typically set to 3 or 4 times the exposure time of the diagnostic. Taking into account

that it takes typically 2 ms to switch the NBI source on and off, the actual ‘on-time’ of a NBI blip with a length of 16 ms is 12 ms [157]. Special care is taken in the timing of the blips that the point at which it is switched on correlates with the beginning of a new frame of the CXRS spectrometer. Hence, only half of the first frame has active signal and the impact of the beam on the kinetic profiles is the smallest. Figure 7.4a shows the evolution of the toroidal rotation during one beam blip (1st to 4th frame). It can be seen that the changes in u_{tor} are on the order of 0 to 10 km/s. On the LFS, the NBI blip tends to decelerate the plasma and on the HFS an increase of the toroidal rotation is found. Panel b shows the comparison of two backward extrapolation methods to the average of u_{tor} across the NBI blip. The first method (‘channel fit’) takes the evolution in each CXRS channel into account and linearly extrapolates the u_{tor} measurement backwards before the beam blip. The other technique (‘profile fit’) fits each frame with a spline function and extrapolates then the profile backwards before the beam blip. It can be seen from panel b that the backwards extrapolation techniques show qualitatively and quantitatively very similar profiles, although the channel fit is a little bit more scattered. The average profile gives smaller values for u_{tor} for $R > 2.0$ m and larger values at smaller radii. Comparing the u_{pol} profiles in figure 7.4c, it can be seen that the backwards extrapolation methods give a flow in the ion diamagnetic direction at mid-radius and a flow in the electron diamagnetic direction towards the plasma edge. The poloidal rotation derived from the averaged toroidal rotation profiles gives small values in the electron diamagnetic direction. The same trend can be seen as well for the $\vec{E} \times \vec{B}$ velocity ($\vec{u}_{\vec{E} \times \vec{B}}$). For the reconstructions shown in the following, the profile backwards extrapolation method is used always since it is more stable in the reconstruction than the channel fit and gives similar profiles as this routine. Additionally, the backwards extrapolation method is believed to reproduce the kinetic profiles before the beam blip better than the average profile.

7.3 Measurement of the poloidal rotation across the LOC-SOC transition

With the indirect measurement technique presented in section 4.6.2, u_{pol} can be measured across the LOC-SOC transition. Figures 7.5a and b show, respectively, the measured ω_{tor} profiles and the reconstructed poloidal rotation during the LOC (black) and the SOC (red) phases of discharge #32841. Even though the toroidal rotation changes significantly, i.e. in the core it goes from the co- to the counter-current direction, the differences in the rotation frequency between LFS and HFS are very similar and the poloidal rotation profiles is, therefore, almost the same in LOC and SOC. In addition, the neoclassical predictions of u_{pol} from NEOART are shown in figure 7.5b with dashed lines and the same color coding. It can be seen that both the experimental (solid lines) and neoclassical (dashed lines) poloidal rotation is unchanged across the transition from LOC to SOC. The NC prediction is always in the electron diamagnetic direction and drops from nearly 1 km/s at the plasma edge to 0.5 km/s in the plasma core. Note that ‘edge’ here refers to the outermost measurement positions of the core CXRS system, but

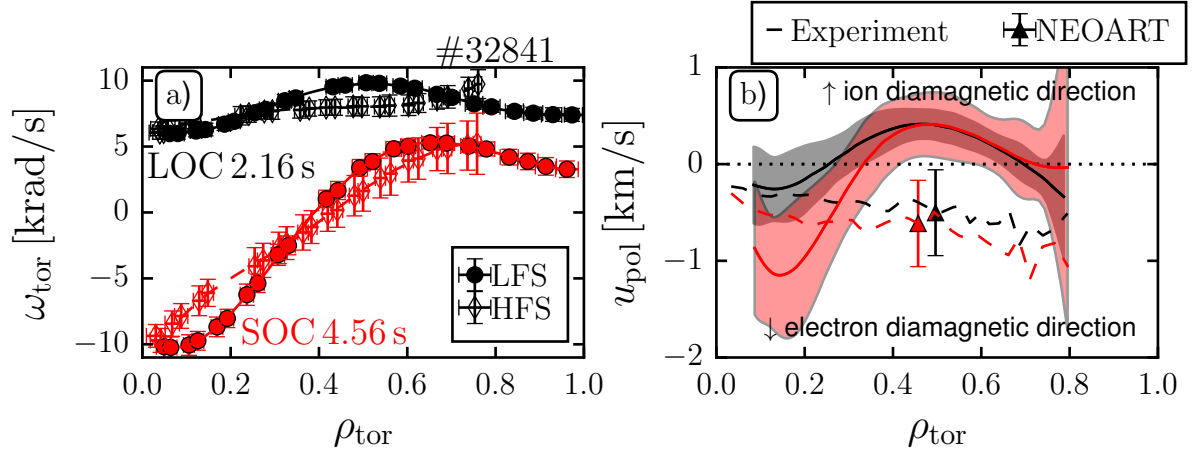


Figure 7.5: (a) Measured LFS (filled circles) and HFS (open diamonds) ω_{tor} profiles and (b) comparison of the measured u_{pol} profile (solid lines) with the neoclassical predictions (dashed lines) from NEOART for a time point in the LOC (black) and the SOC (red).

does not include the edge pedestal region. The experimental poloidal rotation, on the other hand, is in the electron diamagnetic direction only for $\rho_{\text{tor}} > 0.7$ and $\rho_{\text{tor}} < 0.3$. In this region, the agreement with NEOART is good. In between, however, u_{pol} is directed in the ion-diamagnetic direction and, therefore, non neoclassical. This measurement is in-line with previous observations presented in figure 7.1 where a discrepancy between the CXRS and Doppler reflectometry measurement at mid-radius has been found. Due to the lack of the measurement of u_{pol} in [157], the authors were not able to make a conclusion if there is a large phase velocity or poloidal flow in the ion diamagnetic direction. This measurements shows that it is a non neoclassical u_{pol} causing that difference.

In order to study the general behavior of the evolution of u_{pol} across the LOC-SOC transition, a database of Ohmic L-mode plasma discharges was build up (similar to the database presented in the previous chapter). The energy confinement time for the database is calculated from the thermal energies of ions and electrons and is fitted as a function of density with a two-line function, where the crossing point of the two lines is designated as the LOC-SOC transition. Figure 7.6 shows the neoclassical u_{pol} as a function of the experimental one for four different time intervals with respect to the LOC-SOC transition: $t - t_{\text{LS}} \in [-1 \text{ s}, -0.5 \text{ s}]$, $[-0.5 \text{ s}, 0 \text{ s}]$, $[0 \text{ s}, 0.5 \text{ s}]$ and $[0.5 \text{ s}, 1 \text{ s}]$. This figure includes data from the four discharges presented previously, comprising a scan of the plasma current from 0.6 to 1.0 MA.

The error bars shown include the statistical error from the averaging over a certain plasma region, errors in the magnetic equilibrium and the calculated measurement errors. With this method the measured data can be clustered and compared for a large quantity of shots. The radial base for the profiles in figure 7.6 is constrained to $0.3 < \rho_{\text{tor}} < 0.8$, since the error bars on the plasma current and, therefore, on the poloidal magnetic field get quite large for positions closer to the magnetic axis. The outer boundary is given by the CXRS LOS and their alignment with respect to the magnetic equilibrium. A positive sign, corresponds to a drift in the ion diamagnetic direction and a negative one to the electron diamagnetic direction.

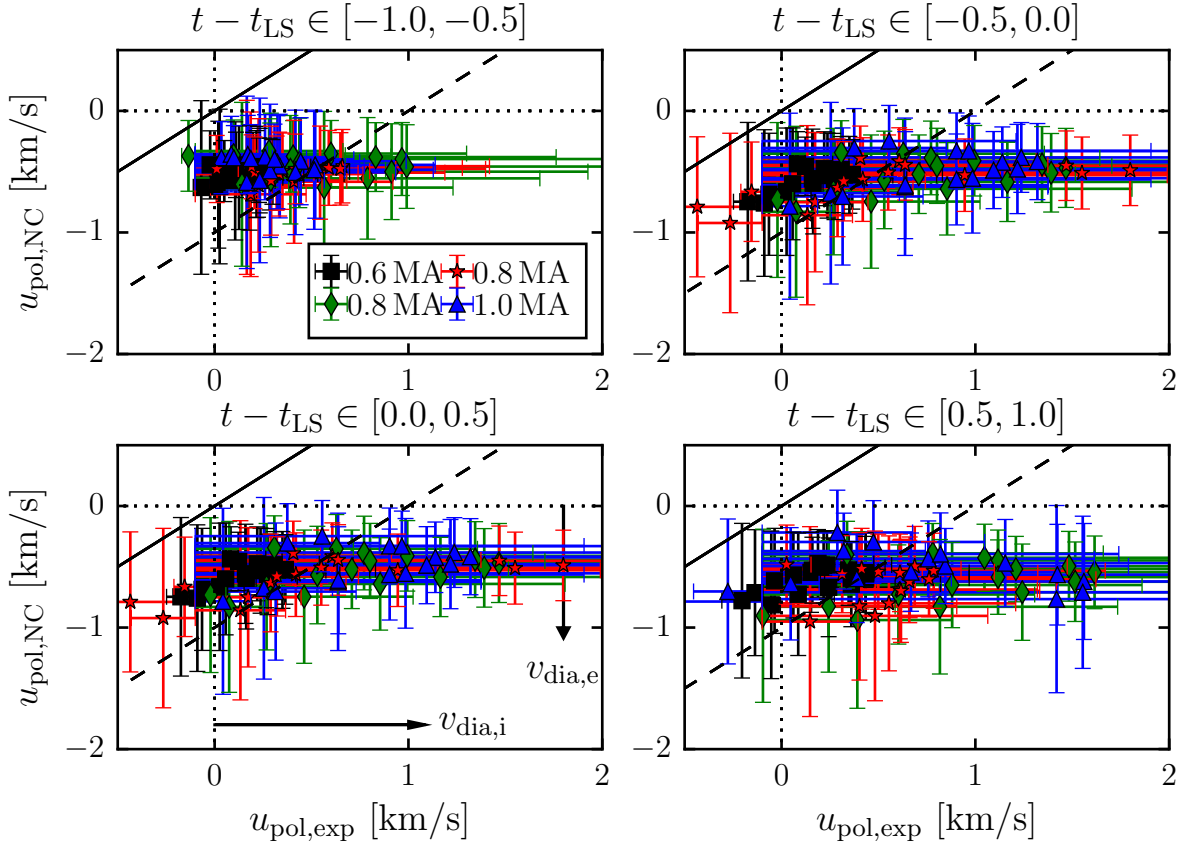


Figure 7.6: Comparison of the experimentally measured poloidal rotation to the neo-classical prediction from NEOART for different time intervals relative to the LOC-SOC transition. The solid line corresponds to the 1-1 line, i.e. a perfect agreement between measurement and theory. Additionally, a ± 1 km/s deviation from theory is shown with a dashed line.

It can be seen that the neo-classical u_{pol} profiles are in the range from -1.0 to -0.5 km/s. They are always directed in the electron diamagnetic direction and the profiles shown in figure 7.5b are a good representation of the general behavior of the neo-classical predictions. The reconstructed values from NEOART have been compared as well to reconstructions from NCLASS [103] and NEO [102] which give the same profiles for the NC poloidal rotation. For the experimental reconstructions, the range is broader (from slightly negative values to $+1.5$ km/s). For the plasma discharges at 0.8 and 1.0 MA, there seems to be a small increase of the poloidal rotation when going from LOC to SOC. This increase is, however, not outside of the error bars of the measurement such that no clear statement can be made. For all discharges and all time points a clear shift of the experimentally measured poloidal rotation in the ion diamagnetic direction is observed, i.e. the data points are shifted to the right from the 1-1 line (black line) which would correspond to a perfect agreement of measurement and NC prediction.

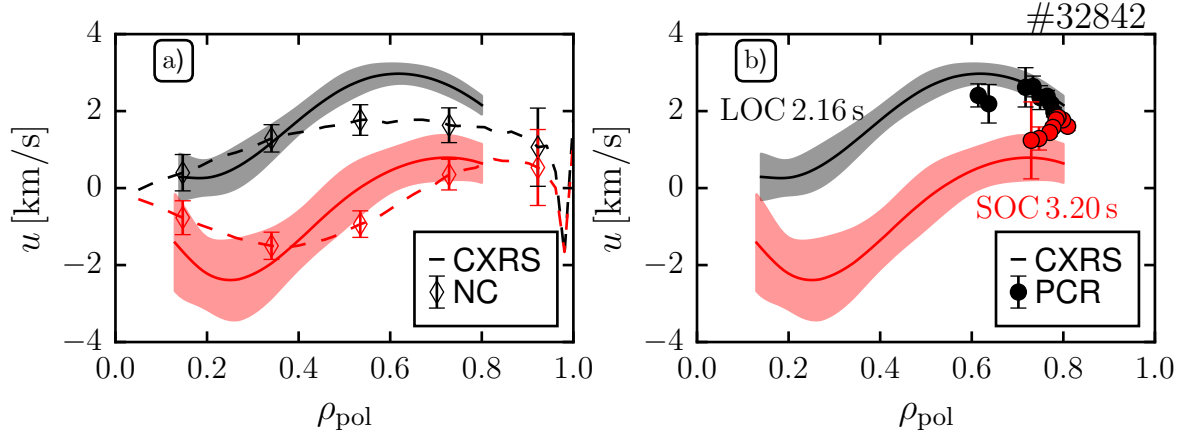


Figure 7.7: Comparison of the u_{ExB} measurement from CXRS to (solid line) to reflectometry data of u_{\perp} (dots) for both confinement regimes, the LOC (black) and SOC (red).

The increasing uncertainties of the experimental values with time relative to the LOC-SOC transition results from the increasing error bars of the HFS CXRS profiles at higher densities (see figure 7.2a) leading to stronger attenuation of the neutral beam and, thus, fewer beam neutrals on the HFS. The CXRS signal is directly proportional to $\int n_{\text{imp}} n_{0,i} dl$ along the observation direction, where $n_{0,i}$ is the neutral density of different beam components. A reduced number of neutrals on the HFS leads to a reduced signal-to-noise ratio of the CXRS signal and larger error bars on the kinetic profiles. The increased error bars for discharges at higher plasma currents results from two facts. Firstly, the LOC-SOC transition happens at higher electron densities and, thus, the error bars on the u_{tor} profiles are larger due to the stronger beam attenuation. Secondly, the difference in ω_{tor} between LFS and HFS depends on the q value. For the same u_{pol} value the difference between LFS and HFS ω_{tor} is larger for higher q and thus for smaller plasma currents ([40] and section 4.6.2). Therefore, the error bars are typically smaller for plasma discharges with lower plasma current.

7.4 Measurement of the phase velocity across the LOC-SOC transition

The knowledge of the impurity poloidal rotation enables the experimental evaluation of the radial electric field according to the radial force balance equation introduced in equation (3.7) and, therefore, the experimental measurement of $u_{\vec{E} \times \vec{B}}$. For this evaluation, the impurity density has to be calculated as well in order to evaluate the diamagnetic term. This is done with the measured line radiance of the CXRS process and the injected neutrals from the neutral beam sources measured by beam emission spectroscopy. Figure 7.7 shows a comparison of the experimentally determined $\vec{u}_{\vec{E} \times \vec{B}}$ (solid line) to the NC prediction from NEOART in panel a and to the u_{\perp} from the poloidal correlation reflectometry diagnostic in panel b. The comparison to neoclassi-

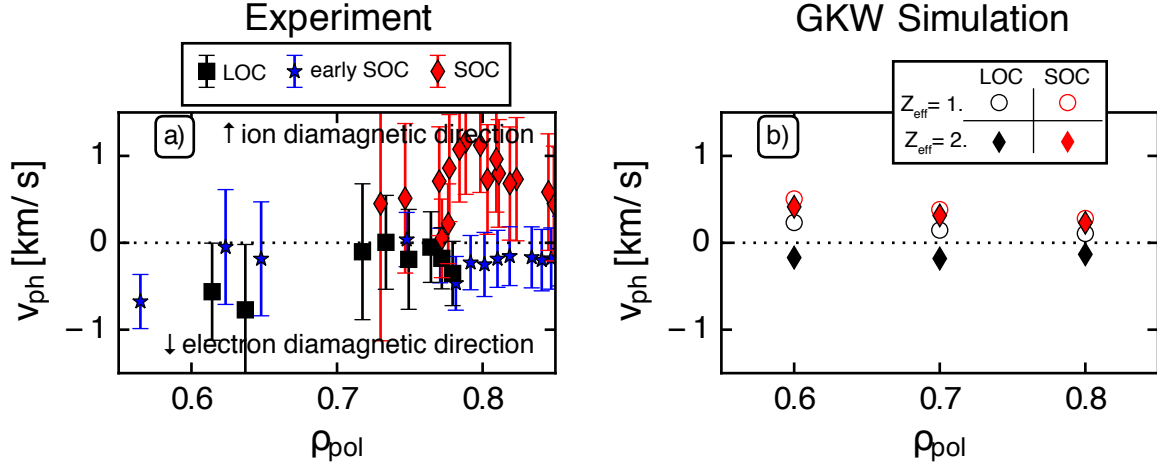


Figure 7.8: Comparison of (a) the experimentally measured turbulent phase velocity obtained by the subtraction of the perpendicular velocity and the $E \times B$ velocity in LOC (black) and SOC (red) to (b) gyrokinetic simulations of v_{ph} for two different impurity content levels.

cal gives the expected behavior. The poloidal rotation is more in the ion diamagnetic direction and the measured $\vec{u}_{\vec{E} \times \vec{B}}$ is, therefore, as well more in the ion diamagnetic direction. This comes from the fact that the measured temperature, density, and toroidal rotation profiles are taken as inputs for NEOART such that the only difference is the u_{pol} contribution. Figure 7.7b shows the measurements from the PCR diagnostic of the perpendicular velocity (filled circles). The difference between the two diagnostics should give the turbulent phase velocity according to equation (2.8): if u_{\perp} from PCR is larger or smaller than $\vec{u}_{\vec{E} \times \vec{B}}$, v_{ph} points in the ion or electron diamagnetic direction. The comparison shows that the measured values of $\vec{u}_{\vec{E} \times \vec{B}}$ from CXRS and u_{\perp} from PCR are in good agreement in LOC and in SOC. Thus, v_{ph} is small and the observed changes in the phase velocity are smaller than 0.5 km/s during the transition from LOC to SOC.

Since the observed changes in v_{ph} are close to the resolution boundary of both diagnostics, systematic changes during the LOC-SOC transition are only observable by investigating a larger number of discharges. Figure 7.8a shows the v_{ph} evaluation for in total 4 time points resulting from two different LOC-SOC transitions performed with a similar discharge design as shown in figure 7.2. At the plasma edge ($0.7 < \rho_{pol} < 0.9$) there is a systematic increase of v_{ph} , i.e. a shift towards the ion diamagnetic direction from LOC to SOC in the order of 0.5 km/s supporting the story of a change in the dominant turbulence regime across the LOC-SOC transition. The absolute values of the phase velocities in LOC and SOC are dependent on the kind of back extrapolation method used in order to extract ω_{tor} before the beam blip. The difference between the different methods is on the order of 2 km/s for u_{tor} , i.e. it will create variations in $\vec{u}_{\vec{E} \times \vec{B}}$ of 0.4 km/s. The trend that v_{ph} increases from LOC to SOC stays, however, for all reconstruction methods.

Figure 7.8b shows gyrokinetic predictions of v_{ph} from the gyrokinetic turbulence simulation code GKW [170]. The phase velocities are calculated for the most unstable mode for the same wavenumber as the PCR diagnostic is measuring. In order to test the stability of the turbulent modes, the GKW simulations have been performed for different $Z_{eff} = \sum n_i Z_i^2 / n_e$ values. $Z_{eff} = 1$ corresponds to a pure deuterium plasma and $Z_{eff} = 2$ to a boron concentration of 5%. Due to the increasing density, when going from LOC to SOC, the impurity content decreases such that the best guesses for the experimental phase velocities are the predictions for $Z_{eff} = 2$ in LOC and somewhere in between $Z_{eff} = 1$ and 2 for SOC. The absolute change in v_{ph} is roughly a factor of 2 higher in the experiment compared to the simulations. From figure 7.8b it can be seen that the direction of the phase velocity (that is the dominant mode) is sensitive to the impurity content of the plasma. The main effect of an increased impurity content is the dilution of the main ions leading to a reduction of the ITG growth rate and a broadening of the domain of dominant TEM instabilities.

7.5 Reversal of the core toroidal rotation

Ohmic L-mode discharges feature another interesting phenomenon: the intrinsic core toroidal is observed to spontaneously reverse from the co- to the counter-current direction when the electron density is increased. In this work, intrinsic rotation refers to the toroidal rotation of the plasma established in the absence of externally applied torque. The rotation reversal was observed first at TCV [167] and since then also at Alcator C-Mod [171], AUG [157, 172], KSTAR [173], and MAST [174] and is in-line with AUG Doppler reflectometry measurements across the LOC-SOC transition [165].

In [157, 172] the behavior of the intrinsic rotation was observed in AUG for a large number of Ohmic L-mode plasmas. The rotation measurements in this database, however, were made with CXRS diagnostics with lower light throughput and lower radial resolution than the diagnostics presented in chapter 4. As a result, the uncertainties on the measured profiles were often several km/s, which is 2 to 3 times larger than what is achievable with the newly installed CXRS diagnostics. Moreover, the previous analysis relied heavily on electron density profiles measurements, which have been significantly improved. These facts motivated a revisit of the intrinsic rotation in Ohmic L-mode discharges and a comparison to the previous analysis and results.

Figure 7.9a shows the evolution of the rotation gradient $u' = -(R^2/v_{thi,i}) d\omega/dr$ at a radial position of $\rho_{tor} = 0.65$. Here, $v_{thi,i}$ is the main ion thermal velocity $v_{thi,i} = \sqrt{2T_i/m_i}$. Additionally, the Mach number M and the normalized logarithmic electron density gradient length $R/L_{ne} = R(\nabla_r n_e)/n_e$ are shown in panels b and c. All quantities are shown as a function of the effective collisionality ν_{eff} which is given by:

$$\nu_{eff} = 0.00279 \cdot \left(15.94 - 0.5 \log \frac{n_e}{T_e} \right) \cdot \frac{n_e}{T_e^2} R \sqrt{m_A} Z_{eff}, \quad (7.1)$$

where the electron density is given in 10^{19} m^{-3} , T_e in keV, R in m, and the mass of the main ion species m_A in amu, i.e. $m_A = 2$. The beginning of the discharges which feature

counter-current directed toroidal rotation are intentionally omitted in this figure. This phase is transient and cannot be maintained by holding all controlled plasma variables constant. However, it is worth noting that these data points also show the same dominant parameter trends as observed in the plasma flat top under steady conditions, namely R/L_{n_e} and ν_{eff} . The dependency on R/L_{T_e} and R/L_{T_i} is observed to be weaker than previously observed [175].

Similar to previous work, the effective collisionality is a good variable to describe the data. In this parametrization, the different densities of the LOC-SOC transition and the rotation reversal collapse to one. In contrast to the previous work, however, there is a clear time delay between the reversal of the core toroidal rotation and the LOC-SOC transition (see figure 7.9b). The electron density peaking in figure 7.9c is as well less pronounced compared to previous work. However, a strong correlation between these parameters is still observed consistent with previous results.

To illustrate the sequence of events observed in these plasmas the collisionalities at which phase velocities in the ion diamagnetic direction are measured are additionally shown in figure 7.9 with vertically dashed lines. Here one can see that as the collisionality is increased first a LOC-SOC transition is observed (gray area), which is a global phenomenon in the energy confinement time. Subsequently, the core toroidal rotation reverses from the co- to the counter-current direction concomitant with an increase in R/L_{n_e} . Finally, phase velocities in the ion diamagnetic direction are measured in the edge region of the plasma. The peaking of the electron density profile at mid-radius is expected to happen while the dominant turbulence mode at this location is still TEM, but near the TEM-ITG transition [176]. The edge measurements at this time point indicate that there is already an ion-directed turbulence propagation, which supports previous indications that the transition occurs first at the plasma edge and then propagates inwards [159].

7.6 Summary

Measurements in Ohmic L-mode discharges show that the impurity poloidal rotation is directed in the ion diamagnetic direction at mid-radius, which is in the opposite direction as predicted from neoclassical theory. This quantity is the missing ingredient to evaluate the core $\vec{E} \times \vec{B}$ velocity. A comparison with the perpendicular flow velocity enables an evaluation of the turbulent phase velocity at different points in the LOC-SOC evolution. An increase in the ion diamagnetic direction is observed at the plasma edge ($\rho_{\text{pol}} > 0.8$) consistent with a change in the plasma turbulence towards a more ITG dominated regime in this region. The gathered data suggests that the change in v_{ph} is not connected to the LOC-SOC transition, but occurs in the SOC regime.

The upgrade of the core CXRS systems provided, additionally, a significant reduction of the error bars for the intrinsic rotation measurement and lead to new insights compared to previous observations. With the availability of v_{ph} measurements in these discharge it was possible to experimentally measure the sequence of events in these Ohmic L-mode discharges. The gathered data suggests that there first the LOC-SOC transition, which is followed by a change in the direction of the core intrinsic toroidal rotation from co- to counter-current direction. The core rotation change is accompanied by a peaking of the core electron density and lastly the edge phase velocity changes sign.

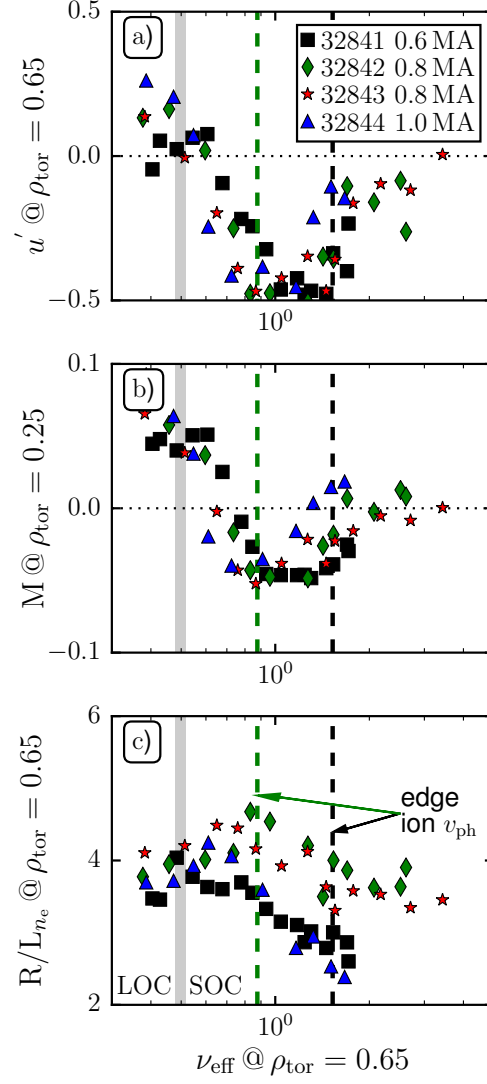


Figure 7.9: Evolution of the rotation gradient (a), Mach number (b), and normalized gradient length of the electron density (c) as a function of effective collisionality for four different plasma discharges at different plasma currents (0.6 MA: 32841 with black squares; 0.8 MA: 32842 with green diamonds, 32843 with red stars; and 1.0 MA: 32844 with blue triangles) at the radial position $\rho_{\text{tor}} = 0.65$. The LOC-SOC transitions for the different discharges are marked with a gray area. The vertical dashed lines correspond to the collisionalities at which phase velocities in the ion diamagnetic direction were measured.

Chapter 8

Summary and outlook

The radial electric field is an important parameter in fusion plasmas due to its strong impact on turbulence and turbulent transport. It can be determined experimentally from the radial force balance equation where all plasma quantities, i.e. the diamagnetic term and the flow of the particles, can be measured with charge exchange recombination spectroscopy. The toroidal rotation in tokamaks is a free parameter that is usually dominated by external momentum input from the NBI sources. The poloidal rotation, on the other hand, is strongly damped due to the magnetic pumping effect and neoclassical theory predicts values in the range of 0.5 to 2.0 km/s in the electron diamagnetic direction for low- Z impurities.

CXRS exploits the line radiation from charge exchange processes between fully stripped impurity ions inside the plasma and neutrals injected from the NBI sources and is a common technique to measure the plasma flow in tokamaks. At the values predicted from theory, the Doppler shift due to the poloidal rotation of the line radiation is only a fraction of the thermal line broadening. Additionally, corrections that are at least of the same order as the measured u_{pol} values are necessary such that the direct observation is challenging. An accurate measurement of u_{pol} is, however, necessary to test the basic understanding of the flow generation in tokamaks.

Under the assumption that the plasma flow is divergence free, any plasma flow can be expressed by a component parallel to the magnetic field and a rigid body rotation in the toroidal direction. By measuring u_{tor} on the LFS and HFS of the plasma, the components of the general plasma flow can be evaluated giving an indirect measurement of the poloidal rotation. The knowledge of both the u_{tor} and u_{pol} velocities and the impurity density profiles allows the calculation the radial electric field. From this, the local $\vec{E} \times \vec{B}$ drift can be determined from CXRS measurements.

For this Ph.D. thesis, a new core CXRS system was installed at AUG providing CXRS measurements with 70 LOSs from the LFS pedestal top to the HFS pedestal top and, thus, enabling the measurement of the complete flow in the plasma core. In the following, the most important results from this thesis are summarized.

Previous direct measurements of the core poloidal rotation resulted in values with errors larger than the predicted values from NC theory and often it was even impossible to unambiguously deduce the direction of the poloidal rotation. Chapter 5 showed that

the indirect measurement technique provides the core u_{pol} with uncertainties in the range of 0.5 to 1 km/s such that the direction of the poloidal rotation can be reconstructed unambiguously. A careful analysis of systematic errors from the magnetic equilibrium, the calibration of the CXRS systems, and from the reconstruction technique was performed and the resulting errors were found to be smaller than 300 m/s, which is significantly improved compared to previous direct measurements.

An impurity density asymmetry was reported in the edge region between HFS and LFS at the AUG and Alcator C-Mod tokamaks. With the new core CXRS system a precise measurement of the n_{imp} inside the plasma is possible. It was measured in L-mode discharges that there is in general no impurity density asymmetry. Due to the measurements technique, the statement relates to L-mode discharges with NBI blips at full power. In H-mode discharges, however, the n_{imp} asymmetry is a common observation. The onset of the asymmetry seems to vary with the applied heating power such that an increase in the NBI heating leads to a movement of the onset to smaller radii. The onset was never observed at radii smaller than $\rho_{\text{pol}} = 0.6$.

The neoclassical poloidal rotation values for impurities depends on the gradients in n_i , T_i , and n_{imp} and has an additional dependency on the plasma collisionality through the viscosity coefficients. A parameter study with a set of input profiles for n_i , T_i , and n_{imp} covering the experimental space of AUG shows that the poloidal rotation is expected to be a few km/s at AUG.

In order to characterize the nature of u_{pol} at AUG, a database was built up covering a wide range of the AUG operating space. This database includes as well neoclassical predictions from different codes, namely NEO, NCLASS and NEOART. A comparison between the predictions of these codes shows a good agreement. In the database the neoclassical predictions for u_{pol} are between 0 and 1.5 km/s in the electron diamagnetic direction.

At AUG, the poloidal rotation velocities at mid-radius are found to be more ion diamagnetic directed than the neoclassical prediction in both L-mode and H-mode discharges. At the plasma edge, u_{pol} is found to be electron diamagnetic directed and in good agreement with NC codes which is consistent with previous investigations at AUG. In order to characterize the core u_{pol} further at AUG, different parameter dependencies were investigated in the framework of the database. No clear correlation with the normalized electron density gradient length and the normalized ion temperature gradient length was found. In the H-mode data there is an increase in the difference between experimentally measured and theoretically predicted u_{pol} values for smaller collisionalities concomitant with larger normalized Larmor radius values. A possible explanation for this result is a balance between the neoclassical damping and the turbulent drive of u_{pol} . Within this paradigm, the dominant driving mechanism for u_{pol} is, therefore, the turbulence for the smallest collisionalities, which feature the largest normalized Larmor radii of the database. For higher collisionalities, the turbulent drive is reduced and the experimental profiles agree with the neoclassical predictions within their uncertainty.

Similar to the H-mode case in Ohmically heated L-mode plasmas the core u_{pol} is observed to be in the ion diamagnetic direction at mid-radius and non neoclassical. These non neoclassical rotations help to explain previous comparisons of CXRS and Doppler

reflectometry data at AUG [157]. The poloidal rotation switches direction outside of $\rho_{\text{tor}} > 0.7$ and reaches similar values as predicted from NC theory.

These plasma discharges feature a large variety of interesting observations, for example the saturation of the energy confinement time. At low electron densities τ_E is observed to increase linearly with n_e defining the linear Ohmic confinement regime. Above a certain critical density, τ_E saturates giving the saturated Ohmic confinement regime. Additionally, the core toroidal rotation reverses from the co- to the counter-current direction, which will be known as ‘rotation reversal’. Due to the indirect measurement of the core u_{pol} , it is possible to evaluate the core $\vec{E} \times \vec{B}$ velocity and get more insights on the turbulent phase velocity through comparisons with turbulence propagation measurements at different points in the LOC-SOC evolution. An increase in the ion diamagnetic direction is observed at the plasma edge ($\rho_{\text{pol}} > 0.8$) consistent with a change in the plasma turbulence towards a more ITG dominated regime in this region. The measurements suggest that the change in v_{ph} is not connected to the LOC-SOC transition, but occurs at some point in the SOC regime.

Additionally, the new core CXRS systems provides a significant reduction of the error bars for the intrinsic rotation measurement and lead to new insights compared to previous observations. Similar dominant parameters for the rotation reversal were found as in previous work, i.e. R/L_{n_e} and ν_{eff} . With the availability of v_{ph} measurements in these discharges it was possible to experimentally measure the sequence of events in these Ohmic L-mode discharges. The gathered data suggests that first the LOC-SOC transition, which is followed by a change in the direction of the core intrinsic toroidal rotation from co- to counter-current direction. The core rotation change is accompanied by a peaking of the core electron density and lastly the edge phase velocity changes sign.

Outlook

In this Ph.D. thesis, the most important result is the non neoclassical poloidal rotation in the plasma core. There is further analysis necessary to derive driving mechanisms of this non-neoclassical poloidal rotation. A very interesting candidate is a turbulence drive of u_{pol} . In order to test this hypothesis further experiments with dedicated density fluctuation measurements are necessary in order to check if the Reynolds stress of the turbulence is a possible explanation to explain the non neoclassical poloidal rotations.

Furthermore, the indirect measurement technique provides a very accurate and reliable measurement of the complete core plasma flow and offers the possibility to evaluate the experimental core E_r on a regular basis, which is a crucial parameter for further investigations of the core transport. With this technique, further phenomena like transport changes during sawteeth and the formation of an internal transport barriers can be investigated.

Acknowledgments

This work is the result of the ideas and effort of many people. I would like to extend my sincerest gratitude and appreciation to those who have supported me throughout this dissertation. I would not have gone this far without the help of the people.

- First of all, I would like to thank my supervisor Dr. Rachael McDermott. She has guided me throughout the thesis and strengthened always my back. I am sincerely grateful for her limitless support, the helpful insights and discussions. Her door was always open and I came out of her office with a number of new ideas, smarter and more motivated. I would like to thank her especially in supporting me to find the right sign of the poloidal rotation (various times).
- I also want to extend my thanks to my academic supervisor Prof. Dr. Ulrich Stroth for giving me the opportunity to do this dissertation at the Max-Planck-Institute für Plasmaphysik and the helpful discussions about my work.
- For the help in interpreting and preparing experiments and for the time to discuss the results of my work, I am sincerely grateful to Dr. Clemente Angioni, Dr. Ralph Dux, Dr. Thomas Pütterich and Dr. Francois Ryter.
- I would like to thank the whole spectroscopy group, especially Dr. Ralph Dux, Dr. Rachael McDermott, Dr. Benedikt Geiger, Dr. Athina Kappatou, Dr. Marco Cavedon, Cecilia Bruhn and Ulrike Plank for the great help in the day to day calibration work and in helping me to understand how visible spectroscopy works.
- I am grateful to Dr. Gerrard Conway, Dr. Tim Happel, Dr. Dmitrii Prisiazhniuk, and Dr. Anna Medvedeva for introducing me into the principles of reflectometry and providing high quality data of turbulence measurements.
- I would like to extend my appreciation to Dr. Rainer Fischer, Dr. Emiliano Fable, Dr. Patrick McCarthy, Dr. Matthias Willensdorfer, Severin Denk, and Ivan Erofeev for their input and contributions to my work. I want to extend my thanks to the whole ADSEX Upgrade team with the amazing support in the control room and the fact that everyone takes the time to discuss and help with stuff.
- All our work would not be possible without the enthusiasm of the technicians who try to realize every crazy idea. My special thanks goes to Michael Ebner, Michael Rolffs, Wolfgang Zeidner, and all the Gefäßmannschaft. I would like to thank Roland Merkel, Karl Behler, Sven Martinov, and Annedore Buhler for the amazing IT-Support.

- I would like to thank especially Dr. Marco Cavedon, Dr. Florian Laggner, Dr. Alexander Bock, and David Rittich for the unforgettable time at various conferences, HEPP and Ringberg seminars, and at the IPP in general. I want to extend the thank to my office mates Dr. Dmitrii Prisiazhniuk, Dr. Anna Medvedeva, Ulrike Plank, and Georg Harrer as well as Dr. Benedikt Geiger, Dr. Eleonora Viezzer, Dr. Mike Dunne, Dr. Ian Faust, Dr. Thomas Pütterich, Dr. Matthias Willensdorfer, Georg Holzner, Bernhard Schießl, and Branka Vanovac. They helped me always with questions and had time for a relaxed chat, to play darts, to commute by bike and to go running. Additionally, I would like to thank Dr. Matthias Bernert and Dr. Athina Kappatou for their generous supply of chocolate.
- Beyond the already mentioned persons, I would like to extend my thanks to Dr. Andreas Burckhart, Dr. Matthias Bernert, Dr. Sina Fietz, Dr. Hauke Doerk, Dr. Philip Schneider, Dr. Steffen Potzel, Dr. Markus Weiland, Dr. Felix Reimold, Felician Mink, Michael Griener, Javier Pinzon, Dr. Dominik Brida, Dr. Michael Faitsch, Dr. Livia Casali, Luis Guimerais, Dr. Christian Vorpahl and Dr. Gregor Birkenmaier for all the support, the friendship and the very nice last years. Moreover, I want to apologize to all those who I forgot to mention in these Acknowledgments.
- Finally, I would like to thank all my friends and especially my family for their support and patience.

Acronyms

A	atomic mass number. 1
ADC	analog-to-digital conversion. 50
Ar	argon. 42
AUG	ASDEX Upgrade. iii, 8
B	boron. 42
BES	beam emission spectroscopy. 72
B_{pol}	poloidal magnetic field. 9, 11
B_{tor}	toroidal magnetic field. 9, 70
C	carbon. 42
CCD	charge coupled device. 18
CX	charge exchange. 41
CXRS	charge exchange recombination spectroscopy. iii, 7
D	deuterium. 2
DCN	deuterium cyanide laser. 13, 14
DR	Doppler reflectometry. 15
$\Delta E/A$	binding energy per nucleon. 1
ECE	electron cyclotron emission. 13
ECRH	electron cyclotron resonance heating. 11
E_r	radial electric field. 7
ETG	electron temperature gradient. 29
ω_{tor}	toroidal rotation frequency. 67
H	hydrogen. 2
He	helium. 2
HFS	high-field side. iii, 6
I_p	plasma current. 7
ICRH	ion cyclotron resonance heating. 11
IDA	integrated data analysis. 13
IDE	integrated data analysis equilibrium. 18

iMSE	imaging motional Stark effect. 69
ITB	internal transport barrier. 8
ITG	ion temperature gradient. iv, 29
Kr	krypton. 42
LFS	low-field side. iii, 6
Li	lithium. 3
LIB	Li-beam. 14
LOC	linear Ohmic confinement. iii, 8
LOS	line-of-sight. iii, 8
LSN	lower single null. 75
MHD	magneto-hydrodynamics. 5
MSE	motional Stark effect. 18
N	nitrogen. 42
n	neutron. 1
n_e	electron density. 13
n	plasma density. 3
n_i	main ion density. 80
n_{imp}	impurity density. 33
NBI	neutral beam injection. 6
NC	neoclassical. iii, 26
Ne	neon. 42
p	proton. 1
PCR	poloidal correlation reflectometry. 15
W_{MHD}	plasma stored energy. 100
POL	polarimetry. 69
ROI	region of interest. 46
SOC	saturated Ohmic confinement. iii, 8
SOL	scrape-off-layer. 44
T	tritium. 2
T_e	electron temperature. 13
T	plasma temperature. 3
T_i	ion temperature. 67
τ_E	energy confinement time. 3
TEM	trapped electron mode. iv, 29
TF	toroidal field. 9
TS	Thomson scattering. 14
USN	upper single null. 75

$\vec{u}_{\vec{E} \times \vec{B}}$	$\vec{E} \times \vec{B}$ velocity. 101, 106
u_{\perp}	perpendicular plasma flow velocity. iii, 15, 31
v_{ph}	turbulent phase velocity. iii
u_{pol}	poloidal rotation. iii, 6
u_{tor}	toroidal rotation. iii, 6

Symbolslist

Sign	Description	Unit
I_p	plasma current	A
n	plasma density	m^{-3}
n_e	electron density	m^{-3}
n_{imp}	impurity density	m^{-3}
n_i	ion density	m^{-3}
E_r	radial electric field	V m^{-1}
B_{pol}	poloidal magnetic field (also denoted as B_θ)	T
B_{tor}	toroidal magnetic field (also denoted as B_ϕ)	T
ω_{tor}	toroidal rotation frequency	krad s^{-1}
R	major radius	m
ρ_{pol}	normalized poloidal flux co- ordinate	
ρ_{tor}	normalized toroidal flux co- ordinate	
T_e	electron temperature	eV
T_i	ion temperature	eV
T	plasma temperature	eV
τ_E	energy confinement time	s
$\vec{u}_{\vec{E} \times \vec{B}}$	$\vec{u}_{\vec{E} \times \vec{B}}$ velocity	m s^{-1}
u_\perp	perpendicular velocity	m s^{-1}
u_{pol}	u_{pol} velocity	m s^{-1}
u_{tor}	u_{tor} velocity	m s^{-1}

Glossary

Alcator C-Mod	It is the third of the Alcator (Alto Campo Toro, High Field Torus) series located at the Massachusetts Institute of Technology. iii, 71
ASDEX	Axially Symmetric Divertor Experiment. This tokamak is the predecessor of ASDEX Upgrade and was located in Garching b. München. iii, 8
DIII-D	The Doublet III-D tokamak is located in San Diego, California, USA. iii, 8
EQH	This equilibrium reconstruction done with CLISTE provides a high temporal resolution of 1 ms. 18
EQI	This equilibrium reconstruction is based on the measurements from magnetic pickup coils at ASDEX Upgrade and provides magnetic equilibria with a temporal resolution of 100 ms. 18
FT	The Frascati Tokamak is located in Italy.. 37
FTU	The abbreviation is short for Frascati Tokamak Upgrade. It is the successor of the FT tokamak. 37
ISX-A	Impurity Study Experiment. 37
ITER	The International Thermonuclear Experimental Reactor (ITER) is an international fusion experiment that is currently built in Cadarache, France. 5
JET	Joint European Torus. 4
NCLASS	The reference [103] gives a brief overview of the principles of this neoclassical code. 83

NEO	Details to this neoclassical code can be found in [102]. 83
NEOART	A neoclassical code to estimate the predictions for the poloidal rotation. Details can be found in [101]. 68
PDX	The Poloidal Divertor Experiment was located at the Princeton Plasma Physics Laboratory, USA. 8
TCV	The Tokamak à Configuracion Variable is located in Lausanne, Switzerland. iii, 8
TEXT	The Texas Experimental Tokamak provided plasmas with a 1 m major radius. 96
TEXTOR	The Tokamak Experiment for Technology Oriented Research was operated at the Forschungszentrum Jülich from 1963 to 2013. 97
tokamak	The name is a transliteration of the Russian word tokamak (toroidal'naya kamera s magnitnymi katushkami) — toroidal chamber with magnetic coils. 4
Tokamak-3	Tokamak in Russia. 36
Tore Supra	A tokamak located in France. 37

Bibliography

- [1] International Energy Agency (IEA): Energy Statistics Division 09/2015, Key World Energy Statistics 2010, © OECD/IEA. <http://www.bpb.de/>.
- [2] F. Birol *et al.* *Energy and Climate Change - World Outlook Special Report*. Ed. by R. Priddle. International Energy Agency (IEA), 2015.
- [3] CAIT Climate Data Explorer. 2015. Washington, DC: World Resources Institute. Available online at: <http://cait.wri.org>.
- [4] Dr. Pieter Tans, NOAA/ESRL (<http://www.esrl.noaa.gov/gmd/ccgg/trends/>) and Dr. Ralph Keeling, Scripps Institution of Oceanography (<http://scrippsco2.ucsd.edu/>).
- [5] G. Audi and A. Wapstra. “The 1995 update to the atomic mass evaluation”. *Nuclear Physics A* **595** (1995) 409–480. ISSN: 0375-9474.
- [6] H.-S. Bosch and G. Hale. “Improved formulas for fusion cross-sections and thermal reactivities”. *Nuclear Fusion* **32** (1992) 611.
- [7] World Nuclear Association, *Outline History of Nuclear Energy*, <http://www.world-nuclear.org/information-library/current-and-future-generation/outline-history-of-nuclear-energy.aspx>, visited 23rd April 2016 15:00.
- [8] E. Rutherford. “LI. Collision of α particles with light atoms I. Hydrogen”. *Philosophical Magazine Series 6* **37** (1919) 537–561.
- [9] A. S. Eddington. “The Internal Constitution of the Stars”. *Nature* **106** (1920) 14–20.
- [10] K. R. Lang. *Astrophysical formulae: a compendium for the physicist and astrophysicist*. 2nd. Berlin: Springer, 1980.
- [11] U. Schumacher. *Fusionsforschung*. English. Eine Einführung. Darmstadt: Wissenschaftliche Buchgesellschaft, 1993. ISBN: 9783534109050.
- [12] J. D. Lawson. “Some Criteria for a Power Producing Thermonuclear Reactor”. *Proceedings of the Physical Society. Section B* **70** (1957) 6.
- [13] J. Nuckolls *et al.* “Laser Compression of Matter to Super-High Densities: Thermonuclear (CTR) Applications”. *Nature* **239** (1972) 139–142.
- [14] R. Dux. *Plasmaphysik und Fusionsforschung- Teil II: Fusionsforschung*. Skript zur Vorlesung. Universität Augsburg, SoSe 2002.

- [15] H. S. Bosch *et al.* “Construction of Wendelstein 7-X - Engineering a steady state stellarator”. *2009 23rd IEEE/NPSS Symposium on Fusion Engineering*. 2009, pp. 1–7.
- [16] U. Stroth. *Plasmaphysik*. German. Phänomene, Grundlagen, Anwendungen. Wiesbaden: Springer, 2011. ISBN: 9783834816153.
- [17] L. Spitzer Jr. *A proposed stellarator*. Report No. NYO-993 (PM-S-1). US Atomic Energy Commission Report, 1951.
- [18] A. D. Sakharov. *Teoriya magnitnogo termoyadernogo reaktora (The theory of magnetic thermonuclear reactor) Pt. II*. Vol. 1. 1958, p. 20.
- [19] B. D. Bondarenko. “Role played by O A Lavrent’ev in the formulation of the problem and the initiation of research into controlled nuclear fusion in the USSR”. *Physics-Uspekhi* **44** (2001) 844.
- [20] Max-Planck-Institut für Plasmaphysik. *Ignition conditions*. <http://www.ipp.mpg.de/15144/zuendbedingungen> (visited 13.06.2017).
- [21] J. Jacquinot and the JET team. “Deuterium-tritium operation in magnetic confinement experiments: results and underlying physics”. *Plasma Physics and Controlled Fusion* **41** (1999) A13.
- [22] ITER Engineering Design Activities (EDA). *Summary of the ITER final design report*. Documentation Series No. 22 IAEA/ITEREDA/DS/22. International Atomic Energy Agency, 2001.
- [23] T. H. Stix. “Decay of poloidal rotation in a tokamak plasma”. *Physics of Fluids* **16** (1973) 1260–1267.
- [24] J. M. Dawson and M. F. Uman. “Heating a plasma by means of magnetic pumping”. *Nuclear Fusion* **5** (1965) 242.
- [25] M. W. Kissick *et al.* “Poloidal rotation effects on a simulated resistive kink mode”. *Physics of Plasmas* **8** (2001) 174–179.
- [26] R. Betti and J. P. Freidberg. “Radial discontinuities in tokamak magnetohydrodynamic equilibria with poloidal flow”. *Physics of Plasmas* **7** (2000) 2439–2448.
- [27] G. Dif-Pradalier *et al.* “Interplay between Gyrokinetic Turbulence, Flows, and Collisions: Perspectives on Transport and Poloidal Rotation”. *Phys. Rev. Lett.* **103** (2009) 065002.
- [28] R. E. Bell and E. J. Synakowski. “New understanding of poloidal rotation measurements in a tokamak plasma”. *AIP Conference Proceedings* **547** (2000) 39–52.
- [29] A. R. Field *et al.* “Comparison of measured poloidal rotation in MAST spherical tokamak plasmas with neo-classical predictions”. *Plasma Physics and Controlled Fusion* **51** (2009) 105002.
- [30] R. E. Bell *et al.* “Comparison of poloidal velocity measurements to neo-classical theory on the National Spherical Torus Experimenta)”. *Physics of Plasmas* **17** (2010) 082507.

- [31] W. L. Rowan *et al.* “Impurity rotation in hydrogen and helium plasmas”. *Physics of Fluids B* **4** (1992) 917–923.
- [32] A. G. Meigs and W. L. Rowan. “Impurity poloidal rotation velocity in tokamaks”. *Physics of Plasmas* **1** (1994) 960–967.
- [33] K. Crombé *et al.* “Poloidal Rotation Dynamics, Radial Electric Field, and Neoclassical Theory in the Jet Internal-Transport-Barrier Region”. *Phys. Rev. Lett.* **95** (2005) 155003.
- [34] T. Tala *et al.* “Toroidal and poloidal momentum transport studies in JET”. *Nuclear Fusion* **47** (2007) 1012.
- [35] W. M. Solomon *et al.* “Experimental test of the neoclassical theory of impurity poloidal rotation in tokamaks”. *Physics of Plasmas* **13** (2006) 056116.
- [36] R. E. Bell *et al.* “Core poloidal rotation and internal transport barrier formation in TFTR”. *Plasma Physics and Controlled Fusion* **40** (1998) 609.
- [37] B. A. Grierson *et al.* “Collisionality scaling of main-ion toroidal and poloidal rotation in low torque DIII-D plasmas”. *Nuclear Fusion* **53** (2013) 063010.
- [38] K. Brau *et al.* “Plasma rotation in the PDX tokamak”. *Nuclear Fusion* **23** (1983) 1643.
- [39] C. Chrystal *et al.* “Calculation of impurity poloidal rotation from measured poloidal asymmetries in the toroidal rotation of a tokamak plasma”. *Review of Scientific Instruments* **83** (2012) 10D501.
- [40] A. Bortolon *et al.* “Indirect measurement of poloidal rotation using inboard-outboard asymmetry of toroidal rotation and comparison with neoclassical predictions”. *Nuclear Fusion* **53** (2013) 023002.
- [41] A. Lebschy *et al.* “Indirect measurement of the poloidal rotation in the core of ASDEX Upgrade plasmas with charge exchange recombination spectroscopy”. *Europhysics Conference Abstracts (CD-ROM, Proc. of the 42th EPS Conference on Plasma Physics, Lisbon, Portugal, 2015)*. Ed. by R. Bingham *et al.* Vol. 39E (2015). 2015.
- [42] R. M. McDermott *et al.* “Extensions to the charge exchange recombination spectroscopy diagnostic suite at ASDEX Upgrade”. *Review of Scientific Instruments* **88** (2017) 073508.
- [43] Max-Planck-Institut für Plasmaphysik. *AUG Drawing Gallery*. https://www.aug.ipp.mpg.de/aug/local/aug_only/AUG_Aufbau/Drawing_Gallery/index.htm.
- [44] J. Wesson and D. J. Campbell. *Tokamaks*. English. Oxford: Clarendon Press; New York: Oxford University Press, 2004. ISBN: 0198509227.
- [45] B. Streibl *et al.* “Chapter 2: Machine Design, Fueling, and Heating in ASDEX Upgrade”. *Fusion Science and Technology* **44** (2003) 578–592.
- [46] N. A. Salmon. “First electron temperature edge measurements on the asdex upgrade tokamak using a heterodyne radiometer”. *International Journal of Infrared and Millimeter Waves* **15** (1994) 53–60. ISSN: 1572-9559.

- [47] W. Suttrop. *Practical Limitations to Plasma Edge Electron Temperature Measurements by Radiometry of Electron Cyclotron Emission*. IPP Report 1/306. Max-Planck-Institut für Plasmaphysik, Garching, Germany, 1996.
- [48] S. K. Rathgeber *et al.* “Estimation of edge electron temperature profiles via forward modelling of the electron cyclotron radiation transport at ASDEX Upgrade”. *Plasma Physics and Controlled Fusion* **55** (2013) 025004.
- [49] R. Fischer *et al.* “Probabilistic lithium beam data analysis”. *Plasma Physics and Controlled Fusion* **50** (2008) 085009.
- [50] M. Willensdorfer *et al.* “Improved chopping of a lithium beam for plasma edge diagnostic at ASDEX Upgrade”. *Review of Scientific Instruments* **83** (2012) 023501.
- [51] E. Wolfrum *et al.* “Fast lithium-beam spectroscopy of tokamak edge plasmas”. *Review of Scientific Instruments* **64** (1993) 2285–2292.
- [52] S. Fiedler *et al.* “Edge plasma diagnostics on W7-AS and ASDEX-Upgrade using fast Li beams”. *Journal of Nuclear Materials* **266 - 269** (1999) 1279–1284. ISSN: 0022-3115.
- [53] A. Mlynek *et al.* “Design of a digital multiradian phase detector and its application in fusion plasma interferometry”. *Review of Scientific Instruments* **81** (2010) 033507.
- [54] W. E. Gordon. “Incoherent Scattering of Radio Waves by Free Electrons with Applications to Space Exploration by Radar”. *Proceedings of the IRE* **46** (1958) 1824–1829. ISSN: 0096-8390.
- [55] K. L. Bowles. “Observation of Vertical-Incidence Scatter from the Ionosphere at 41 Mc/sec”. *Phys. Rev. Lett.* **1** (1958) 454–455.
- [56] D. H. Froula *et al.* *Plasma Scattering of Electromagnetic Radiation: Theory and Measurement Techniques*. Elsevier, Amsterdam, 2011.
- [57] B. Kurzan and H. D. Murmann. “Edge and core Thomson scattering systems and their calibration on the ASDEX Upgrade tokamak”. *Review of Scientific Instruments* **82** (2011) 103501.
- [58] T. Happel *et al.* “Core turbulence behavior moving from ion-temperature-gradient regime towards trapped-electron-mode regime in the ASDEX Upgrade tokamak and comparison with gyrokinetic simulation”. *Physics of Plasmas* **22** (2015) 032503.
- [59] G. D. Conway *et al.* “Interaction of Mean and Oscillating Plasma Flows Across Confinement Mode Transitions”. *Plasma Fusion Res.* **5** (2010) S2005.
- [60] M. Hirsch *et al.* “Doppler reflectometry for the investigation of propagating density perturbations”. *Plasma Physics and Controlled Fusion* **43** (2001) 1641.
- [61] E. Poli, A. G. Peeters, and G. V. Pereverzev. “TORBEAM, a beam tracing code for electron-cyclotron waves in tokamak plasmas”. *Computer Physics Communications* **136** (2001) 90–104.

- [62] N. Mahdizadeh *et al.* “Investigation of the parallel dynamics of drift-wave turbulence in toroidal plasmas”. *Plasma Physics and Controlled Fusion* **49** (2007) 1005.
- [63] C. P. Ritz *et al.* “Advanced plasma fluctuation analysis techniques and their impact on fusion research (invited)”. *Review of Scientific Instruments* **59** (1988) 1739–1744.
- [64] J.-N. Leboeuf *et al.* “TEXT tokamak edge turbulence modeling”. *Physics of Fluids B: Plasma Physics* **3** (1991) 2291–2299.
- [65] S. J. Zweben and S. S. Medley. “Visible imaging of edge fluctuations in the TFTR tokamak”. *Physics of Fluids B: Plasma Physics* **1** (1989) 2058–2065.
- [66] P. C. Liewer. “Measurements of microturbulence in tokamaks and comparisons with theories of turbulence and anomalous transport”. *Nuclear Fusion* **25** (1985) 543.
- [67] T. Estrada *et al.* “Sheared flows and transition to improved confinement regime in the TJ-II stellarator”. *Plasma Physics and Controlled Fusion* **51** (2009) 124015.
- [68] B. Nold *et al.* “Generation of blobs and holes in the edge of the ASDEX Upgrade tokamak”. *Plasma Physics and Controlled Fusion* **52** (2010) 065005.
- [69] A. Lebschy *et al.* “Measurement of the complete core plasma flow across the LOC–SOC transition at ASDEX Upgrade”. *Nuclear Fusion* **58** (2018) 026013.
- [70] D. Prisiazhniuk *et al.* “Magnetic field pitch angle and perpendicular velocity measurements from multi-point time-delay estimation of poloidal correlation reflectometry”. *Plasma Physics and Controlled Fusion* **59** (2017) 025013.
- [71] V. A. Vershkov, V. V. Dreval, and S. V. Soldatov. “A three-wave heterodyne correlation reflectometer developed in the T-10 tokamak”. *Review of Scientific Instruments* **70** (1999) 1700–1709.
- [72] A. Krämer-Flecken and S. Soldatov. “On the possibility to use Correlation Reflectometry for determination of safety factor at TEXTOR”. *10th International Reflectometry Workshop, Consorzio RFX, Padova, Italy*. 2011.
- [73] H. Grad and H. Rubin. “Hydromagnetic Equilibria and Force-Free Fields”. *Proceedings of the 2nd UN Conf. on the Peaceful Uses of Atomic Energy*. Vol. 31. Geneva: IAEA, 1958, p. 190.
- [74] V. D. Shafranov. “Equilibrium of a toroidal plasma in a magnetic field”. *Journal of Nuclear Energy. Part C, Plasma Physics, Accelerators, Thermonuclear Research* **5** (1963) 251.
- [75] P. J. McCarthy, P. Martin, and W. Schneider. *The CLISTE Interpretive Equilibrium Code*. IPP Report 5/85. Max-Planck-Institut für Plasmaphysik, Garching, Germany, 1985.

- [76] P. J. McCarthy. “Analytical solutions to the Grad–Shafranov equation for tokamak equilibrium with dissimilar source functions”. *Physics of Plasmas* **6** (1999) 3554–3560.
- [77] M. Dunne *et al.* “Measurement of neoclassically predicted edge current density at ASDEX Upgrade”. *Nuclear Fusion* **52** (2012) 123014.
- [78] R. Fischer *et al.* “Coupling of the Flux Diffusion Equation with the Equilibrium Reconstruction at ASDEX Upgrade”. *Fusion Science and Technology* **69** (2016) 526–536.
- [79] H. Yuh. “The Motional Stark Effect Diagnostic on Alcator C-Mod”. PhD thesis. Massachusetts Institute of Technology (MIT), 2005.
- [80] R. C. Wolf *et al.* “Motional Stark Effect measurements of the local magnetic field in high temperature fusion plasmas”. *Journal of Instrumentation* **10** (2015) P10008.
- [81] I. H. Hutchinson. *Principles of Plasma Diagnostics*. 2nd. Cambridge University Press, Cambridge, 2002.
- [82] A. Bock. “Generation and (Analysis of Plasmas with Centrally Elevated Helicity Profiles in Full W ASDEX Upgrade”. PhD thesis. Ludwig-Maximilians Universität München / Max-Planck-Institut für Plasmaphysik, 2016.
- [83] D. M. Rittich. “Quantification of Neutral Beam Driven Current and the effect of radial fast ion transport in ASDEX Upgrade”. PhD thesis. Universität Augsburg / Max-Planck-Institut für Plasmaphysik, 2017.
- [84] O. P. Ford, J. Howard, and R. C. Wolf. “The prototype imaging motional Stark effect diagnostic for ASDEX upgrade”. *Review of Scientific Instruments* **86** (2015) 093504.
- [85] A. Mlynek *et al.* “First results from the new sub-millimeter polarimeter on the ASDEX Upgrade tokamak”. *Poster presented at 21st Topical Conference on High Temperature Plasma Diagnostics (HTPD 2016), Madison, WI*. 2016.
- [86] J. P. Freidberg. *Plasma Physics and Fusion Energy*. Cambridge University Press, New York, 2007.
- [87] S. I. Braginskii. “Reviews of Plasma Physics”. Ed. by M. A. Leontovich. Consultants Bureau, New York, 1965. Chap. Transport Processes in a Plasma, pp. 205–311.
- [88] F. L. Hinton and R. D. Hazeltine. “Theory of plasma transport in toroidal confinement systems”. *Rev. Mod. Phys.* **48** (1976) 239–308.
- [89] EuroFusion. EuroFusion Charged Particle Movements (2005).
- [90] J. Hugill. “Transport in tokamaks - a review of experiment”. *Nuclear Fusion* **23** (1983) 331.
- [91] F. Wagner and U. Stroth. “Transport in toroidal devices-the experimentalist’s view”. *Plasma Physics and Controlled Fusion* **35** (1993) 1321.

- [92] F. Romanelli. “Models of plasma transport based on microturbulence”. *Plasma Physics and Controlled Fusion* **31** (1989) 1535.
- [93] M. Rosenbluth and C. Longmire. “Stability of plasmas confined by magnetic fields”. *Annals of Physics* **1** (1957) 120–140. ISSN: 0003-4916.
- [94] W. Horton. “Drift waves and transport”. *Rev. Mod. Phys.* **71** (1999) 735–778.
- [95] B. Coppi and G. Rewoldt. “New Trapped-Electron Instability”. *Phys. Rev. Lett.* **33** (1974) 1329–1332.
- [96] R. D. Hazeltine. “Rotation of a toroidally confined, collisional plasma”. *Physics of Fluids* **17** (1974) 961–968.
- [97] A. G. Peeters. private communication.
- [98] K. H. Burrell and C. Chrystal. “Functional form for plasma velocity in a rapidly rotating tokamak discharge”. *Physics of Plasmas* **21** (2014) 072316.
- [99] S. Hirshman and D. Sigmar. “Neoclassical transport of impurities in tokamak plasmas”. *Nuclear Fusion* **21** (1981) 1079.
- [100] Y. B. Kim, P. H. Diamond, and R. J. Groebner. “Neoclassical poloidal and toroidal rotation in tokamaks”. *Physics of Fluids B* **3** (1991) 2050–2060.
- [101] A. G. Peeters. “Reduced charge state equations that describe Pfirsch Schlüter impurity transport in tokamak plasma”. *Physics of Plasmas* **7** (2000) 268–275.
- [102] E. A. Belli and J. Candy. “Kinetic calculation of neoclassical transport including self-consistent electron and impurity dynamics”. *Plasma Physics and Controlled Fusion* **50** (2008) 095010.
- [103] W. A. Houlberg *et al.* “Bootstrap current and neoclassical transport in tokamaks of arbitrary collisionality and aspect ratio”. *Physics of Plasmas* **4** (1997) 3230–3242.
- [104] R. Hawryluk *et al.* “An empirical approach to tokamak transport”. *Physics of plasmas close to thermonuclear conditions* **1** (1980) 19–46.
- [105] E. E. Simmet and the ASDEX Team. “Statistical analysis of the global energy confinement time in Ohmic discharges in the ASDEX tokamak”. *Plasma Physics and Controlled Fusion* **38** (1996) 689.
- [106] E. P. Gorbunov, S. V. Mirnov, and V. S. Strelkov. “Energy confinement time of a plasma as a function of the discharge parameters in TOKAMAK-3”. *Nuclear Fusion* **10** (1970) 43.
- [107] C. Daughney. “Empirical scaling for present Ohmically heated tokamaks”. *Nuclear Fusion* **15** (1975) 967.
- [108] D. L. Jassby, D. R. Cohn, and R. R. Parker. “Reply to ”Comments on the paper ’Characteristics of high-density tokamak ignition reactors’””. *Nuclear Fusion* **16** (1976) 1045.
- [109] W. Pfeiffer and R. E. Waltz. “Empirical scaling laws for energy confinement in Ohmically-heated tokamaks”. *Nuclear Fusion* **19** (1979) 51.

- [110] R. J. Goldston. “Energy confinement scaling in tokamaks: some implications of recent experiments with Ohmic and strong auxiliary heating”. *Plasma Physics and Controlled Fusion* **26** (1984) 87.
- [111] D. Cohn, R. Parker, and D. Jassby. “Characteristics of high-density tokamak ignition reactors”. *Nuclear Fusion* **16** (1976) 31.
- [112] M. Murakami *et al.* “Plasma Confinement Studies in the ISX-A Tokamak”. *Phys. Rev. Lett.* **42** (1979) 655–658.
- [113] S. Fairfax *et al.* “Energy and particle confinement in the Alcator tokamaks”. *Proceedings of the Eighth International Conference on Plasma Physics and Controlled Nuclear Fusion Research*. Ed. by B. International Atomic Energy Agency. Vol. 1. 1980, pp. 439–450.
- [114] S. Ejima *et al.* “Scaling of energy confinement with minor radius, current and density in Doublet III Ohmically heated plasmas”. *Nuclear Fusion* **22** (1982) 1627.
- [115] R. E. Waltz and G. E. Guest. “Maximum Energy-Confinement Time in Joule-Heated Tokamaks”. *Phys. Rev. Lett.* **42** (1979) 651–655.
- [116] U. Stroth. “A comparative study of transport in stellarators and tokamaks”. *Plasma Physics and Controlled Fusion* **40** (1998) 9.
- [117] F. Alladio *et al.* “Analysis of saturated ohmic confinement in FT”. *Plasma Physics and Controlled Fusion Research (Proc. 13th Int. Conf., Washington, DC, 1990)*. Vol. 2. 1991, p. 153.
- [118] G. Bracco *et al.* “Electron heat transport analysis of FTU Ohmic plasmas”. *Proc. Varenna Meeting on Local Transport (Varenna) (Bologna: Editrice Compositori)*. 1993, p. 63.
- [119] X. Garbet *et al.* “Turbulence and energy confinement in TORE SUPRA Ohmic discharges”. *Nuclear Fusion* **32** (1992) 2147.
- [120] I. Erofeev *et al.* “Theory-based modeling of LOC–SOC transitions in ASDEX Upgrade”. *Nuclear Fusion* **57** (2017) 126067.
- [121] C. Angioni *et al.* “Relationship between density peaking, particle thermodiffusion, Ohmic confinement, and microinstabilities in ASDEX Upgrade L-mode plasmas”. *Physics of Plasmas* **12** (2005) 040701.
- [122] P. N. Yushmanov *et al.* “Scalings for tokamak energy confinement”. *Nuclear Fusion* **30** (1990) 1999.
- [123] F. Wagner *et al.* “Regime of Improved Confinement and High Beta in Neutral-Beam-Heated Divertor Discharges of the ASDEX Tokamak”. *Phys. Rev. Lett.* **49** (1982) 1408–1412.
- [124] M. Cavedon. “The role of the radial electric field in the development of the edge transport barrier in the ASDEX Upgrade tokamak”. PhD thesis. Technische Universität München / Max-Planck-Institut für Plasmaphysik, 2015.
- [125] J. Snipes *et al.* “H mode power threshold database for ITER”. *Nuclear Fusion* **36** (1996) 1217.

- [126] Y. R. Martin, T. Takizuka, and the ITPA CDBM H-mode Threshold Database Working Group. “Power requirement for accessing the H-mode in ITER”. *Journal of Physics: Conference Series* **123** (2008) 012033.
- [127] F. Ryter *et al.* “Experimental Characterization of the Electron Heat Transport in Low-Density ASDEX Upgrade Plasmas”. *Phys. Rev. Lett.* **86** (2001) 5498–5501.
- [128] X. Garbet *et al.* “Profile stiffness and global confinement”. *Plasma Physics and Controlled Fusion* **46** (2004) 1351.
- [129] R. J. Fonck, D. S. Darrow, and K. P. Jaehnig. “Determination of plasma-ion velocity distribution via charge-exchange recombination spectroscopy”. *Phys. Rev. A* **29** (1984) 3288–3309.
- [130] R. C. Isler. “A Review of Charge-Exchange Spectroscopy and Applications to Fusion Plasmas”. *Physica Scripta* **35** (1987) 650.
- [131] R. Dux. *STRAHL User Manual*. IPP Report 10/30. Max-Planck-Institut für Plasmaphysik, Garching, Germany, 2006.
- [132] K. Behringer. *Description of the impurity code STRAHL*. Report (JET-R-87-08). Jet Joint Undertaking, Abingdon, United Kingdom, 1987.
- [133] J. D. Huba. *NRL PLASMA FORMULARY*. Tech. rep. Naval Research Laboratory, 2013.
- [134] A. D. Whiteford *et al.* *CXSFIT — User Manual*. Tech. rep. ADAS - Atomic Data and Analysis Structure, http://www.adas.ac.uk/notes/adas_r07-01.pdf, 2007.
- [135] P. Instruments. <http://www.princetoninstruments.com/>.
- [136] I. FARO Technologies. <http://www.faro.com>.
- [137] W. W. Heidbrink *et al.* “A Code that Simulates Fast-Ion $D\alpha$ and Neutral Particle Measurements”. *Communications in Computational Physics* **10** (2011) 716–741.
- [138] R. Dux. private communication.
- [139] R. E. Bell. “Exploiting a transmission grating spectrometer”. *Review of Scientific Instruments* **75** (2004) 4158–4161.
- [140] M. von Hellermann *et al.* “Analytical approximation of cross-section effects on charge exchange spectra observed in hot fusion plasmas”. *Plasma Physics and Controlled Fusion* **37** (1995) 71.
- [141] W. M. Solomon *et al.* “Extraction of poloidal velocity from charge exchange recombination spectroscopy measurements”. *Review of Scientific Instruments* **75** (2004) 3481–3486.
- [142] P. Zeeman. “The Effect of Magnetisation on the Nature of Light Emitted by a Substance”. *Nature* **55** (1897) 347–347.
- [143] P. Zeeman. “VII. Doublets and triplets in the spectrum produced by external magnetic forces”. *Philosophical Magazine Series 5* **44** (1897) 55–60.

- [144] A. Blom and C. Jupén. “Parametrization of the Zeeman effect for hydrogen-like spectra in high-temperature plasmas”. *Plasma Physics and Controlled Fusion* **44** (2002) 1229.
- [145] R. C. Isler. “An overview of charge-exchange spectroscopy as a plasma diagnostic”. *Plasma Physics and Controlled Fusion* **36** (1994) 171.
- [146] O. Sauter and S. Medvedev. “Tokamak coordinate conventions.” *Computer Physics Communications* **184** (2013) 293–302. ISSN: 0010-4655.
- [147] C. Chrystal *et al.* “Testing neoclassical and turbulent effects on poloidal rotation in the core of DIII-D”. *Physics of Plasmas* **21** (2014) 072504.
- [148] E. Viezzer *et al.* “Rotation and density asymmetries in the presence of large poloidal impurity flows in the edge pedestal”. *Plasma Physics and Controlled Fusion* **55** (2013) 124037.
- [149] R. Churchill *et al.* “In-out impurity density asymmetry in the pedestal region of Alcator C-Mod”. *Nuclear Fusion* **53** (2013) 122002.
- [150] R. M. McDermott *et al.* “Impurity density evaluation with the CHICA code”. *Review of Scientific Instruments* (“in-preparation”).
- [151] E. Viezzer *et al.* “High-accuracy characterization of the edge radial electric field at ASDEX Upgrade”. *Nuclear Fusion* **53** (2013) 053005.
- [152] E. Viezzer *et al.* “Evidence for the neoclassical nature of the radial electric field in the edge transport barrier of ASDEX Upgrade”. *Nuclear Fusion* **54** (2014) 012003.
- [153] K. D. Marr *et al.* “Comparison of neoclassical predictions with measured flows and evaluation of a poloidal impurity density asymmetry”. *Plasma Physics and Controlled Fusion* **52** (2010) 055010.
- [154] G. Kagan *et al.* “The effect of the radial electric field on neoclassical flows in a tokamak pedestal”. *Plasma Physics and Controlled Fusion* **53** (2011) 025008.
- [155] R. E. Bell *et al.* “Poloidal Rotation in TFTR Reversed Shear Plasmas”. *Phys. Rev. Lett.* **81** (1998) 1429–1432.
- [156] C. L. Rettig *et al.* “Search for the ion temperature gradient mode in a tokamak plasma and comparison with theoretical predictions”. *Physics of Plasmas* **8** (2001) 2232–2237.
- [157] R. M. McDermott *et al.* “Core intrinsic rotation behaviour in ASDEX Upgrade Ohmic L-mode plasmas”. *Nuclear Fusion* **54** (2014) 043009.
- [158] F. Imbeaux, F. Ryter, and X. Garbet. “Modelling of ECH modulation experiments in ASDEX Upgrade with an empirical critical temperature gradient length transport model”. *Plasma Physics and Controlled Fusion* **43** (2001) 1503.
- [159] F. Ryter *et al.* “Experimental Study of Trapped-Electron-Mode properties in tokamaks: threshold and stabilization by collisions”. *Phys. Rev. Lett.* **95** (2005) 085001.

- [160] C. Sung *et al.* “Changes in core electron temperature fluctuations across the Ohmic energy confinement transition in Alcator C-Mod plasmas”. *Nuclear Fusion* **53** (2013) 083010.
- [161] D. L. Brower *et al.* “Observation of a high-density ion mode in tokamak microturbulence”. *Phys. Rev. Lett.* **59** (1987) 48–51.
- [162] R. L. Watterson, R. E. Slusher, and C. M. Surko. “Low-frequency density fluctuations in a tokamak plasma”. *The Physics of Fluids* **28** (1985) 2857–2867.
- [163] H. Arnichand *et al.* “Quasi-coherent modes and electron-driven turbulence”. *Nuclear Fusion* **54** (2014) 123017.
- [164] H. Arnichand *et al.* “Identification of trapped electron modes in frequency fluctuation spectra”. *Plasma Physics and Controlled Fusion* **58** (2016) 014037.
- [165] G. D. Conway *et al.* “Observations on core turbulence transitions in ASDEX Upgrade using Doppler reflectometry”. *Nuclear Fusion* **46** (2006) S799.
- [166] G. D. Conway. “Turbulence measurements in fusion plasmas”. *Plasma Physics and Controlled Fusion* **50** (2008) 124026.
- [167] A. Bortolon *et al.* “Observation of Spontaneous Toroidal Rotation Inversion in Ohmically Heated Tokamak Plasmas”. *Phys. Rev. Lett.* **97** (2006) 235003.
- [168] D. Prisiazhniuk. “Development and application of poloidal correlation reflectometry to study turbulent structures in the ASDEX Upgrade tokamak”. PhD thesis. Technische Universität München / Max-Planck-Institut für Plasmaphysik, 2017.
- [169] R. M. McDermott *et al.* “Core momentum and particle transport studies in the ASDEX Upgrade tokamak”. *Plasma Physics and Controlled Fusion* **53** (2011) 124013.
- [170] A. G. Peeters *et al.* “The nonlinear gyro-kinetic flux tube code GKW”. *Computer Physics Communications* **180** (2009). 40 years of CPC: A celebratory issue focused on quality software for high performance, grid and novel computing architectures 2650–2672. ISSN: 0010-4655.
- [171] J. E. Rice *et al.* “Spontaneous core toroidal rotation in Alcator C-Mod L-mode, H-mode and ITB plasmas”. *Plasma Physics and Controlled Fusion* **50** (2008) 124042.
- [172] C. Angioni *et al.* “Intrinsic Toroidal Rotation, Density Peaking, and Turbulence Regimes in the Core of Tokamak Plasmas”. *Phys. Rev. Lett.* **107** (2011) 215003.
- [173] Y. J. Shi *et al.* “ECH effects on toroidal rotation: KSTAR experiments, intrinsic torque modelling and gyrokinetic stability analyses”. *Nuclear Fusion* **53** (2013) 113031.
- [174] J. C. Hillesheim *et al.* “Dependence of intrinsic rotation reversals on collisionality in MAST”. *Nuclear Fusion* **55** (2015) 032003.

-
- [175] A. Lebschy *et al.* “Measurement of the ExB velocity across the LOC-SOC transition”. *Europhysics Conference Abstracts (CD-ROM, Proc. of the 43th EPS Conference on Plasma Physics, Leuven, Belgium, 2016)*. Ed. by P. Mantica *et al.* Vol. 40A (2016). 2016.
- [176] E. Fable, C. Angioni, and O. Sauter. “The role of ion and electron electrostatic turbulence in characterizing stationary particle transport in the core of tokamak plasmas”. *Plasma Physics and Controlled Fusion* **52** (2010) 015007.

Appendix A

Taylor expansion of grating equation

The aim of this part is to derive the parabolic dependence of the central wavelength of the spectrometer channels as a function of the distance from the axis introduced in section 4.3. Starting point is, hence, the grating equation for a Czerny-Turner spectrometer as shown in figure 4.4:

$$\lambda = \frac{\cos \gamma}{n g} (\sin(\theta_1 + \phi_1) + \sin(\theta_2 + \phi_2)) \quad (\text{A.1})$$

In order to retrieve the parabolic dependence, the grating equation is approximated by a Taylor expansion for the two variables (γ, x_2) around $A = (\gamma = 0, x_2 = 0, \phi_1 = 0)$ up to second order. Small angles are assumed such that $\gamma \ll 1$ and $x_2 \ll f_2$.

$$\lambda = \lambda_0 + \underbrace{\frac{\partial \lambda}{\partial \gamma} \Big|_A}_{=0} \gamma + \frac{\partial \lambda}{\partial x_2} \Big|_A x_2 + \frac{\partial^2 \lambda}{\partial \gamma^2} \Big|_A \frac{\gamma^2}{2} + \underbrace{\frac{\partial^2 \lambda}{\partial \gamma \partial x_2} \Big|_A}_{=0} \gamma x_2 + \frac{\partial^2 \lambda}{\partial x_2^2} \Big|_A \frac{x_2^2}{2} \quad (\text{A.2})$$

with the single contributions:

- $\frac{\partial \lambda}{\partial \gamma} \Big|_A = - \underbrace{\frac{\sin \gamma}{n g}}_{=0, \sin 0=0} (\sin(\theta_1 + \phi_1) + \sin(\theta_2 + \phi_2)) = 0$
- $\frac{\partial \lambda}{\partial x_2} \Big|_A = \left(\frac{\lambda_0}{f_2} \right) \frac{\cos \gamma \cos(\theta_2 + \phi_2) \cos^2 \phi_2}{\sin \theta_1 + \sin \theta_2} \Big|_A = \left(\frac{\lambda_0}{f_2} \right) \frac{\cos \theta_2}{\sin \theta_1 + \sin \theta_2}$, with
 $\phi_2 = \arctan \frac{x_2}{f_2}; \frac{\partial \phi_2}{\partial x_2} = \left(1 + \left(\frac{x_2}{f_2} \right)^2 \right)^{-1} = \cos^2 \phi_2; \cos^2(\arctan x) = (1 + x^2)^{-1}$
- $\frac{\partial^2 \lambda}{\partial \gamma^2} \Big|_A = - \frac{\cos \gamma}{n g} (\sin(\theta_1 + \phi_1) + \sin(\theta_2 + \phi_2)) \Big|_A = -\lambda_0$
- $\frac{\partial^2 \lambda}{\partial \gamma \partial x_2} \Big|_A = - \left(\frac{\lambda_0}{f_2} \right) \frac{\sin \gamma \cos(\theta_2 + \phi_2) \cos^2 \phi_2}{\sin \theta_1 + \sin \theta_2} \Big|_A = 0$

- $\frac{\partial^2 \lambda}{\partial x_2^2} \Big|_A = - \left(\frac{\lambda_0}{f_2} \right) \frac{\sin \theta_2}{\sin \theta_1 + \sin \theta_2}$ with

$$\begin{aligned} \frac{\partial \cos(\theta_2 + \phi_2) \cos^2 \phi_2}{\partial x_2} &= - \sin(\theta_2 + \phi_2) \cos^4 \phi_2 / f_2 \\ &\quad - \underbrace{\cos(\theta_2 + \phi_2) 2 \cos \phi_2 \sin \phi_2 \cos^2 \phi / f_2}_{=0} \\ &= - \sin \theta_2 / f_2 \end{aligned}$$

Putting everything together, equation (A.2) reveals as:

$$\Delta \lambda = \lambda - \lambda_0 = -\lambda_0 \frac{\gamma^2}{2} + \frac{x_2 \lambda_0}{2 f_2 (\sin \theta_1 + \sin \theta_2)} \left(2 \cos \theta_2 - \frac{x_2}{f_2} \sin \theta_2 \right) \quad (\text{A.3})$$

We are interested in the location of the same wavelength across all channels. Therefore, $\Delta \lambda$ is set to zero and due to the small angle approximation one can approximate $\tan \gamma \approx \gamma = y_2 / f_2$. This gives the following parabolic behavior:

$$\boxed{y_2^2 = \frac{x_2 f_2}{\sin \theta_1 + \sin \theta_2} \underbrace{\left(2 \cos \theta_2 - \frac{x_2}{f_2} \sin \theta_2 \right)}_{=2 \cos \theta_2, \text{ since } x_2 \ll f_2} = \frac{2 f_2 \cos \theta_2}{\sin \theta_1 + \sin \theta_2} x_2} \quad (\text{A.4})$$

Appendix B

Derivations of q-dependence of indirect u_{pol} measurement

In order to derive the q-dependence of the indirect measurement of u_{pol} for a circular plasma, the following equations are necessary:

$$u_{\text{tor}} = \hat{\omega}(\psi)R + s_b \hat{u}(\psi)F(\psi)/R \quad (\text{B.1})$$

$$u_{\text{pol}} = s_j \hat{u}(\psi)B_{\text{pol}} \quad (\text{B.2})$$

$$R_0 = \frac{R_{\text{LFS}} + R_{\text{HFS}}}{2}, a = \frac{R_{\text{LFS}} - R_{\text{HFS}}}{2} \quad (\text{B.3})$$

$$\frac{B_{\text{tor},0}}{B_{\text{tor},1}} = \frac{R_1}{R_0} \quad (\text{B.4})$$

In the following s_b and s_j are set to 1 and the difference between LFS and HFS toroidal rotation frequency can be written as:

$$\begin{aligned} \Delta \omega_{\text{tor}} = \omega_{\text{tor,HFS}} - \omega_{\text{tor,LFS}} &= \frac{u_{\text{tor,HFS}}}{R_{\text{HFS}}} - \frac{u_{\text{tor,LFS}}}{R_{\text{LFS}}} \\ &\xrightarrow{(B.1)} \hat{u}(\Psi) \left(\frac{B_{\text{tor,HFS}}}{R_{\text{HFS}}} - \frac{B_{\text{tor,LFS}}}{R_{\text{LFS}}} \right) \end{aligned} \quad (\text{B.5})$$

The second part of the product can be approximated further:

$$\begin{aligned} \frac{B_{\text{tor,HFS}}}{R_{\text{HFS}}} - \frac{B_{\text{tor,LFS}}}{R_{\text{LFS}}} &\stackrel{(B.4)}{=} B_{\text{tor},0} R_0 \left(\frac{1}{R_{\text{HFS}}^2} - \frac{1}{R_{\text{LFS}}^2} \right) \\ &= B_{\text{tor},0} R_0 \frac{(R_{\text{LFS}} + R_{\text{HFS}})(R_{\text{LFS}} - R_{\text{HFS}})}{R_{\text{HFS}}^2 R_{\text{LFS}}^2} \\ &\stackrel{(B.3)}{=} \frac{B_{\text{tor},0} R_0}{R_{\text{HFS}}^2 R_{\text{LFS}}^2} \stackrel{(*)}{=} \frac{4a B_{\text{tor},0}}{R_0^2} \end{aligned} \quad (\text{B.6})$$

(*) using the approximation: $\frac{1}{R_{\text{HFS}}^2 R_{\text{LFS}}^2} = \frac{1}{(R_0^2 - a^2)^2} \approx \frac{1}{R_0^4}$ for $R_0 \gg a$.

Putting everything together, $\Delta \omega_{\text{tor}}$ can be expressed as:

$$\begin{aligned}
 \boxed{\Delta \omega_{\text{tor}}} &\stackrel{(B.5)}{=} \hat{u}(\Psi) \left(\frac{B_{\text{tor,HFS}}}{R_{\text{HFS}}} - \frac{B_{\text{tor,LFS}}}{R_{\text{LFS}}} \right) \stackrel{(B.6)}{=} \hat{u}(\Psi) \frac{4 a B_{\text{tor},0}}{R_0^2} \\
 &\stackrel{(B.2)}{=} \frac{u_{\text{pol}}}{B_{\text{pol}}} \frac{4 a B_{\text{tor},0}}{R_0^2} = \frac{4}{R_0} \underbrace{\frac{a B_{\text{tor},0}}{R_0 B_{\text{pol}}}}_{\equiv q} u_{\text{pol}} = \boxed{\frac{4 q}{R_0} u_{\text{pol}}} \quad (B.7)
 \end{aligned}$$